DTU Wind

Structural load analysis and optimization of the VAWT design

Nienke Senden

DTU Wind-M-0677
September 2023

Author: Nienke Senden

DTU Wind-M-0677
September 2023

Title:
Structural load analysis and optimization of the VAWT design

Project period:
November 2022 - September 2023

ECTS: 45

Education: Master of Science

Supervisor(s):

Taeseong Kim
Antariksh C. Dicholkar
DTU Wind and Energy Systems

Carlos Simao Ferreira
TU Delft

Jeroen Donkers
Eric Romeijn
HUISMAN

Remarks:
This report is submitted as partial fulfillment of the requirements for graduation in the above education at the Technical University of Denmark.

DTU Wind and Energy Systems is a department of the Technical University of Denmark with a unique integration of research, education, innovation and public/private sector consulting in the field of wind and energy. Our activities develop new opportunities and technology for the global and Danish exploitation of wind and energy. Research focuses on key technical-scientific fields, which are central for the development, innovation and use of wind energy and provides the basis for advanced education.

Technical University of Denmark
Department of Wind and Energy Systems
Frederiksborgvej 399
DK-4000 Roskilde
www.wind.dtu.dk

Structural load analysis and optimization of the VAWT design

Master's thesis in Wind Energy

Nienke Senden

Structural load analysis and optimization of the VAWT design

Thesis report

by

Nienke Senden

to obtain the degrees of

Master of Science
in Engineering (European Wind Energy)
at Technical University of Denmark

Master of Science
in Aerospace Engineering
at Delft University of Technology

To be defended on August 31st, 2023

Supervisors:	Carlos Simão Ferreira	TU Delft
	Taeseong Kim	DTU
	Jeroen Donkers	Huisman
	Eric Romeijn	Huisman
Defence committee:	Gianfranco la Rocca	TU Delft
	Wei Yu	TU Delft
Start date:	November 1st, 2022	
End date:	August 16th, 2023	
Student number:	TU Delft	4836081
	DTU	s213894

An electronic version of this thesis is available at `http://repository.tudelft.nl/`.

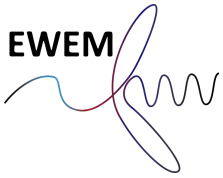

Summary

The increasing global electricity consumption requires a corresponding increase in energy generation. Wind turbines generate electricity without depleting natural resources or emitting greenhouse gases, offering a straightforward solution to the energy dilemma. Wind power, because of recent technology breakthroughs, is a financially viable, clean, and quickly expanding source of energy. Traditional horizontal axis wind turbines (HAWTs) have been favored over the years due to a lack of research and development on vertical axis wind turbines (VAWTs). However, as wind turbines are deployed further offshore, conventional HAWTs begin to make less sense for floating platforms, as their high center of gravity can cause major tilting concerns.

VAWTs can be considered instead, as the rotor design can provide numerous possibilities to make them more commercially competitive than HAWTs. There is currently a lack of understanding of how specific design parameters influence the rotor configuration of modern VAWTs. This thesis attempts to identify design drivers for the VAWT design while accounting for their aerodynamic behavior and aeroelastic stability.

The VAWT is modeled in an aeroelastic analysis tool named HAWC2 [1][2]. First, the cross-sectional parameters of the blades and struts are determined using the BECAS software, which can be used as an input file for HAWC2 [3][4]. The original model is based on the reference model of Schelbergen [5], which is then verified. After that, several design factors are found and investigated to see how they affect the performance and behavior of the wind turbine. These design parameters include elements, such as the thickness of the laminate, the placement of the struts, and an additional diagonal strut. The study carries out a parametric analysis, to understand what can benefit an optimal VAWT design.

The verification phase shows that the reference model has significantly lower power output, most likely due to implementing a dynamic stall model in the aeroelastic analysis. The significance of proper modeling of the dynamic stall effects is highlighted. As with the reference model, a range of laminate thicknesses is provided, therefore, multiple models with different laminate thicknesses are examined. The assessment reveals that opting for thinner laminates can lead to reduced mass and expenses without significant power output compromise but with less structural integrity. Moreover, the optimal placement of the struts for increasing power output while preserving structural integrity can be identified through strut placement analysis. Besides, an additional diagonal strut shows enhanced structural stability but could be more expensive. The upscaling of the model is done by increasing the aspect ratio (with the blade length). The power generation is increased, but it is crucial to pay attention to the structural integrity and aeroelastic stability, as the deflection of the blades increases significantly. The study also looks into the Huisman VAWT design, which is compared to the company's own findings. The design is simplified but still shows good power output and blade behavior.

In short, this study examines the design drivers of the VAWT design, paving the way for advancing VAWTs in practical applications and future research.

Acknowledgments

With this Master's thesis, I close off the last two years of my student life. The European Wind Energy Master (EWEM) has given me the experience of living abroad, studying at different universities, and meeting many new friends. I am extremely grateful for the chance I was blessed to travel to Denmark and live there. It helped me broaden my horizons and develop new perspectives and insights in a variety of fields. It has been a blast studying in Denmark, at the Technical University of Denmark (DTU), and in the Netherlands, at the Technical University of Delft (TU Delft). I want to thank everyone I have met, especially my friends from the studies. I have benefited greatly from your friendship, support, and, encouragement.

I want to express my sincere gratitude to Carlos Simão Ferreira and Taeseong Kim, my two university supervisors, for their mentoring and support during my thesis. Despite their hectic schedules, they met me almost weekly for a progress meeting. I would also like to thank Antariksh C. Dicholkar, for his kind assistance.

Moreover, I would like to thank my supervisor Jeroen Donkers from Huisman, to make me feel at home at the company while also helping me with the project wherever he could. For every question, I could step by him. Furthermore, the helpful suggestions and industry knowledge helped me develop my research topics and understand my results. On top of that, I would like to express my gratitude to Eric Romeijn, who gave me advice and relevant knowledge, and this opportunity at the company. I have met a lot of great people here.

Finally, I am thankful for my family, for giving me the chance to experience this adventure and their unwavering love, inspiration, and support.

N. Senden
Schiedam, The Netherlands
16.08.2023

Contents

Nomenclature

List of Abbreviations

2D	Two dimensional
3D	Three dimensional
A.D.	anno Domini
ACM	Actuator Cylinder Model
AoA	Angle of attack
B-L	Beddoes-Leishman
B.C.	before Christ
BECAS	BEam Cross section Analysis Software
BEM	Blade Element Theory
c.g.	Center of gravity
CFD	Computational Fluid Dynamics
CFRP	Carbon Fiber Reinforced Plastic
CG	Conjugate gradient
COE	Cost of Energy
CSD	Computational Structural Dynamics
DEL	Damage Equivalent Load
DLC	Design Load Case
DMST	Double Multiple Stream Tube
DNS	Direct Numerical Solution
DoF	Degree of Freedom
DTU	Denmark Technical University
DW	Downwind
EDC	Extreme Direction Change Model
EDC	Extreme Direction Change
EOG	Extreme Operating Gust Model
EOG	Extreme Operating Gust
ETM	Extreme Turbulence Model
EWEM	European Wind Energy Master
EWM	Extreme Wind Model
EWS	Extreme Wind Shear Model
EWS	Extreme Wind Shear
EWV	Extreme Wind Veer
F	Fatigue load cases
FEM	Finite Element Model
FPM	Fully Populated stiffness Matrix
FVAWT	Floating Vertical Axis Wind Turbine
GFRP	Glass Fiber Reinforced Plastic
HAWC2	Horizontal Axis Wind turbine simulation Code 2nd generation
HAWT	Horizontal Axis Wind Turbine
IEC	International Electrotechnical Commission
LE	Leading Edge
LES	Large Eddy Simulations
MBS	Multi-Body Systems
MDO	Multidisciplinary Design Optimization
N-S	Navier-Stokes
NTM	Normal Turbulence Model
ODEs	Ordinary Differential Equations
RANS	Reynolds Averaged Navier-Stokes
SNL	Sandio National Laboraties
SST	Single Stream Tube
TE	Trailing Edge
TSR	Tip Speed Ratio
TU Delft	Technical University Delft
U	Ultimate load cases
UW	Upwind
VAWT	Vertical Axis Wind Turbine
VVAWT	Vane type Vertical Axis Wind Turbine
WT	Wind Turbine

List of Greek Symbols

α	Angle of attack
$\varnothing$	Diameter
Γ	Circulation
γ	Pitching angle of the blade
γ_F	Load safety factor
γ_M	Material safety factor
γ_N	Consequence-of-failure factor
λ	Tip speed ratio
ν	Poisson's ratio
ω	Rotational speed
Φ	Pitch angle
Ψ	Inflow angle
ρ	Density
σ	Solidity / Stress
θ	Azimuthal angle
θ_p	Pitch angle
θ_t	Twist angle

List of Symbols

$\dot{m}$	Mass flow rate
$\vec{f}$	External forces
$\vec{T}$	Stress tensor on the fluid
$\vec{v}$	Flow velocity
A	Area
a	Axial induction factor
B	Number of blades
c	Chord length of blade
C_D	Drag coefficient
C_L	Lift coefficient
C_N	Nrmal coefficient
C_p	Power coefficient
C_Q	Torque coefficient
c_s	Speed of sound
C_T	Thrust coefficient
C_t	Tangential force coefficient
D	Diameter of rotor
d	Diameter
E	Young's modulus
F	Force
f	Frequency of shedding vortex / Interpolation factor
G	Shear's modulus
H	Blade height
h	Height
I	Area moment of inertia
K	Torsional stiffness constant
k	Weibull shape parameter
L	Length
L'	Airfoil lift
M	Moment
m	Mass (per unit length)
Ma	Mach number
N	Quantity / Number
P	Power
p	Pressure
Q	Torque
q	Centrifugal force per meter
Q_n	Non-dimensional time-averaged normal loading
Q_t	Non-dimensional time-averaged tangential loading
R	Radius of turbine
r_g	Radius of gyration
R_z	Elastic rotation
Re	Reynolds number
St	Strouhal number
T	Thrust
t	Thickness
U	Undisturbed wind speed
V	Velocity component
w	Deflection

List of Figures

List of Tables

1 Introduction

In this chapter, an introduction is given to the main topic of this thesis project. Some background and motivation are elaborated, followed by the aim of the project. The research questions are provided afterward. Lastly, the report structure of this thesis is presented.

1.1. Motivation and background

The background is given with an introduction to wind power, which is then further specified to offshore wind. A distinction can be made between horizontal axis wind turbines (HAWTs) and vertical axis wind turbines (VAWTs). The rise of VAWTs and their advantages are explored, leading up to the motivation of this thesis project.

1.1.1. Wind power

As global electricity consumption increases, energy generation needs to keep up [6][7]. This issue is acknowledged in Europe, where objectives have been established to achieve a renewable energy contribution of 27% in 2030 [7]. The simplest solution to the energy crisis that is hindering human progress without consuming natural resources, fossil fuels, or creating greenhouse gases is to install wind turbines [8]. Wind power is a commercially viable and quickly expanding source of electrical energy [9]. Recent substantial technological and design advancements have made it possible to produce and use wind energy on a massive scale [10]. Most wind turbines are placed together in farms, which is visible in Figure 1.1.

Figure 1.1: Wind farm of horizontal axis wind turbines (HAWTs) [11]. The photograph is taken by Inga Spence / Alamy Stock Photo.

After solar energy, wind turbines are swiftly overtaking as a major source of clean, sustainable, and affordable electricity throughout the world. In rural areas all over the world, solar and wind energy frequently offer the least expensive solutions for economic and community development while supplying electricity, fostering local employment and economic development [12]. Today, wind energy is regarded as the least expensive renewable energy source. The cost of creating wind energy has decreased by 80% over the past century [10]. However, fossil fuels, which are used to provide heat and electricity in homes, companies, and power plants, have by far been the main source of primary energy in the world [12]. Wind turbines are eco-friendly constructions that produce electricity from the kinetic energy of the wind [10]. There are two

classes of wind turbines, which are based on the axis of orientation [9]. There are the vertical axis wind turbines (VAWTs) and the conventional, horizontal axis wind turbines (HAWTs).

1.1.2. Offshore wind energy

The industry is turning to offshore wind energy to meet the high demand for renewable energy [7]. The number of offshore wind installations in Europe has increased over the past decade, as can be seen in Figure 1.2. There is more open space offshore, better wind conditions, and less visual and aural pollution. Most people complain about the appearance of wind turbines [13]. With the placement of wind turbines offshore, the visual impact is reduced. Nevertheless, it has been demonstrated that offshore wind farms can induce positive and negative contributions to marine life. While some marine life finds shelter and new habitats around offshore wind farms, placing the wind farms there can impact other fauna and marine life [14][15]. Pile-driving emits very high underwater sound levels, which brings the risk of injury to hearing in a large area, especially to harbor porpoises.

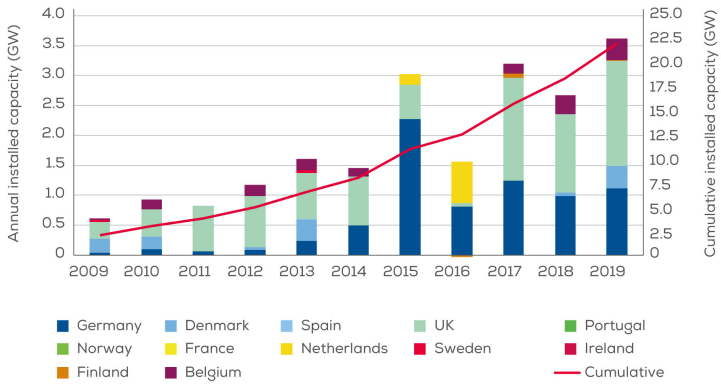

Figure 1.2: The annual offshore wind installations over the years 2009-2019 by country in Europe (left axis) and the cumulative capacity of the country (right axis) [16].

Offshore wind turbines are becoming larger than onshore due to the high expense of the infrastructure and maintenance to support wind turbines [17]. Higher wind speeds, strong seas, and accessibility issues cause more complicated maintenance. Furthermore, the offshore wind turbine business is still growing, while this is not the case for onshore wind turbines [5]. Besides, fewer wind turbines with the same total capacity can be installed economically due to these extra costs, while they also produce more energy than their onshore counterparts [17]. Offshore wind farms are considered to be more efficient due to the higher wind speeds, greater consistency, and lack of interference of objects.

Due to deep oceans and harsh climatic conditions, not everywhere bottom-fixed structures can be placed [7]. Floating farms are held in place by anchors rather than being fastened to the sea floor [17]. As a result, the wind turbines on floaters can be placed in deeper water regions. Some nations which have an interest are Norway and Japan. Furthermore, the North Sea's quick adoption of bottom-fixed wind farms has sparked a trend towards deeper seas that will eventually favor floating wind turbines.

1.1.3. The rise of VAWTs

The conventional HAWTs are widely used, as they have been tried the most in their history with refinement and improvements [9]. These days, wind turbines are frequently employed in open offshore projects. If wind turbines are positioned in the deep sea, a floating construction is required [18]. In Figure 1.3, HAWTs are placed offshore on floating constructions. However, the conventional HAWTs are beginning to make less sense offshore. They hold a lot of heavy components at the top, which brings challenges for floating platforms [19]. Moreover, the generator must be installed on the tower top, resulting in a high center of gravity. The weight of the control system unit also adds to the center of gravity [20]. This means that the floating platform could lead to a serious tilting issue [19]. These disadvantages sum up. Thus, vertical axis wind turbines (VAWTs) can be considered [7].

Figure 1.3: Floating horizontal axis wind turbines (HAWTs) [21]. The photograph is taken by Dennis Schroeder / NREL.

In the past, the research on VAWTs was neglected due to lack of funding, low fatigue life, and no active control mechanism of VAWTs [6]. Another factor holding the progress of VAWTs back, was their decreased efficiency, caused by the added drag of blades moving against the wind [8]. Still, there are many possibilities relating to rotor design, which make VAWTs more competitive commercially compared to HAWTs, particularly in the relationship between swept area and rotor mass [6]. There is currently a lack of understanding of how specific design factors impact the rotor layout of a contemporary VAWT [5]. Nowadays, research on VAWTs is increasing, as they are shown to have more advantages when placed offshore (as illustrated in Figure 1.4). Currently, VAWTs are receiving more attention from the wind energy sector [22].

Figure 1.4: Multiple vertical axis wind turbines placed in an array, representing an offshore wind farm [23].

Advantages

Various advantages of the VAWTs can be named:

- VAWTs can have simplicity in their design and structure [7]. The blades are easier to manufacture, as the blade design is simple [24]. In addition, VAWTs have fewer components in the power plant [8]. As a result, the expense of maintenance is reduced, also by the easily accessible electrical system at the base of the turbine. The expense of maintaining the turbine is reduced by this feature and by the easily accessible electrical system at the base of the turbine.
- VAWTs have low sound emission due to their low operational tip speed ratio (TSR) which leads to a lower rotational speed of the blades [22].
- VAWTs are omnidirectional, so no yaw control or tail fins are needed [8]. The blades do not need to be oriented in the direction of the incoming wind [9].
- VAWTs have less influence on gust effects and their wake effects are less pronounced. VAWTs have a fast wake recovery [24]. This takes up less space so that VAWTs can be placed closer together

[8][25]. The power density of a wind farm can be raised, leading to a higher energy density per unit of land area.

- It seems that VAWTs can challenge HAWTs in terms of efficiency and cost-effectiveness. Floating VAWTs have the ability to significantly lower their cost of energy (COE) [22]. Additionally, as floating VAWTs dissipate the wakes more quickly when positioned in pairs, they are better suited to wind farm conditions.
- Around cities and metropolitan regions, the pattern and flow of the wind are less predictable. The wind is more chaotic and full of turbulence due to high-rise buildings, trees, and structures [9]. Therefore, large HAWTs are consequently less effective in urban environments. VAWTs can be more desirable and suited for use in urban settings, where they can be installed on-ground or onto buildings and rooftops.

Disadvantages
VAWTs have also a number of drawbacks. The major problem is the fact that VAWTs have serious fatigue issues [24]. The loads vary sinusoidally over one rotation at rather high frequencies, bringing along structural challenges. Second, aerodynamic modeling of VAWTs is difficult due to dynamic stall and other unstable aerodynamic phenomena. The downwind part of the rotor is spinning in its own wake. Due to this, VAWTs become less effective. Moreover, the low rotational speed of the rotor leads to the disadvantage of requiring a more expensive generator. Finally, the VAWT design shows vibration sensitivity.

1.2. Aim of the project

The current advantages of VAWTs give the opportunity to develop a new commercial design of the vertical axis wind turbine. Before constructing such a large new structure, a thoroughly detailed design procedure is required to be carried out [7]. Based on load conditions, the design can be optimized. This way, the rotor design can become competitive and eventually be produced commercially. However, the design space of a VAWT is still very large. Therefore, this thesis looks for the main design drivers of a VAWT design under operating conditions. With this, the main design parameters to pay attention to during the design process can be highlighted. The project starts with validating a reference model, which is discussed in a previous thesis project, ”Structural Optimization of Multi-Megawatt, Offshore Vertical Axis Wind Turbine Rotors” by Mark Schelbergen [5]. From this point on, various design parameters are analyzed for their aerodynamic behavior and aeroelastic stability. Moreover, the rotor can be scaled up to higher Mega-Watt outputs to find scaling trends. Ultimately, the H-rotor design of Huisman is investigated.

1.3. Research questions

The aim of the thesis can be elaborated in research questions, with sub-questions. These are listed below:

1. **What are the design drivers for the design of an H-rotor vertical axis wind turbine?**
   (a) What effects do various design factors have on the aeroelastic stability (in particular resonance), the structural integrity, and the performance of VAWTs?
   (b) How can the aeroelastic stability constraints be included in the optimization of the VAWT design?
   (c) In order to prevent critical failure modes, what trade-offs must be made between maximizing aerodynamic efficiency and ensuring aeroelastic stability?
   (d) What influence does the dynamic stall have on the aerodynamic behavior of a VAWT?
   (e) How do structural changes affect VAWT performance, mass optimization, and aeroelastic stability?
2. **How can the design be scaled up to higher multi-MegaWatt outputs?**
   (a) What are the key findings and trends that the design’s upscaling has revealed?
   (b) What effects does upscaling VAWTs have on their aeroelastic performance and stability at higher power outputs?
   (c) How can aeroelastic stability be preserved and potential resonance problems avoided during upscaling?

1.4. Limitations

The scope of this project is limited to:

- The VAWT can be designed in various types, depending on their shapes. The most known types are the Savonius, H-rotor, and the Darrieus [26]. Due to its simpler construction, the H-rotor is a more economical option than the Darrieus [27]. This thesis investigates only the design drivers for an H-rotor;

- The simulations are done in software provided by DTU (BECAS and HAWC2);
- The aerodynamic, gravitational, and centrifugal loads are implemented in static analyses, as there is no controller available in HAWC2;
- The aerodynamic loads are only applied on the rotor, which can be defined in HAWC2. The aerodynamic performance of the rotor is investigated, therefore, aerodynamics is only applied to the rotor blades. Other components, such as the struts, are not designed aerodynamically yet. Therefore, these components behave more simply and are thought to have less effect on aerodynamic performance. Aerodynamic drag forces can also be applied to other structures, but thus this is not done.
- The wind turbine model is fixed to the ground, there are no hydrodynamic and wave loads;
- The structural model is based on a reference model, a three-bladed H-VAWT with two horizontal struts per blade;
- The aerodynamic profile and material of the model will not be varied for investigating the design drivers;
- The Huisman model is simplified to look into the aerodynamic behavior of the design, though the airfoil is changed;
- No high-fidelity optimization is applied. Therefore, the study is parametric;
- Design drivers are primarily indicated through the validation and verification phase of the project, while research on other design drivers is carried out afterward, which can be compared to literature;
- The models in HAWC2 are investigated on their performance, blade behavior, and aerodynamic loads, with the expanse of other parameters;
- The project scope will be further constrained by the numerous assumptions and simplifications that must be made throughout due to the complexity of the actual structure.

1.5. Overview of the report structure

In Chapter 2, a literature review is presented. This captures a broad field around the vertical axis wind turbine: it describes the history of wind turbines, design, working principle, and upscaling laws. Chapter 3 discusses all various analysis methods, including load analysis, aerodynamic models, and optimization methods. The methodology is given in Chapter 4. The first structural design is elaborated in Chapter 5, which is validated against the reference model in Chapter 6. During the simulations with the reference model, various design drivers can be found and investigated. The results are put in Chapter 6. In Chapter 7, the Huisman VAWT design is simplified and simulated. The results are provided and discussed as well. Finally, Chapter 8 provides the discussion of this project while Chapter 9 concludes the project. The appendices are put at the end of the report.

2

Theoretical background

The literature review is conducted in the beginning phase of the thesis project. It is started with the general history and then the various types of VAWTs are discussed. As the specific type of rotor is known, this design should be studied in further detail. Furthermore, its working principle is explained with expressions for parameters and drawings. Another topic that is considered is the influence of the pitch angle of the blades.

2.1. Overview of history

This section presents a comprehensive overview of the historical evolution of wind turbines. The history goes from ancient Persian windmills to the current wind turbine designs.

2.1.1. First windmills

According to the work of Burton et al. [28], windmills have reportedly been around for at least three thousand years [29]. In order to automate the processes of grinding grain and pumping water, the first windmills were created [30][31]. The earliest known design is the vertical axis system, created in Persia between 500 and 900 A.D. Figure 2.1 displays the ancient Persian windmills, which used the drag component of wind power, resulting in a low efficiency [31]. Vertical sails were constructed of bundles of reeds or wood. These were connected to the central vertical shaft by horizontal struts [30]. Moreover, to work properly, the part rotating in the opposite direction compared to the wind had to be protected by a wall [31]. Obviously, devices of this type can be used only in places with a main wind direction, because there is no way to follow the variations. These wind turbines are still operational today [32]. Furthermore, the oldest known record of a Chinese vertical axis windmill was made in 1219 A.D. This possibly corrects claims that the windmill was invented in China more than 2000 years ago. The island Crete is also known for thousands of white sail-rotor windmills, that pump water for irrigation [30][33]. In Figure 2.2, Cretan windmills can be seen. The sail-type windmills were significantly influenced by sailing ships, which was one of the primary and earliest known applications of wind power in ancient times [28]. Although ancient mariners were aware of lift and employed it frequently, they lacked a physics-based understanding of how or why it functioned this way [30].

Figure 2.1: Ancient Persian windmills of Nashtifan, Khorasan, Iran [34]. The photograph is taken by Kaveh Farrokh in 2017.

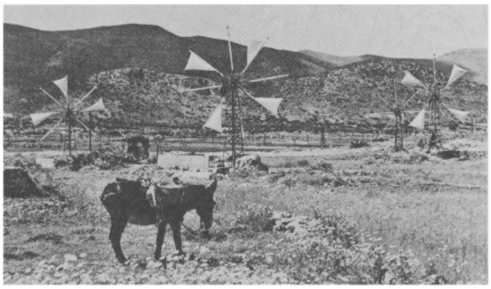

Figure 2.2: Cretan windmills [33].

2.1.2. The beginning in the Western world

The configuration of the horizontal axis wind turbines (HAWTs) was the first to appear in Europe [30]. The idea of windmills was apparently brought by Vikings around the 10th or 11th centuries [29]. The water wheels with horizontal axis configurations might have served as a technological model for the first windmills. Another reason for the switch from vertical axis configurations to horizontal axis configurations could be related to their efficiencies. The horizontal axis configurations have a higher structural efficiency than the vertical axis configurations, which lose up to half of their rotor-swept area due to shielding needs [30].

The first illustrations (1270 A.D.) depict a mill with four blades [30]. The four blades were fixed on a central post, from which the name ”post mill” originates. The mill seemed to be already somewhat advanced in comparison to Persian mills in terms of technology. To convert the motion of the horizontal shaft to vertical movement to turn a grindstone using wind power, these mills utilized wooden cog-and-ring gears. This gear appears to have been modified from Vitruvius’s old horizontal axis water wheel for use on post mills [30]. The main function of these windmills was to pump water, mill grain, saw food, and power tools.

Figure 2.3: A Dutch windmill [35].

As shown in Figure 2.3, the Dutch intended to improve the tower mill design [30]. The traditional post mill was essentially attached to the top of a multi-story tower, with separate floors for grinding grain, removing chaff, storing grain, and housing the wind smith and his family. By pushing a large lever at the back of the mill, both the post mill and its later design had to be oriented into the wind manually. The wind smith had several responsibilities, including maximizing windmill energy and power output and safeguarding the mill from damage by furling the rotor sails during storms [30]. Eventually, the European windmills were improved by sails that generated aerodynamic lift. A higher rotor speed enabled better grinding and pumping action, resulting in increased rotor efficiency.

2.1.3. Improvements in the design over years

It took over 500 years to refine the windmill sail and to make small efficiency improvements [30]. By the end of the process, windmill sails had all the key characteristics that contemporary designers have identified as essential to the functionality of modern wind turbine blades:

1. Camber along the leading edge;
2. Placement of the blade spar at the quarter chord position;
3. Center of gravity at the same quarter chord position;
4. Nonlinear twist of the blade from root to tip.

Additionally, some versions consisted of flaps, spoilers, and aerodynamic brakes. These mills served as the “electrical motor” of pre-industrial Europe. Applications were diverse, including the common water well, irrigation or drainage pumping using a scool wheel, grain grinding, and sawing of wood [30].

2.1.4. Shift in wind turbine use

The horizontal axis windmills were crucial to the rural economy [28]. In total, almost six million mechanical output wind turbines were installed in the United States alone between 1850 and 1970 [30]. For hundreds of years, the turbines were used to pump water in farms, followed by stock irrigation and farm dwelling water requirements. In locations without navigable rivers, very huge windmills with rotors up to 18 meters in diameter were utilized to pump water for the steam railroad trains that served as the main mode of

commercial transportation. However, they were only out with the development of affordable fossil-fueled engines and the subsequent spread of rural electrification [31][30]. In Figure 2.4, a multi-bladed windmill can be seen. Often, they are referred to as fan mills [6]. Beginning with the Halladay windmill in 1854 and continuing with the Aermotor and Dempster designs, which are still in use today, these systems were improved in the US during the 19th century [30]. The earliest attempts to produce electricity were made towards the end of the 19th century and in the first part of the 20th century [31].

Figure 2.4: A typical American windmill to pump water [36].

The American Charles F. Brush constructed what is currently regarded as the first wind turbine for generating electricity in 1887 [37]. For twenty years, this generator kept the batteries installed in his home's basement charged. Despite its size, the generator managed to generate not that much power. Figure 2.5 shows the wind turbine by Brush. Danish scientist Paul la Cour discovered that wind turbines with fewer blades are more efficient at generating electricity. Figure 2.6 depicts the wind turbine by Paul la Cour. The German physicist Albert Betz developed the theoretical underpinnings of the use of wind energy for electricity in Germany during the second decade of the 20th century [37]. In 1919, Betz created the law that bears his name. Nevertheless, Denmark saw the first major advancement in wind energy in Europe by contributing to the construction of the decentralized model for the electrification of the country.

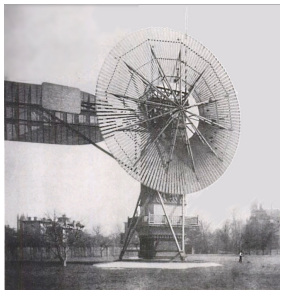

Figure 2.5: The wind turbine by Charles F. Brush [37].

Figure 2.6: The wind turbine by Paul la Cour [37].

Wind energy was not much used other than for battery charging for outlying houses during the 20th century [28]. They even got replaced once there was access to the electricity grid. Wind turbines were still developed further on with new technical advances and enthusiasm, but without any persistent interest in wind generation until the price of oil rose considerably in 1973. The unexpected rise in oil prices sparked numerous significant government-funded research, development, and demonstration programs. This prompted the building of several prototype turbines in the USA, UK, Germany, and Sweden. There was a lot of ambiguity over which architecture would prove to be the most economical, thus various creative designs were thoroughly researched. This led to various vertical axis wind turbines being constructed. These government-funded research programs yielded a wealth of crucial scientific and engineering knowledge [28]. Furthermore, the prototypes generally performed as intended. At first, smaller wind turbines were built, as they were in general easier to repair and modify. Over time, larger and more advanced wind turbines were developed commercially. Nowadays, large wind turbines are recognizable and can be placed in

various terrains. Figure 2.7 illustrates the current design of a horizontal axis wind turbine, which is placed offshore.

Figure 2.7: A floating, conventional horizontal axis wind turbine is placed offshore near Le Croisic, western France [38]. The photograph is taken by Sebastian Salom Gomis.

Governments are looking to lessen their reliance on unpredictable fossil fuel prices and to minimize carbon emissions [30]. Wind energy is emerging as an increasingly appealing alternative. The potential of wind energy to help limit climate change is a key driver for using wind turbines to generate electrical power [28]. Wind power is rapidly establishing itself as a significant component of the world's energy mix [30]. With rated power ranging from a few kW at the beginning to 6 MW and higher for the most current structures, the recent development has resulted in the implementation of a wide range of kinds and models, both with vertical and horizontal axes [31]. Currently, the HAWT type dominates the market for energy generation.

2.2. Types of VAWT

The general design of a vertical axis wind turbine (VAWT) and its historical developments are covered in Paraschivoiu's work [39] [5]. Figure 2.8 depicts the three VAWT principles that are used the most frequently. From left to right, Savonius, Darrieus, and H-rotor are presented. All three types will be discussed in this section.

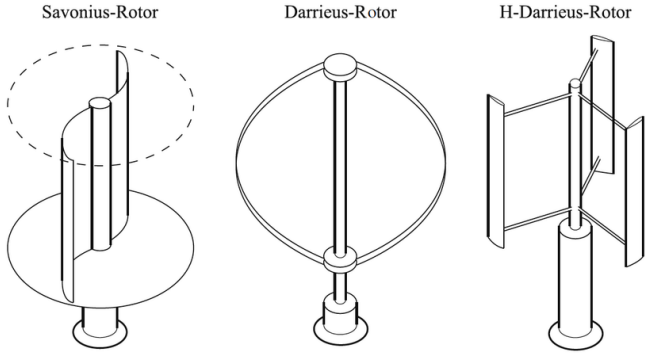

Figure 2.8: Standard types of vertical axis wind turbines [40].

2.2.1. Savonius

Savonius wind turbines were invented by the Finnish engineer Sigurd J. Savonius in 1922. The turbines are among the most straightforward self-starting VAWTs [12]. Johann Ernst Elias Bessler (born 1680) is the first person to attempt to construct a horizontal windmill of the Savonius kind [31]. He did this in the German town of Furstenburg in 1745. However, they are no longer frequently connected to electrical power systems.

Design

The Savonius turbine is a drag-type VAWT [31]. Similar to wind speed anemometers, the design typically has two or three cups, bowls per section, or two half-cylinders facing opposing directions to the wind [9][31]. This is to create an "S"-shaped design that is attached to a vertical shaft. Long helical scoops are used in

some designs to provide smooth torque. The Savonius rotates because of the differential drag and spins at the same speed as the passing wind [12]. It can only rotate in a specific direction. The wind must be directed into the inside of the convex side of the cups on one side and the back of the concave side of the other [9]. The working principle can be seen in Figure 2.9. As a result of the wind being directed between them, the attached vertical shaft moves and rotates. The cups have less drag when rotating in the wind direction and more drag when rotating against.

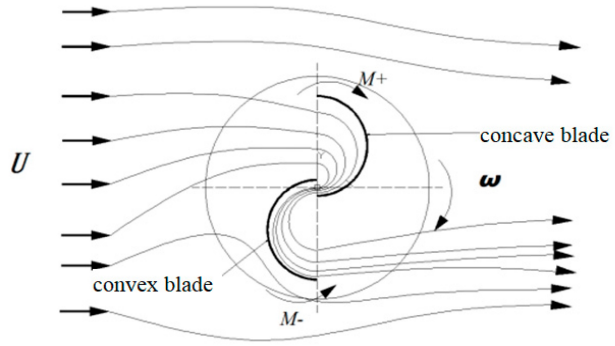

Figure 2.9: The working principle of the Savonius wind turbine [41].

The turbine's rotational speed is limited to that of the wind [31]. This indicates that the tip speed ratio is equal to one or less, which makes this turbine less than ideal for producing energy. Additionally, it is relatively inefficient in comparison to other varieties. Savonius rotors have a large portion of their swept surface close to the ground, which makes the total efficiency of energy extraction decrease due to reduced wind speed at lower heights [12][31].

The simplicity, dependability, and extremely minimal noise generation are its main features [31][9]. Due to the strong torque, especially under these circumstances, it may function well even in low wind conditions (low cut-in wind speed and tip speed ratio). However, because the torque varies, advancements like the helical shape are frequently used. The most widely utilized application of the Savonius wind turbine is the ventilator, which is frequently found on the roofs of vans and busses [12].

2.2.2. Darrieus turbine

French aviation engineer Georges Jean Marie Darrieus invented the "Turbine having its shaft transverse to the flow of the current" [42]. The type eventually carries the name of its inventor. It is the first lift-based VAWT. Darrieus was the first to patent the design in 1931 [5]. His earlier invention from 1927 covers nearly every configuration conceivable employing vertical airfoils [31]. The Darrieus wind turbine is used to produce electricity from the energy carried by the wind [12].

Design

The rotor of the Darrieus wind turbine includes curved blades that are fixed to a vertical shaft (tower) on both ends. It uses two or three thin aerofoil blades or vanes that resemble an egg-beater form [9]. As the blades are arranged horizontally about the central shaft, the blades are simpler to construct and offer higher aerodynamic performance. The "Troposkien" shape of the blades reduces the internal flapwise bending moment brought on by the centrifugal load. Guy cables are typically used by the Darrieus wind turbine to keep the tower steady. The cables are tensioned, mounted to the top of the tower, and fastened to the ground [5].

The blade only produces its full torque twice during a cycle, as the angle of attack shifts when the turbine rotates [31]. The blade then experiences its maximum lift, resulting in massive torque and power (and a sinusoidal power cycle). There is a way to make the blades canted into a helix so that the torque is distributed evenly during the entire revolution, preventing damaging pulsations [12].

Unlike the Savonius, it requires an additional mechanism to start up. This means that for the wind to act as a driving force, the rotor must already be rotating. Sometimes, it has a tiny Savonius rotor attached to it to deliver the necessary beginning torque at low speeds. Nevertheless, the advantage of the Darrieus is that it can operate under a higher tip speed.

Examples

The largest VAWT (diameter of 64 meters) in existence today is the Lavalin Éole Research Turbine, constructed in Canada in the 1980s [5][43]. The Lavalin Éole is highlighted in Figure 2.10. The turbine

produced a peak amount of power of over 1.3 MW. The rotor speed and cut-out speed were restricted due to fatigue and in order to properly run under a five-year energy purchase agreement. Due to the bottom bearing's premature failure, the turbine was turned off in 1993.

Figure 2.10: The Lavalin Éole is the largest VAWT, standing in Québec, Canada. It is a Darrieus wind turbine [43].

Sandia National Laboratories (SNL) carried out research on VAWTs, on which Sutherland et al. [44] provide an overview. SNL started with research on VAWTs with small diameters in the 1970s [5]. Later, the 34 m Test Bed turbine was constructed in 1987 and Figure 2.11 gives a view of the Sandia Test Bed VAWT. As it says in the name, the turbine was made for research of fundamental physics and had numerous sensors to collect measurements. The measurements serve to validate the analytical models and design codes. The design was extremely conservative and adaptive, allowing for the mounting of several blades. The turbine had specific stall characteristics to prevent the rotor from producing too much power at high wind speeds. A modal test was used to identify the natural frequencies of the stationary turbine. The outcome determined the rotor speed operation range. The measured data was used to provide a first view of the fatigue load spectra. However, the buildup of insect waste on the blades during operation hampered the performance of the wind turbine. The blade stall was affected and delayed by the accumulation. This caused the turbine to produce more power at wind speeds when stall would typically happen [5]. No significant performance change was seen when vortex generators were placed close to the outer blade connection and blade-tower connection.

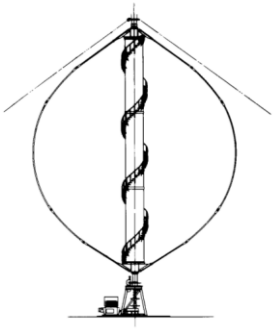

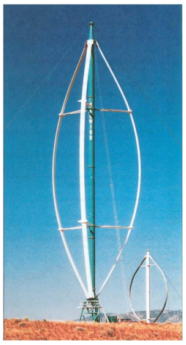

Figure 2.11: The Sandia Test Bed VAWT [44]. **Figure 2.12:** The FloWind wind turbine [44].

Additionally, the FloWind Corporation attempted to use the Darrieus wind turbine on a big scale in California from 1982 [31]. However, the business failed in 1997. FloWind had over 170 turbines with a diameter of 19 meters that produced 250 kW of power at a wind speed of 20 m/s [5]. In 1992, a new rotor was created for their outdated fleet to reduce fatigue and increase power output [44]. However, the aluminum blades required a lot of maintenance due to fatigue. The Sandia Point Design served as the basis for this redesigned rotor, which was called the expanded height-to-diameter rotor. The new rotor had three fiberglass-made blades, which had to be bent into place [5]. This increased their out-of-plane bending moment. Furthermore, they required struts in order to lessen vibrations. This contributed to the overall cost. The design increased resonance stability while reducing the size of the torque tube. With different airfoils, the turbine was improved. Furthermore, to prevent buckling, a thicker skin thickness

was added. The need for resonance stability resulted in increasing the number of blades as the most economical option. Figure 2.12 showcases the FloWind wind turbine.

2.2.3. H-rotor

Georges Darrieus also created the straight-bladed wind turbine, also known as the Giromill or H(-Darrieus)-rotor, as a sort of vertical axis wind turbine in 1927 [31]. The study team of Musgrove examined this type of VAWT in the United Kingdom in the 1980s. The H-configuration model was mostly developed in the UK [5]. The H-rotor works well in turbulent wind conditions and offers a good alternative in places where HAWTs are unsuitable.

Design

The blades of the common Darrieus are replaced with straight, vertical blade sections that are linked to the central shaft with horizontal supports (struts) [31]. Typically, these turbines have two or three vertical airfoils. Although the H-rotor blade design is significantly easier to construct than the conventional arrangement, it produces a more massive structure and calls for stronger blades. Since the generator in these turbines sits at the base of the tower, it can be larger and heavier than a typical HAWT generator, while the tower's structure can be lighter. The Giromill can self-start by pitching the downwind moving blade flat to the wind [12]. They create drag and start the turbine spinning at low wind speed. This allows for practically constant torque generation over a wide angle. However, the blade pitching mechanism is complex and heavy, while a wind-direction sensor must be included.

A H-rotor operates in a similar way as a standard Darrieus turbine. When the wind strikes the blades, its velocity is divided into components for lift and drag [31]. The turbine rotates as a result of the vector sum of these two components of velocity.

Examples

The 500 kW VAWT-850 was constructed in 1989 at the Carmarthen test site, being the largest H-rotor (45 meters tall, 38 meters diameter) in all of Europe [31]. Inside the top of the tower, an induction generator and gearbox were placed. The turbine ran until February 1991, when a flaw in the production of the fiberglass blades caused one of the blades to break. The swept area of the rotor is denoted by the numbers in the turbine name [5]. It was determined through experiments on the VAWT-450 that reefing the blades was not necessary for effective management of the power output and blade loading (using passive stall regulation). As a result, the variable geometry mode of the VAWT-450 was discontinued. The VAWT-850 was created to demonstrate the improvements made in the H-type VAWT developments. It was designed with the goals of providing excellent reliability throughout its 30-year design life and low cost [5].

In the 1990s, the German business Heidelberg Motor GmbH designed and constructed a number of 300 kW prototypes using large-diameter direct-drive generators [31]. The generator was situated on the ground in some turbines, while it was mounted on the top of the tower in others. After the development of a 12 kW prototype in Uppsala, Sweden, the largest VAWT in Sweden was developed and built in Falkenberg by VerticalWind AB in 2010. The H-rotor had three blades and a tower made of wood composite, which makes the turbine less expensive than other turbines made of steel. The VAWT was designed to reach a rated power of 200 kW.

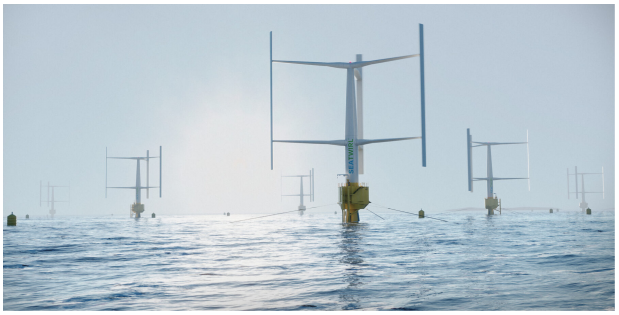

Figure 2.13: The H-rotor VAWT design of SeaTwirl [45].

Currently, SeaTwirl works on producing a VAWT. SeaTwirl was established in Gothenburg in 2012 [46]. Their first prototype (the S1) was produced in 2015, which can generate up to 30 kW. In 2023, SeaTwirl is currently developing a full-scale model (the S2), which can generate up to 1 MW. The design is shown in Figure 2.13. The goal of SeaTwirl is to develop larger wind turbines to dominate the offshore market by 2030.

2.2.4. Vane type Vertical Axis Wind Turbine (VVAWT)

The technical characteristics of existing wind turbine designs demonstrate the need to develop a new class of wind turbines that can capture wind force to its fullest potential while having a broad range of applications [12]. The new class wind turbines should maximize the usage of wind kinetic energy up to the Betz limit and reduce the geometrical sizes in the active area of blades or vanes. Vane-type vertical axis wind turbines (VVAWT) can address this issue. This type of wind turbine uses drag force from the active area of the working elements and has a straightforward construction and production process.

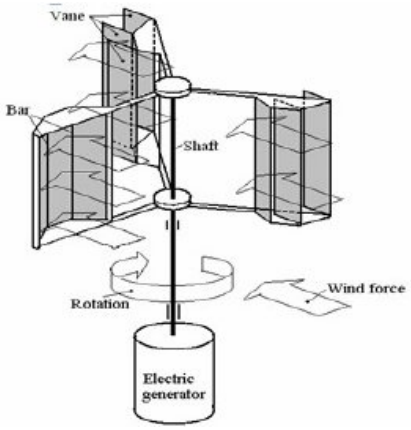

Figure 2.14: Sketch of a Vane type Vertical Axis Wind Turbine (VVAWT) [47].

The VVAWT is a unique design that consists of moveable vanes that, when closed, form a scoop shape. The scoop shape of these frames makes them more aerodynamic while increasing the torque. To lessen the negative torque, movable vanes on the opposite side of the impeller are first opened by the action of the wind through three frames with angles of 120° between. Another design for the VVAWT has four frames with angles of 90° between one. It has horizontally constructed bars with vanes that have the ability to twist at 90°. Bars should be used to link vertical frames in order to boost the construction's stiffness.

2.2.5. Propeller type wind turbines

Due to the shape and geometry of the blades, modern propeller-type wind turbines employ the wind lift force as an aircraft wing and are not constructed with a large number of rotor blades or particularly wide blades [12]. The performance of the wind turbine is significantly impacted by the number of its blades, while the stability of the turbine is decreased by a large number of rotor blades. These types of wind turbines are built on the tower. Guy wired cannot be used to support one, as the propeller spins both above and below the tower. The strength of the tower must increase considerably with the size of the propeller. Besides, the majority of the wind passing through the area between the blades will entirely miss them, preventing the blades from using the wind's kinetic energy. The actual efficiency of these types of turbines lies around 20%.

2.3. Rotor design

In this section, a comprehensive exploration of the rotor design for the VAWT is delved into, providing a nuanced understanding. Firstly, the general design of the turbine is discussed. Furthermore, the next subsections put emphasis on the blade and its design.

2.3.1. Turbine design

The specific vertical axis wind turbine of this project is the H-rotor with three blades. An example of the design is shown in Figure 2.15. The number of blades is actually a crucial design parameter. The number of blades decision is ultimately a balance between the blade stiffness, aerodynamic efficiency, and economic factors [48].

The swept area of the H-rotor design can be expressed as the diameter of the turbine (D) times the blade length (H), as can be seen in Equation 2.1 [46].

$$A = DH = 2RH \tag{2.1}$$

The rotor aspect ratio can be defined as $AR = H/D$, which describes the relationship between the rotor diameter and the blade length. The work of Ahmadi-Baloutaki et al. [49] demonstrated that, from an aerodynamic perspective, a rotor aspect of between 0.5 and 2 is ideal, while the best performance is found with a rotor aspect ratio of 1 [46].

Furthermore, the number of struts per blade and their placements are crucial factors for the structural design as well. The work of Ahmadi-Baloutaki et al. [49] and Hameed et al. [50] demonstrated that the optimum placement of two struts, to reduce bending stresses and have the most optimal bending stress distribution along the blade, is at 21% and 79% of the blade length [46]. The work of Ahmadi-Baloutaki et al. [49] carries out a parametric optimization for a number of design parameters (such as the solidity, blade aspect ratio, and rotor aspect ratio). The goal of the optimization is to increase the turbine power coefficient (C_p) and its operational range. The most severe strains affecting the blades and supporting struts are identified by aerodynamic loading analysis.

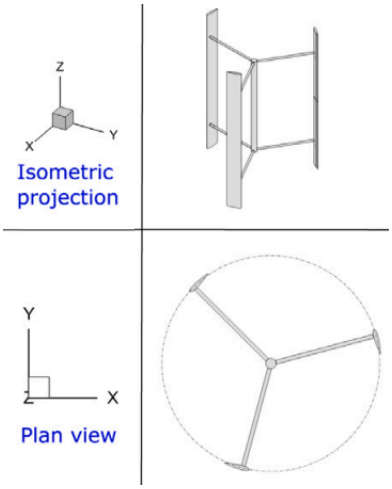

Figure 2.15: Isometric projection and plan view of a three-bladed, H-rotor VAWT, adapted from Hand et al. [48].

2.3.2. Blade design

An aerodynamic and structural compromise is made in the design of a wind turbine blade [51]. For HAWTs, the design of the outer two-thirds of the blade is typically dominated by aerodynamic factors, whereas the inner one-third of the blade is typically dominated by structural factors. The blade is often segmented into blade elements for the aerodynamic analysis, as can be seen in Figure 2.16.

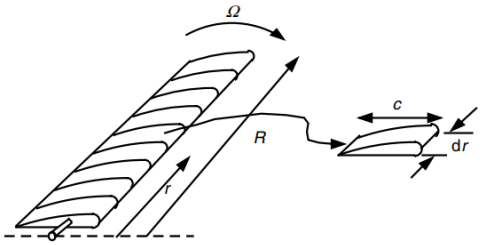

Figure 2.16: Visualization of blade elements, in which c represents the airfoil chord length, r the radius, dr the radial length of element, R the rotor radius and Ω represents the angular velocity of the rotor [32].

The blade has an aerodynamic profile, an airfoil. The NACA 4-digit series of airfoils is one of the most popular profiles for wind turbine blades [46]. The front point of the airfoil is called the leading edge, and the back point is called the trailing edge. The chord (c) is a straight line that runs from the leading edge to the trailing edge. The first two digits indicate the potential asymmetry of the airfoil (the camber) and its position. The final two digits provide the maximum thickness of the chord in %. The nomenclature of an airfoil is visible in Figure 2.17.

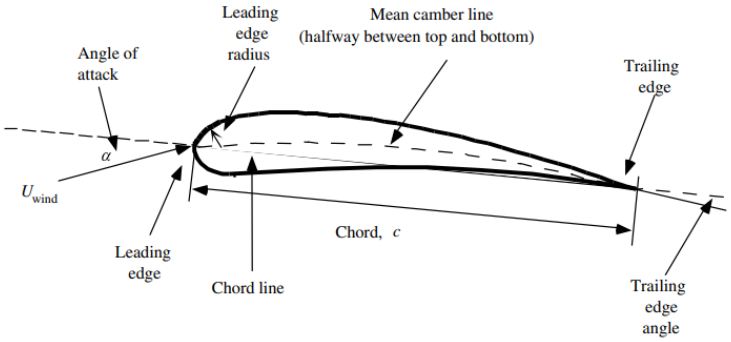

Figure 2.17: Nomenclature of an airfoil [32].

Figure 2.18 visualized the cross-section of a wind turbine blade. The blade is normally hollow from a structural standpoint. Often, shear webs are placed to transfer shear loads. The internal longitudinal spar caps and shear webs carry the shear loads and the main part of the bending loads. They also prevent the skin panels from buckling and the cross-section shape from deforming. The skin forms the aerodynamic shape while carrying torsional loads and partly bending loads [52].

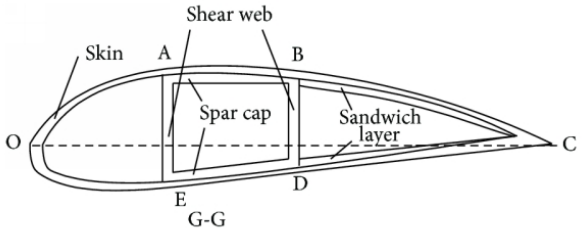

Figure 2.18: The cross-section of a wind turbine blade [53].

2.3.3. Blade material

As mentioned before, the original blades were made of metal. The blades of the Sandia Test Bed were made of aluminum [5]. Later on, blades were made of full composite. The blades of the VAWT-850 and FloWind were made of Glass Fiber Reinforced Plastics (GFRP). The blades of the FloWind turbine were made using pultrusion technology. Large turbine blades currently in use in industry are made of fiber composite materials to produce a rigid, lightweight design with a high fatigue life [54]. Furthermore, composite (horizontal axis) wind turbine blade manufacturing methods have advanced significantly in recent years [5]. Modern production methods allow for greater freedom in blade shape.

CFRP

Carbon Fiber Reinforced Polymers (CFRP) are composites made of polymers acting as the matrix and carbon fibers as the reinforcing material [55]. Low density, high strength, and high stiffness are all characteristics of carbon fibers. The fibers have good mechanical characteristics and are lightweight when they are arranged in staple or filament form. They can endure temperatures of up to 3000 degrees Celsius while retaining structural integrity. Additionally, their coefficient of linear heat conductivity is extremely low. At room temperature, they are unaffected by moisture, the majority of solvents, acids, or bases. CFRPs are advantageous for a wide range of applications, including in the aeronautical and automotive world. This is thanks to these unique features. Nevertheless, they are highly electrically conductive, expensive, and sensitive to production quality [56].

GFRP

GFRP stands for Glass Fiber Reinforced Plastics. GFRP is a cheap material that has good static and fatigue properties [56]. However, it has a relatively low Young's modulus, which leads to the need for very thick spar caps in the blade. Most blades are made of GFRP [5].

Coating

To protect the blades from environmental damage, coatings can be applied during or after molding [48]. A gelcoat coating can be used during the in-mold process to offer the composite a better aerodynamic surface and provide protection from UV radiation, moisture absorption, and erosion. Since the coating is not a structural element, it does not increase the blade's mass. To facilitate the application of gel coat, a material known as Nexus is frequently utilized.

2.3.4. Fiber orientations

Composites have various advantages. They allow for more blade geometry flexibility and modification of the mechanical properties of laminates [5]. The stiffness and strength of the laminates can be adjusted in any direction by adjusting the fiber orientations.

The standard fiber orientations for wind turbine blades are 0°, +45° and -45°, with 0° being parallel to the blade span direction or pitching axis [54]. Plies with 0° are used to resist bending, while plies with +45° fibers are used to resist torsional stiffness and buckling resistance. Although there are other possible combinations with the fiber directions, the 0/$\pm$45° ply layup is the most useful from a manufacturing perspective. In Table 2.1, the structural members in a wind turbine blade (HAWT) are written down alongside their fiber angle and function.

Table 2.1: An overview of the structural members in the wind turbine blade, with their fiber angle and function described, adapted from Schelbergen [5].

Structural member	Fiber angle	Function
Shear webs	$\pm$ 45°	Carry transverse loads
Spar caps / Girders	0°	Carry bending loads
Skin	$\pm$ 45°	Subjected to aerodynamic loads, Transfer the loads

2.3.5. Weight distribution

Normal weight distribution is written down in Table 2.2, for a small wind turbine. The horizontal axis wind turbine has a blade of 48.8 m with a mass of 10.7 tonnes and produces 2.5 MW [5].

Table 2.2: The weight contribution from the materials in the horizontal axis wind turbine blade [5].

Material	Weight contribution [%]
Dry fibers	
45° / -45° / 0°	25
$\pm$45°	2
UD	25
Resin	34
Paste	2
Steel	2
Rest	10

2.4. Aerodynamics

The production of power by the wind turbine depends on the interaction between the rotor and the wind [28]. The aerodynamic forces created by the mean wind determine wind turbine performance. As a result, this section elaborated on the rotor's aerodynamics.

2.4.1. Momentum theory

A simple model, commonly credited to Betz [57], can be used for various determinations. The output and thrust from an ideal turbine rotor and the effect of the rotor operation on the local wind field can all be calculated using this model [58]. The model is based on the linear momentum theory.

The surface of a stream tube and two cross-sections of the stream tube serve as the control volume boundaries. The only flow is across the ends of the stream tube. The wind turbine is represented by a uniform "actuator disk", which creates a discontinuity of pressure in the stream tube of air flowing through it. Visualization can be seen Figure 2.19. Furthermore, it should be noted that the analysis is not limited to any type of wind turbine.

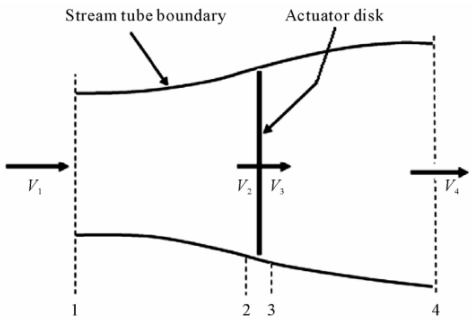

Figure 2.19: Visualization of the actuator disk model of a wind turbine [58]. The air velocity is given with V, positioned at four different locations (1,2,3,4).

Assumptions
The model is based on certain assumptions listed below:

1. Homogeneous, in-compressible (constant density), and steady-state fluid flow;
2. No frictional drag;
3. An infinite number of blades;
4. Uniform thrust over the disk or rotor area;
5. A non-rotating wake;
6. The static pressure far upstream and far downstream of the rotor is equal to the undisturbed ambient static pressure.

Thrust
It is possible to determine the net force acting on the contents of the control volume by applying the conservation of linear momentum to the control volume containing the entire system [57][58]. The thrust (T) which is the force of the wind on the wind turbine, is equal to and opposing to that force.

The thrust is equal to and in the opposite direction of the change in momentum of the air stream, according to the conservation of linear momentum for a one-dimensional, in-compressible, time-invariant flow. The expression is shown in Equation 2.2, in which ρ is the air density, A is the cross-sectional area, V is the air velocity and the subscripts represent at which locations it is positioned (see: Figure 2.19). For steady flow, an assumption can be made for mass flow rate $\dot{m} = (\rho AV)_1 = (\rho AV)_4$.

$$T = V_1(\rho AV)_1 - V_4(\rho AV)_4 = \dot{m}\,(V_1 - V_4) \tag{2.2}$$

Furthermore, the velocity behind the rotor (V_4) is lower than the free stream velocity (V_1). This is because the thrust is positive. On each side of the turbine, no work is done. Therefore, the two control volumes on either side of the actuator disk can use the Bernoulli equation. In Equation 2.3, this is shown for the stream tube upstream and downstream of the disk respectively. It is assumed that the far upstream and downstream pressures are equal to each other ($p_1 = p_4$). Another assumption is that the velocity across the disk remains the same ($V_2 = V_3$).

$$p_1 + \frac{1}{2}\rho v_1^2 = p_2 + \frac{1}{2}\rho v_2^2 \qquad\qquad p_3 + \frac{1}{2}\rho v_3^2 = p_4 + \frac{1}{2}\rho v_4^2 \tag{2.3}$$

The net total of the forces acting on the actuator disc's two sides can be used to calculate the thrust as follows in Equation 2.4. Combining both expressions for the thrust force, the velocity V_2 can be found. This represents the wind velocity at the rotor plane. It is the average of the upstream and downstream wind speeds.

$$T = A_2\,(P_2 - P_3) = \frac{1}{2}\rho A_2\left(V_1^2 - V_4^2\right) \qquad\qquad V_2 = \frac{V_1 + V_4}{2} \tag{2.4}$$

The axial induction factor (a) is the fractional decrease in wind velocity between the free stream velocity and rotor plane. With these new expressions, the axial thrust on the disk can be defined.

$$a = \frac{V_1 - V_2}{V_1} \qquad\qquad T = \frac{1}{2}\rho A V_1^2[4a(1-a)] \tag{2.5}$$

2.4.2. Airfoil aerodynamics

As the analysis is done on an H-rotor wind turbine, the focus only lies on lift-driven VAWT. This model is known as its simplest type of wind turbine, but its aerodynamic analysis can be quite complex [58]. The torque produced by the lift on the blades is what gives the rotor its power [8].

Velocity components
A 2D blade element, as illustrated in Figure 2.20, is considered to comprehend the aerodynamic properties of a VAWT [24]. As the turbine rotates through the wind, two distinct components of velocity can be

observed: the wind (V_∞) and the rotational speed ($\omega \cdot R$). Moreover, the turbine creates a force field inside the flow, causing an induced velocity (V_{ind}). The magnitude of this induced velocity changes over rotation while also being influenced by the thrust coefficient of the turbine.

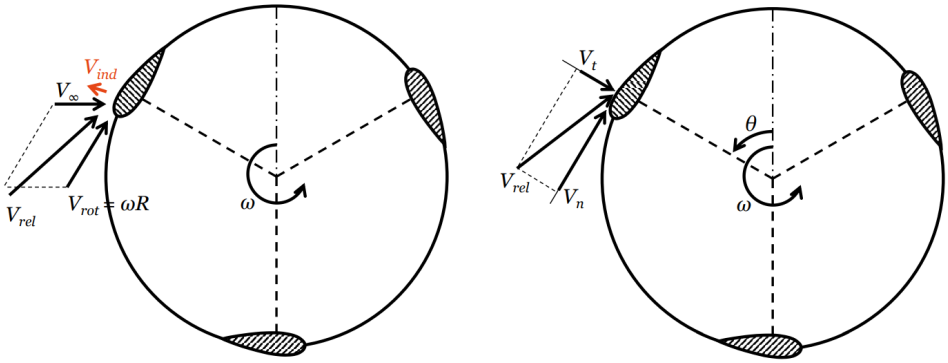

Figure 2.20: Velocity components acting on a 2D blade element [24].

The velocity components can be decomposed into directions of interest. The blade's perceived velocities both normal to and tangential to the spinning path are important for the analysis. These are found below.

$$V_x = V_\infty + \omega R \cdot \cos\theta + V_{ind,x} \tag{2.6}$$
$$V_y = \omega R \cdot \sin\theta + V_{ind,x} \tag{2.7}$$
$$V_t = V_x \cdot \cos\theta + V_y \cdot \sin\theta \tag{2.8}$$
$$V_n = V_x \cdot \sin\theta - V_y \cdot \cos\theta \tag{2.9}$$
$$V_{rel} = \sqrt{V_x^2 + V_y^2} \tag{2.10}$$

Overview of angles
First, a quick overview of all the angles used in this section is given [24]:

- The azimuth angle is defined with θ, and it is the angle between the y-axis and the airfoil location;
- The angle of attack is defined with α or AoA, and it is the angle between relative velocity and the airfoil chord line;
- The inflow angle is defined with Ψ, and it is the angle between relative velocity and tangent to the rotating plane;
- The pitch angle is often defined with θ_p, and it is the angle between the airfoil chord line and tangent to the rotating plane.

The angles and forces are also illustrated in Figure 2.21.

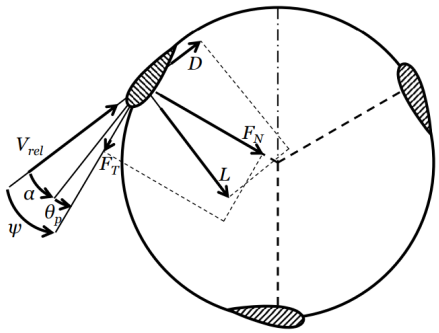

Figure 2.21: Angles and forces acting on a 2D blade element [24].

Angle of attack
From the velocity triangle, the angle of attack (α, AoA) can be calculated with Equation 2.11.

$$\alpha = \text{atan}(\frac{V_n}{V_t}) \tag{2.11}$$

Lift and drag force
The lift and drag forces act on the blade and are called the aerodynamic forces. For a specific airfoil shape, the lift and drag coefficients (C_L, C_D) can be determined as a function of the angle of attack. The lift and drag forces are tangential and in line with the relative velocity.

$$L = \frac{1}{2}\rho V_{rel}^2 C_L(\alpha) \cdot c \tag{2.12}$$

$$D = \frac{1}{2}\rho V_{rel}^2 C_D(\alpha) \cdot c \tag{2.13}$$

Normal and tangential force
The lift and drag force can be decomposed into normal and tangential force using the inflow angle (Ψ).

$$F_N = L\cos\Psi + D\sin\Psi \tag{2.14}$$

$$F_T = L\sin\Psi - D\cos\Psi \tag{2.15}$$

Power
The power is the rate at which work is done and that work is defined as the force applied over a distance, x [24]. By multiplying the rotational velocity (ωR) with the average tangential force, the average power over one revolution is acquired. The average tangential force can then be calculated by integrating the tangential force across one rotation and multiplying it by the number of blades (B).

$$P = \frac{1}{2\pi}\int_0^{2\pi} B \cdot F_T(\theta) \cdot \omega R \cdot d\theta \tag{2.16}$$

Power coefficient
The power coefficient (C_p), which equals the proportion of extracted to available power in the swept area, is a measure of efficiency [6]. Equation 2.17 shows the expression for the power coefficient. In this expression, P stands for the converted power, ρ for the air density, V_∞ for the undisturbed wind speed, and A for the swept rotor area.

$$C_p = \frac{P}{0.5\rho A V_\infty^3} \tag{2.17}$$

The Betz limit shows that the theoretical maximum value of the power coefficient is $C_p = 0.59$. For HAWTs, the power coefficient lies around 0.4 and 0.5 [46]. VAWTs have a lower power coefficient than HAWTs. Turbines with a different rotor aspect ratio but with the same swept area can generate the same output power. As can be seen in Figure 2.22, the swept area can be held constant by varying the rotor aspect ratio. However, the rotor aspect ratio will have an impact on the structural and aerodynamic performance, in reality [46].

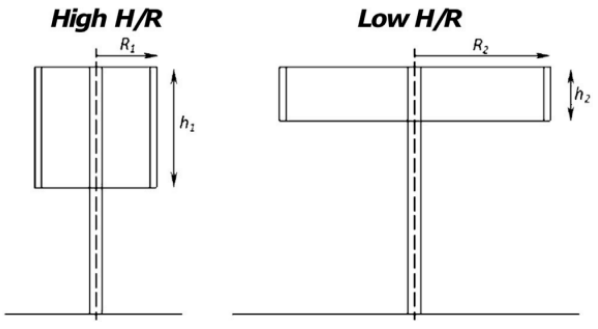

Figure 2.22: Two VAWTs with different rotor aspect ratios can hold a constant swept area [48].

Thrust
The average thrust can be found by calculating the average x-force of all blades over one revolution [24]. The thrust can be calculated with Equation 2.18.

$$T = \frac{1}{2\pi} \int_0^{2\pi} B \cdot (F_T(\theta)\cos(\theta) - F_N(\theta)\sin(\theta)) \cdot d\theta \tag{2.18}$$

The thrust coefficient can be calculated with Equation 2.19.

$$C_T = \frac{T}{\frac{1}{2}\rho A V^2} = \frac{\text{Thrust force}}{\text{Dynamic force}} \tag{2.19}$$

Gravity force and centrifugal load force
The gravity force (F_g) and the centrifugal load force (F_c) are dependent on the mass. The expressions are shown in Equation 2.20 and Equation 2.21, in which m_i and r_i are the mass and radius position of a discretized element, ω is the angular velocity and g is the acceleration of gravitation [46].

$$F_c = \sum_{i=1}^{n} m_i r_i \omega^2 = m\omega^2 R \tag{2.20}$$

$$F_g = \sum_{i=1}^{n} m_i g = mg \tag{2.21}$$

Tip speed ratio
The tip speed ratio (TSR, λ) of a VAWT is defined by Equation 2.22. The tip speed ratio measures how quickly the wind turbine is spinning in relation to the undisturbed wind speed [6].

$$\lambda = \frac{R\omega}{V_\infty} \tag{2.22}$$

Solidity
The solidity (σ) is the total area of the blades divided by the swept area [46]. The solidity is expressed in Equation 2.23, in which B represents the number of blades, c the chord, and R the rotor radius. Even though the optimal solidity varies for VAWTs, studies show that the optimal solidity lies around 0.2 to 0.6 [49][46]. In the swept area, the solidity represents the percentage of occupied space [6].

$$\sigma = \frac{Bc}{2R} \tag{2.23}$$

Strouhal number
The Strouhal number (St) is a dimensionless quantity that relates the frequency of vortex shedding to the characteristic length and velocity of the flow. It is defined in Equation 2.24. In this expression, f is the frequency of the shedding vortex, L is the characteristic length (such as the diameter or height) and V is the velocity. The Strouhal number was developed to address period fluid flows [59], while it also sheds light on the instability and vortex shedding in the flow.

$$St = \frac{fL}{V} \tag{2.24}$$

Aspect ratio
As mentioned before, the aspect ratio (AR) can be defined as the ratio between the blade length (H) and the rotor diameter (D).

$$AR = \frac{H}{D} \tag{2.25}$$

Segmentation of wind turbine path
The position of the blade along its rotation can be determined by its path: upwind (UW) or downwind (DW). Figure 2.23 visualizes this.

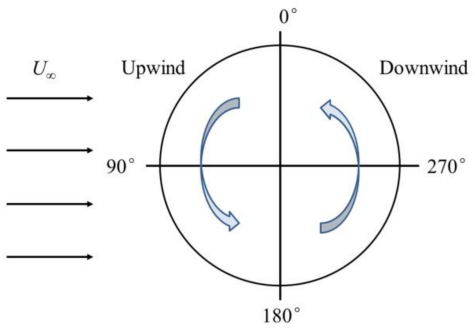

Figure 2.23: The upwind and downwind paths of a VAWT [60].

2.5. Unsteady aerodynamics

The complex unsteady aerodynamics and cyclic loads on the drive train, tower, and blades are of great concern for VAWTs [61]. Therefore, unsteady aerodynamics is a key factor in VAWT designs [24]. The performance of VAWTs is significantly impacted by some unstable occurrences, which should not be disregarded.

2.5.1. Dynamic stall

The development of VAWTs has been impeded due to the occurrence of dynamic stalls, which leads to low efficiency and structural unreliability of the wind turbines [62]. VAWTs face the issue of operating at lower tip speed ratios to maximize their peak aerodynamic performance while experiencing dynamic stall or avoiding dynamic stall at the expense of lowering peak performance.

Definition
When the airfoil is experiencing abrupt changes in the angle of attack, the term ”dynamic stall” is used to describe the coupling effects of the trailing edge (TE) separation and the leading edge (LE) separation. This constant variation in the angle of attack normally occurs during VAWT operation and should be taken into consideration while simulating [61]. Dynamic stall is mostly present at low tip speed ratios. The amplitude of the angle of attack rises with decreasing TSRs. Figure 2.24 shows the normal coefficient (C_N) as a function of the angle of attack (α), while the stages of dynamic stall are named.

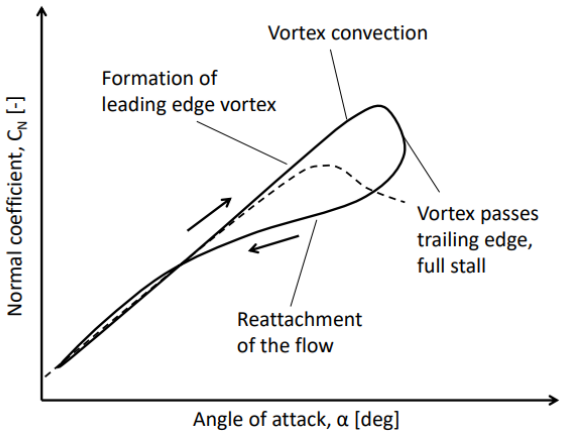

Figure 2.24: The normal coefficient (C_N) as a function of the angle of attack (α), while the stages of dynamic stall are named [24].

Stages
The dynamic stall effect can be explained in its five stages:

1. Leading edge separation will commence;
2. Leading edge vortex will form;
3. The flow will entirely separate;
4. The flow will start to reattach;
5. The flow aerodynamic loads will restore to the pre-stalled state.

Figure 2.25 illustrates these stages of dynamic stall around an airfoil.

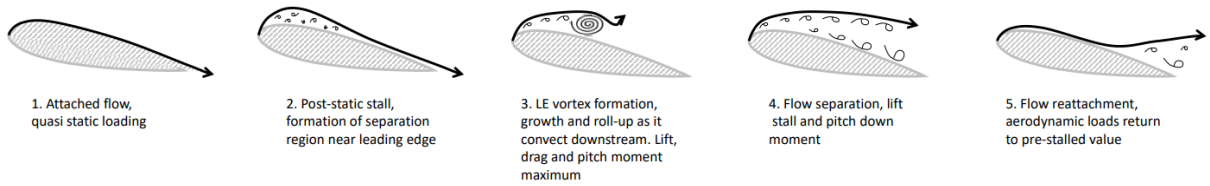

Figure 2.25: Stages of dynamic stall [24].

VAWTs

When a VAWT is running, the implications of dynamic stall are fairly complicated [61]. Figure 2.26 depicts the vortex shedding structure of a Darrieus wind turbine at a low tip speed ratio (λ =2.14). It is demonstrated that the flow is completely divided when the blade passes Quadrant III because both the leading and the trailing edge vortices are released and washed away. This may be caused by both blades' circling motion and the turbulent flow. Some models (like the Beddoes-Leishman) take the vortex shedding into account. This can be achieved by simulating the rapid release of trailing and leading edge vortices. The delay in the angle of attack, leading-edge separation point, and vortex lift are adjusted to zero when the blade reaches Quadrant III (see: Figure 2.26).

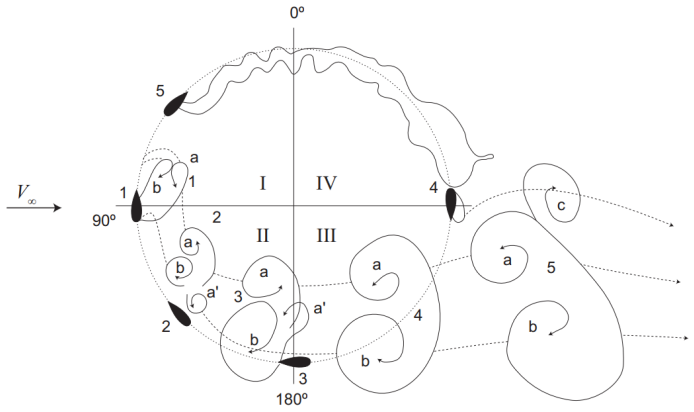

Figure 2.26: Visualization of the flow under the dynamic stall situation at $\lambda = 2.14$ when a Darrieus turbine is rotating [61].

Importance

Due to the difficulties in regulating pitch, VAWTs are often stall-regulated [61]. Stall regulation is a common method for power regulation, especially in offshore VAWT designs [63]. The aerodynamic, structural, and generator designs must adhere to a number of restrictions imposed by stall regulation. A VAWT experiences unstable and azimuthally changing aerodynamics, which makes designing an airfoil for stall correction extremely difficult.

As a result, the impact of dynamic stall is crucial to how VAWTs function [61]. When the rotational velocity is constrained by high wind speeds, the tip speed ratio drops, increasing the amplitude of the angles of attack (for VAWTs with fixed blades). Consequently, the blades enter a stall and the lift force decreases. Then, the dynamic stall passively controls VAWT blades, hence it is crucial to take this into consideration while modeling the turbine. Additionally, with dynamic stall, the amplitude of the oscillations of the blade forces changes, which is connected to fatigue issues. Due to a shortage of experimental data, studies on the VAWT blade loads during the dynamic stall are limited.

2.5.2. Blade-vortex interaction

Another unstable phenomenon for VAWTs can be described as the blade-vortex interactions [24]. The rotating blades shed vorticity into the wake, as shown in Figure 2.27. Moreover, the blades of the rotor are essentially moving through the wake created by the upwind portion as they move downwind.

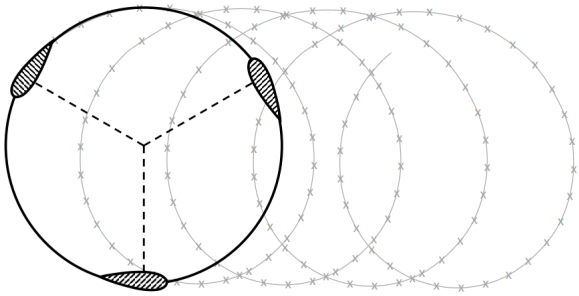

Figure 2.27: Visualization of blade-vortex interaction [24].

2.5.3. Flow curvature

Another phenomenon for VAWTs is flow curvature, as depicted in Figure 2.28. Due to the rotor's rotation, each individual blade segment will experience a curvilinear inflow [24]. This will cause the flow properties, like the angle of attack along the chord, to vary. An additional incidence angle can be introduced, as the airfoil would have an additional camber if converted from a geometric airfoil to a rectilinear flow.

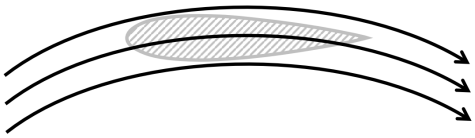

Figure 2.28: Visualization of flow curvature [24].

2.5.4. Dynamic inflow

The last phenomenon discussed under unsteady aerodynamics is dynamic inflow. Dynamic inflow describes the unstable relationship between the induction and the unstable loading and/or momentum of the flow [24]. This means that the velocity field will respond gradually if the loading on the rotor changes instantly (for example, with blade pitching). The response time shall take a while, and this is what dynamic response is referred to. In Figure 2.29, a comparison between static and dynamic response is illustrated over time for the induction factor (a).

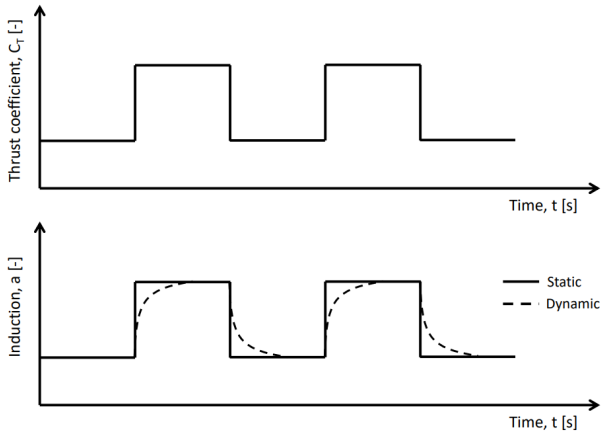

Figure 2.29: Dynamic inflow: dynamic and static response of the thrust coefficient (C_T) and the induction factor (a) as a function of time (t).

2.6. The influence of the pitch angle of the blades

As mentioned before, the vertical axis configuration is thought to enable significant reductions in the cost of electricity for floating offshore turbines [64]. Turbine loading must be restricted at high wind speeds for this to happen. Blade pitch is thought to be a method for achieving this.

Variable pitch

A variable pitch approach is used to enhance VAWT performance by altering the angle of attack (α) [65]. Variable pitch is not a feature of the VAWT design by default [66]. Instead, the blade is often positioned so that the chord line is tangential to the turbine's circle. When the pitch angle is equal to zero, this is referred to as fixed pitch.

In the design of a VAWT, changing the blade pitch can be used for a variety of purposes, such as increasing starting torque, maximizing power capture, maintaining power levels in operations at wind speeds greater than the rated wind speed, or reducing cross-sectional area during survival wind speed events at sea [64].

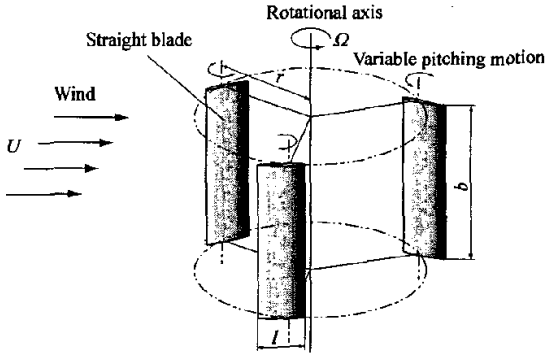

Figure 2.30: Vertical axis wind turbine with variable pitch [67].

Optimizing output with pitch

The key distinction between HAWT and VAWT is, that the conventional wind turbine without pitch would have a constant angle of attack at all azimuthal angles [66]. For the VAWT, the angle of incidence varies in cycles, resulting in a varying relative velocity and angle of attack. Consequently, the lift and drag forces are affected by the cyclical behavior of the angle of attack. This leads to a higher power coefficient (C_p) for the frontal half of the turbine (the half that faces the incoming wind) and a lower power coefficient for the back half. Therefore, the pitch can be individually adjusted to a specific magnitude (as can be done to optimize HAWT), but it will still act in that cyclical motion. It will not optimize power production for all azimuthal angles. Alternatively, the pitch can be changed along the azimuthal angle to try to provide the angle of attack at which the instantaneous power coefficient is as high as possible.

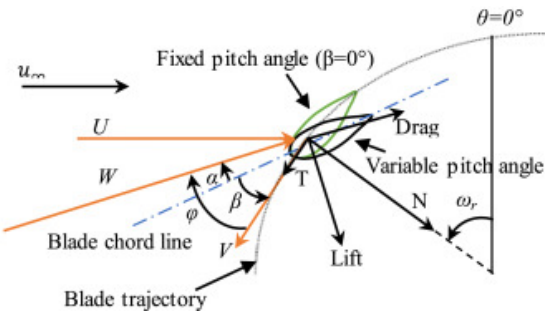

Figure 2.31: Variable pitch seen on the wind turbine blade, alongside the forces and velocities acting on the blade of a Darrieus turbine [65].

Types of variable pitch angle control systems

There are two basic types of variable pitch angle control systems: passive and active [65]. In a passive variable pitch system, the blade is free to pitch about its axis near the leading edge. The beginning torque and effectiveness of a VAWT can theoretically be significantly increased by this system. Nevertheless,

according to experimental research, the greatest power coefficient (C_p) value is only one-third of the expected value. To produce continuous changes in the blade pitch amplitude in an active control system, pitch control devices such as push-rods, cams or servomotors have been developed.

Pitch amplitude
To lower the angle of attack and hence improved rotor performance at low tip speed ratios (TSRs), a greater pitch amplitude is required [65]. However, with high TSRs, a big pitch amplitude may result in poor VAWT performance. In contrast, a modest pitch amplitude will result in poor performance at low TSRs even while it is sufficient to achieve good performance at high TSRs. This effect raises a crucial issue: How should the pitch amplitude be adjusted to enhance VAWT performance as the TSR shifts? In reality, the high frequency of the rotational speeds and the variations in the angle of attack makes it difficult to build actuators with quick response times to adjust the pitch angle for a compact H-type VAWT. The cost of such designs is also high for large turbines. A suitable aerodynamic model and a control system that can approximate the optimal pitch angle of an H-type VAWT during rotation are therefore required.

3

Analysis methods

In this chapter, the load analysis is discussed. Various loading conditions alongside the load cases are presented. In addition, a short look into fatigue analysis is made. One other topic is the critical failure modes. Moreover, aerodynamic models are summarized: from Single Stream Tube to CFD models. Moreover, two dynamic stall methods are discussed. The structural modeling methods are also briefly described. A small part of design optimization can also be read in this chapter. The chapter ends with addressing upscaling laws and considerations.

3.1. Load analysis

Structural loads are measured for various reasons. It can be for validation of the simulation model or design [68]. Another reason could be the optimization of components or certifications. Based on load conditions, the rotor design can be optimized. Besides, the certifications could be for a complete wind turbine, components, or a wind farm project.

3.1.1. Introduction to the load spectrum

Often, a load case table is made for wind turbines, which is a visualization of the load spectrum. These are all the loads seen by the wind turbine in its life [69]. The fundamental tenet is that the wind turbine must be capable of withstanding any load circumstances that may arise over the course of its lifespan. The International Electrotechnical Commission (IEC) standard provides a helpful table that lists each of these. Although some manufacturers opt for 25 or even 30 years, the technological life is typically assumed to be 20 years. Project developers aim to recoup their investment in maybe 10 years, but economic life may be a completely different story.

Load scenarios

The load scenarios are mentioned below. Production occurs, which ought to account for a sizable portion of overall life, as it is after all what the turbine is made for [69]. There will undoubtedly be starts, stops, and instances where the turbine is stalled or idled due to the wind speed being excessively high or low. Each normal load case must be combined with a single defect, often called a fault, such as a yaw or pitch system failure or a grid outage. This is because it is impossible to totally rule out the possibility of a fault. Finally, there may be sudden shutdowns in an emergency, such as when strong vibrations are noticed and the turbine needs to be swiftly shut down.

1. Production
2. Production + fault (grid outage, pitch, yaw error)
3. Start
4. Shutdown
5. Emergency shutdown
6. Parked / Idling
7. Parked / Idling + fault
8. Transport, maintenance, assembly, repair

Categories for load cases

Fatigue load cases (F) and ultimate load cases (U) are two categories for the load cases [69]. The ”highest loads ever” that the turbine encounters are known as ultimate load instances. These loads are typically assumed to be those that happen roughly every 50 years. Every instance that occurs regularly is classified as Normal (N). Some improbable fault combinations with a low chance of occurrence are labeled Abnormal

(A), which results in a lower safety factor. Various partial safety factors can be found, like the load factor (γ_F), material factor (γ_M), and the consequence-of-failure factor (γ_N).

To be sufficiently conservative, the loads are estimated as accurately as possible. However, each load is still multiplied by a load factor in the calculations. Furthermore, a consequence-of-failure factor can be added, since a failure of the tower is worse than a failure of a yaw gear.

3.1.2. Class definition

An overview of the wind turbine design classes can be found in Table 3.1. Three locations (or wind climates) are represented by the three primary classes: I stands for offshore, II for coastal, and III for inland [69]. The average wind speed at hub height is highest offshore and lowest onshore. The opposite happens for the turbulence intensity, where the highest values are found inland and lowest offshore. Offshore has the smoothest terrain. Class A represents inland and Class C offshore. The wind climate is also affected by other parameters. The wind speed distribution (Weibull distribution) is one of them. The Weibull shape parameter (k) measures the shape of the wind speed distribution, the greater the value of k, the narrower the spread of wind speeds [70]. Others are the turbulence frequency spectrum (a Kaimal spectrum), air density, wind shear exponent, and terrain slope.

Table 3.1: IEC wind turbine design classes [69] [71].

Reference site	Unit	Offshore	Coastal	Inland
Class	-	I	II	III
Average wind speed	m/s	10	8.5	7.5
50-years wind speed	m/s	50	42.5	37.5
50-year return gust wind velocity	m/s	70	59.5	52.5
Turbulence class	-	C	B	A
Wind speed distribution	-	Weibull k =2		
Turbulence spectrum	-	Kaimall		
Air density	kg/m^3	ρ = 1.225		
Wind shear exponent	-	0.2		

3.1.3. Loading conditions

A numerical approach for performing a combined aerodynamic and structural analysis of an H-configuration VAWT blade was developed by Castelli et al. [72]. Assessing the contributions of aerodynamic and inertial loads to the stresses and deformations of the blade during normal operation is the main focus of the research [5]. The paper analyses various skin thicknesses of the blade. For all the analyzed skin thicknesses, the inertial load seems to contribute more to the blade movement than the aerodynamic load. Aerodynamic loads are seen to be practically constant along the length of the blade when the blade is in the upwind position, with the exception of the aerodynamic loads at the tip.

Otherwise, it is shown that the aerodynamic load is dramatically shifting in both direction and magnitude while the blade is in the downwind position. The authors advise further study in order to determine the precise cause of this phenomenon. The authors also advise examining the aeroelastic impact on the turbine's performance. In particular, the relationship between the geometry of the airfoil's deformation and the turbine's performance.

3.1.4. Load cases for VAWT

Galinos et al. [73] investigated vertical axis wind turbine design load cases (DLC), also in comparison with horizontal axis wind turbines. The minimum design specifications for the structural integrity of VAWTs must be established in accordance with IEC and standardization. Based on HAWC2 simulations of a 5 MW 2-bladed Darrieus rotor, the IEC 61400-1 ed.3 standard's applicability for VAWTs was investigated. Numerous DLCs were examined and load levels with comparable nominal power HAWTs were compared. The researchers have chosen an IEC wind turbine class of II, which represents a coastal wind climate.

The wind turbine has minimum design requirements. Generally, IEC 61400-1 ed.3 standards set the minimum structural requirements for onshore wind turbines. The wind turbine states and external conditions make up the Design Load Cases (DLCs). Galinos et al. [73][74] have chosen for the following design situations:

1. Normal power production;
2. Emergency shut down;
3. Parked rotor.

Overview
Table 3.2 provides all investigated design load cases by Galinos et al. [73]. The definitions of the abbreviations mentioned in Table 3.2 for the wind conditions can be found in the nomenclature.

Table 3.2: Investigated design load cases by Galinos et al. [73].

Design situation	DLC according to IEC 61400-1 ed.3	Wind condition	Type of analysis
Power production	1.1 / 1.2	NTM	Ultimate & Fatigue
Power production	1.3	ETM	Ultimate
Power production	1.5	EWS	Ultimate
Power production	-	EOG	Ultimate
Power production	-	EDC	Ultimate
Emergency shut down	5.1	NTM	Ultimate
Parked-standing still and idling rotor	6.1 / 6.2 6.3 / 7.1	EWM 1 year and 50 years return period	Ultimate
Parked-idling rotor	6.4	NTM	Fatigue

Considerations
Galinos et al. [73][74] take in some considerations of the IEC 61400-1 ed.3 for VAWTs.

1. The hub height is taken where the wind reference values are applied. In their study, the rotor swept area center location is at nominal rotor speed.
2. The rotor diameter is used in equations for the definition of wind characteristics. The largest rotor diameter of the wind turbine is taken at a nominal speed.

Conclusion
In their conclusion, it can be read that the examined DLCs of IEC 61400-1, ed.3 are applicable for VAWTs, to a large degree [74][73]. However, some of them seem unnecessary and some of them need to be changed. When it comes to the loading of the VAWT structure, Extreme Wind Shear (EWS) and Extreme Wind Veer (EWV) transient wind conditions are not crucial.

Instead of being rated wind speed, the VAWT maximum loads always arise at the maximum operating wind speed for the investigated extreme transient events. These investigated extreme transient events are Extreme Direction Change (EDC), Extreme Operating Gust (EOG), EWS, and EWV. Extreme operating gust wind condition models have shown that when a frontal gust passes over a rotor, the emerging loads depend on the orientation of the rotor. Due to the rotor's 3D extension in space, the application of EOG should be researched in conjunction with various rotor orientations. In the VAWT models, high transient loads were not triggered by cases of abrupt changes in wind shear or dramatic direction changes.

3.1.5. Critical failure modes

Design standards are the result of years of research on HAWT design [5]. The requirements for blades specify that blade tip deflection, buckling, fatigue, and aeroelastic instability are the most dangerous failure types. The failure modes for VAWT blades and HAWT blades are distinct from one another. As HAWT blades have less tower clearance than VAWT blades, tip deflection will be more important.

Structural resonance
In literature, structural resonance is another frequent mode of failure for VAWTs [5]. When a blade is subjected to an external excitation that has a frequency matching one of the blade's natural frequencies, resonance results [52]. The eigenfrequencies should therefore be well known to prevent resonance. According to Lobitz [75], the safety and fatigue life of VAWT systems are significantly influenced by the dynamic response properties of the rotor. The calculation of critical rotor speeds (resonances) and the evaluation of forced vibration response amplitudes are the main issues. Experience has shown that under specific VAWT operating conditions, significant resonances can and do happen.

Berg [76] also covered this topic. He worked on the Sandia Test Bed design, previously discussed. Finding the resonance frequencies of the turbine systems is the main emphasis of the design process [5]. Resonance severely restricts the operating ranges of the rotor speed for each of the examined design options.

Definition
The 1P frequency of a wind turbine is defined as the frequency of the rotor revolution [46]. The 3P frequency of a turbine with three blades is three times larger than the 1P frequency, which is the frequency of a blade passing the tower. To avoid increased dynamic loads and resonance, it must be verified that the wind turbine does not operate such that the 1P and 3P frequencies for three-bladed turbines are within $\pm$ 10% from the first natural frequency of the turbine.

Sources for resonance
The main sources for resonance are listed below:

- Aerodynamic excitations at multiples of the rotor speed;
- Aerodynamic excitations due to the stochastic nature of the wind;
- Aerodynamic excitations on the downwind blade due to shed vortices at the rotor tower;
- Aeroelastic excitations due to flutter.

3.1.6. Fatigue analysis

The loads that the rotor faces during normal operation are critical for determining the rotor's fatigue life [5]. Because wind turbine structures must typically withstand at least 10^9 cycles over the course of a 30-year lifespan, this is critical, according to Sutherland et al. [44]. With each revolution, the radial aerodynamic loads on VAWT blades change signs, and as a result, they have a significant role in the fatigue life of a VAWT blade.

Normally, the goal is to ensure the lifetime of the wind turbine components when subjected to a lifetime load collective [68]. A lifetime load collective is the combination of all possible load variations during a lifetime. The starting point is the material fatigue strength (SN-curves, Wöhlercurves). Fatigue is a design factor for wind turbines. In normal operation, the blades undergo a reverse aerodynamic load with each revolution, wearing them down [5]. Centrifugal loads and gravity loads cause cyclic loads. Due to their propensity for fatigue, structural joints need special consideration when assessing fatigue. A counting method is needed since the wind turbine loads are time series with varying amplitudes. Often, Damage Equivalent Loads (DEL) are used to visualize the loads. DELs can be calculated by using a rainflow algorithm over signals. The algorithm extracts turning points and output loads for full or half cycles.

3.2. Aerodynamic models

VAWTs are mainly modeled using four different aerodynamic models [24]. Their accuracy and required resources vary. The four types of models are momentum models, the actuator cylinder model, the vortex model, and CFD models. Figure 3.1 shows an overview of these aerodynamic models with their accuracy and speed.

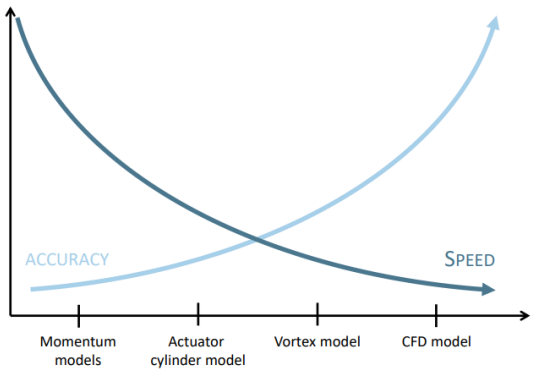

Figure 3.1: Overview of the modeling techniques as a function of their accuracy and speed [24].

3.2.1. Momentum models

The momentum theory, also known as the actuator disk theory, describes a mathematical model of an ideal actuator disk [24]. The rotor is modeled as a disc that is infinitely thin and has a uniform induced velocity throughout the cross-section of a stream tube.

Single stream tube model

Templin [77] suggested using this idea to calculate the rotor's induction with a single actuator disk with a similar thrust coefficient to replace a full vertical axis rotor in 1974 [24]. This model is referred to as the Single Stream Tube model.

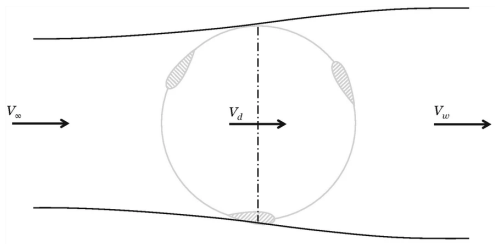

Figure 3.2: Visualization of single-stream tube model [78].

The momentum theory can be used to calculate the induction for the actuator disk set-up, as the entire rotor would be subjected to this induction. With the aid of momentum continuity, the induction factor in the zone can be calculated, as in Equation 3.1. This factor depends on the solidity (σ), the tip speed ratio (λ), and the azimuth angle (θ) [6].

$$a = \frac{\sigma}{\pi}\lambda \sin\theta \tag{3.1}$$

The blade is assumed to receive a lower, undisturbed flow velocity throughout the downwind path because the SST is a straightforward tool that does not account for the interaction between the blade and the wake [6]. Due to the earlier disruption of the flow, this is only partially true. The accuracy of SST is being greatly reduced as a result of these assumptions and simplifications.

Double stream tube model

The double stream tube model (DST) has been proposed, as the single stream tube model is rather constrained [24]. The induction downwind is expected to be higher than the induction upwind. The double stream tube employs two actuator disks in series, one for the rotor's upwind half and the other for its downwind half. Both actuator disks have equal thrust coefficients. It is assumed that the input of the second stream tube is equal to the outlet velocity of the first stream tube. For this reason, the model can determine two different induction for the upwind and downwind halves of the rotor.

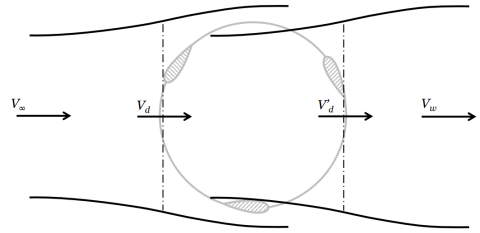

Figure 3.3: Visualization of the double stream tube model [24].

Multiple stream tube model

However, it is expected that the induction would change in the cross-flow direction in addition to the fact that it should vary in the upwind and downwind halves of the rotor [24]. Therefore, Wilson, Lissaman, and subsequently Stickland suggested using a succession of contiguous stream tubes rather than enclosing the entire rotor in a single tube. The multiple stream tube model is invented. The rotor parts are replaced by a single equivalent actuator disk with loading that corresponds to whatever load is present in each individual stream tube. Figure 3.4 shows a visualization of the multiple stream tube model.

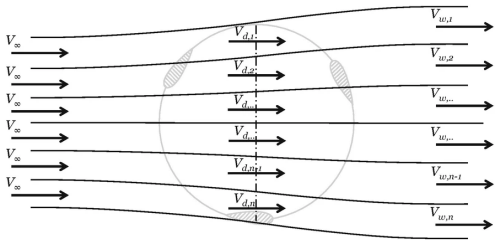

Figure 3.4: Visualization of the multiple stream tube model [78].

Double multiple stream tube (DMST)
The combination between the multiple stream tube model and the double stream tube model follows quickly and the double multiple stream tube (DMST) model is developed [24]. The model was proposed by Paraschivouiu [79]. The DMST model uses many stream tubes, similar to how many are used in the Blade Element Model (BEM) [6]. The upwind and downwind halves of the rotor are replaced by two different actuator disks that have an equivalent loading. These actuator disks are arranged in a sequence of neighboring, aerodynamically independent stream tubes. This allows for the determination of a varied induction for each stream tube as well as for the upwind and downwind halves independently.

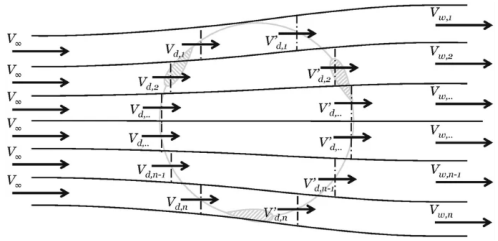

Figure 3.5: Visualization of the Double Multiple Stream Tube model [78].

Various assumptions can be displayed from the Double Multiple-Streamtube Model (DMST) [24]:

- The atmospheric pressure is in the center of the turbine, as the wake of the upwind half develops completely before it reaches the downwind half;
- The flow is considered to be undisturbed, regardless of its location. This neglects the fact that a wake was shed earlier;
- Straight stream tubes are used in Paraschivoui's initial DMST model, while flow expansion is included by Read and Sharpe;
- The stream tubes completely operate independently;
- The induction of the downwind actuator disk on the upwind actuator disk is not taken into account.

Due to its ease of use and quick response time, DMST was seen as a significant design tool, similar to the BEM [6]. Only high-quality models were able to demonstrate the model's error [80]. The original DMST made the assumption that the flow only encounters induction factors parallel to the flow. However, the rotating motion also causes induction factors perpendicular to the flow. The lateral induction factor was suggested by Prof. Carlos Simão Ferreira [80] as a way to enhance the DMST. By approaching the induction zone as a circulation issue, this can be accomplished. A tiny vortex is created in the circulation problem throughout the course, but the main vortex contribution occurs at the change from upwind to downwind. Improvement can be found in this modified model.

3.2.2. Actuator Cylinder Model (ACM)

H.A. Madsen first put forth the Actuator Cylinder Model (ACM) in 1982 [8]. The ACM is a 2D model, but 3D equations can be derived in a similar way [24]. The model is based on the conservation of mass and momentum. This approach incorporates the swept area of the turbine in the direction perpendicular to the disk. It extends the actuator disk concept (the momentum theory) and the model is also solved iteratively. However, the ACM uses a cylinder or circle instead of a disc, which is more equivalent to the swept area [6][24]. The average blade forces that will occur during one revolution will be applied as a reaction to the actuation surface. An infinite number of blades is thus assumed. In due course, the force field and velocity field will be steady in time. The Actuator Cylinder Model is presented in Figure 3.6.

Principle
The Actuator Cylinder model should be solved iteratively [24]. First, control points are initially placed at the midpoint of each of the N uniformly spaced sections of the rotor [6]. The induced velocity is initially set to zero. The blade element theory can then be used to calculate the angle of attack, and the forces based on the local velocity. Furthermore, the influence coefficients, which quantify the influence of loading on the velocity of each control point, can be calculated. As a result, the induced velocity can be updated at each azimuthal location and the procedure can be repeated until a convergent solution is discovered. The flow velocity is obtained using 2D, steady, and incompressible Euler equations and the equation of continuity are used for the Actuator Cylinder Model.

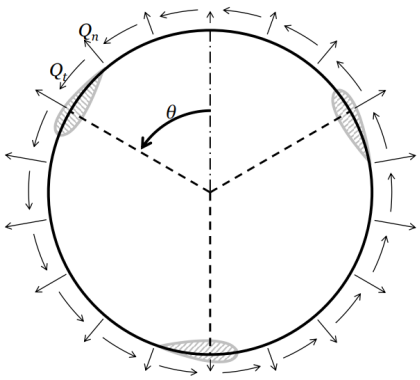

Figure 3.6: The Actuator Cylinder Model, representing a VAWT [24]. The forces are perpendicular and normal to the circle.

In the Actuator Cylinder Model, two parameters are introduced. These are the non-dimensional time-averaged normal and tangential loading [24]. The loading is time-averaged in one revolution and non-dimensionalized. The non-dimensional loading components are displayed with Q_n and Q_t for the normal and tangential direction respectively, shown in Equation 3.2.

$$Q_n(\theta) = \frac{BF_n(\theta)}{2\pi R\rho V_\infty^2} \qquad Q_t(\theta) = -\frac{BF_t(\theta)}{2\pi R\rho V_\infty^2} \tag{3.2}$$

Assumptions
The ACM is based on various assumptions [24]:

- The elements and stream tubes are no longer dependent, instead, the impact of one element or stream tube on the other is taken into consideration;
- The induction of the downwind part on the upwind part is taken into account;
- Stacking 2D independent slices can be used to simulate a 3D rotor;
- Steady solution.

Despite being a somewhat complex model, the ACM nonetheless generates quick results. However, it should be noted that the ACM makes simplifications, like no wake-blade interaction [6].

HAWC2
The 2D Actuator Cylinder model is used for the aerodynamic model in HAWC2 [81]. The three-dimensional VAWT is condensed into a number of 2D cylinders, which are stacked vertically. Now, it is possible to determine the steady-state solution very quickly. The implementation is a more computationally efficient approach than other models. With the dynamic inflow model, known from dynamic BEM formulations of HAWT simulations, the model is expanded from a quasi-steady approach. The aerodynamic model can still be improved in terms of identifying the proper time constants.

3.2.3. Vortex models
Vortex models are another method that can be used to calculate the induced velocity at the rotor and at any other point in the velocity field [24]. To compute the induced velocity and hence the relative velocity at the blades, vortex models examine the vorticity field. Either the lifting-line theory or the principle of a lifting

surface can be used to compute the loads on the blade. Generally, vortex models are unstable codes due to solving in time. Figure 3.7 demonstrates the growth of shed vortices of a vortex element.

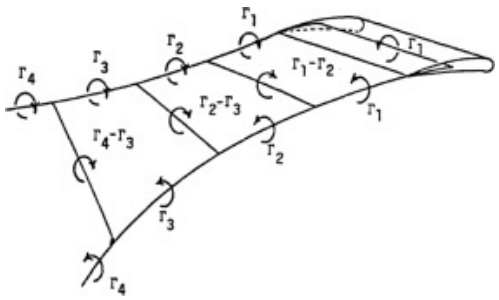

Figure 3.7: Diagram of a vortex element showing the development of shed vortices [82].

Theorems
The vortex models rely on two main principles [6][24]:

- Helmholtz' vortex theorem: the circulation is constant along vortex line and cannot end;
- Kelvin's circulation theorem: the change in circulation over time has to equal zero, as opposed to momentum and mass conservation.

The first one is Helmholtz's vortex theorem. It says that circulation should be constant along a vortex line and cannot end in the fluid. It must form a closed path. The second principle is called Kelvin's circulation theorem. This theorem states that the time rate of change of circulation in a closed loop must be zero (Equation 3.3).

$$\frac{D\Gamma}{Dt} = 0 \tag{3.3}$$

Lift
According to Kutta-Joukowski, the product of velocity (U), density (ρ), and circulation (Γ) can be used to describe an airfoil lift (L'). Equation 3.4 shows this expression. A change in the angle of attack typically results in a different lift force, which necessitates a change in the circulation. Another circulation needs to be discharged in the form of a wake in order to make up for this change. This circulation will move downwind, where its impact will diminish with increasing distance.

$$L' = \rho U \Gamma \tag{3.4}$$

Types of vortex models
This approach captures the vortex interactions that occur when the VAWT works in its own wake, making it more realistic and accurate than the DMST model. Furthermore, there are two types of wake simulations for these models, free-wake and fixed-wake. The vortex method can often be divided into two groups based on whether they are discretized as a single line or as a mesh made up of numerous panels. These are the lifting line and the vortex panel method.

3.2.4. CFD models

Lastly, aerodynamics can be looked into with the use of Computational Fluid Dynamics (CFD). The solver inserts a finite number of permeable, mass-conserving control volumes into the domain [6]. Before adding control volumes to the domain, it is necessary to establish its bounds by either knowing the values at the edge of the domain (Dirichlet boundary conditions) or its flux (Neumann boundary conditions). For VAWTs, the blades could be included as geometrical surfaces or represented by including volume forces into the flow field [24].

Principle
CFD tries to solve the Navier-Stokes (N-S) equations and the continuity equation for every control volume and time step. The Navier-Stokes equations to calculate the pressure and velocity field [24]. The continuity equation is simplified by the assumption that the flow is in-compressible as the Mach number is below 0.3 [6]. Here, in these equations, $\vec{v}$ stands for the flow velocity, ρ for the fluid density (mostly air), p for

the pressure, $\vec{T}$ for the stress tensor on the fluid and $\vec{f}$ for the external forces. The blades are either represented by volume forces or as geometrical surfaces.

$$\rho\left(\frac{\delta\vec{v}}{t}+\vec{v}\cdot\nabla\right)=-\nabla p+\nabla\cdot\vec{T}+\vec{f} \tag{3.5}$$

$$\nabla\cdot\vec{v}=0 \tag{3.6}$$

Accuracy, grid considerations, and turbulence modeling
CFD models are the most accurate for VAWTs. However, the domain of such problems needs to have a fine grid in order to be sufficient [6]. This will increase the computational cost. CFD models do not have the errors brought on by various assumptions used in other simulation techniques. CFD models are effective for extremely high and low solidity values and for all tip speed ratios [8]. Through the use of discretization techniques, a mesh covering the rotor and its surrounds is constructed, which is then used to solve the Navier-Stokes equations. Turbulent air is a common operating environment for wind turbines. As a result, turbulence modeling must be used while the rotor is being simulated. CFD models can be divided into three main types: DNS, RANS, and LES [6].

DNS
The Navier-Stokes equation is directly solved using the Direct Numerical Solution (DNS) method. Within a single control volume, DNS is able to resolve the domain down to the tiniest of details, where the change in momentum equals zero. The great accuracy and lack of any simplifications make DNS appear to be an expensive brute-force solver. It will be more prudent to use a different method to solve the CFD model if the domain is vast.

RANS
The Navier Stokes is modified slightly by the Reynolds Averaged Navier-Stokes (RANS) approach. The problem is examined by RANS as a superposition problem. It is divided into a time-averaged value and its fluctuation. Fewer iterations will be necessary, lowering the cost of calculation. RANS has the limitation that it cannot simulate an unstable aerodynamic, which is required for dynamic stall. Although URANS is attempting to add unstable terms, its validation is not yet complete.

LES
Large Eddy Simulation (LES) can only estimate the conservation of momentum up to a specific amount of turbulence. Values that are smaller than this size will be ignored or calculated using a different turbulence model. Smaller turbulence can be ignored to reduce processing costs and provide self-defined fidelity.

3.2.5. Comparison between models
Based on the discretization being decreased to a single tube, the SST is determined to be the simplest model [6]. SST and DMST rank last in accuracy when compared to other models, while SST is slightly lower than DMST. DMST does not consider the unsteady flow effects and the influence of the downwind part on the blades at the upwind part [8]. The DNS edition of CFD holds the top spot since it can resolve the domain even in the presence of the slightest disturbance. SST, DMST, and ACM all share the top spot in terms of computational time. Furthermore, they are computationally less expensive than CFD models. Compared to the DMST model, the vortex models require more computational work but have a greater level of fidelity [8].

3.3. Dynamic stall methods
Large dynamic loads that a wind turbine experiences during its life cycle can be predicted in large part thanks to dynamic stall [83]. An efficient way to reduce the cost of energy is to avoid over-designing a wind turbine by accurately predicting dynamic loads. HAWC2 offers three different dynamic stall models that can be used in the software. These are the (1) Stig Øye method, (2) the MHH Beddoes method (Beddoes-Leishman), and (3) the Gaunaa-Andersen method with Deformable Trailing Edge Flap's [1]. The last method is to support trailing edge flap devices.

3.3.1. Stig Øye method
Stig Øye created a simple, dynamic stall model in the 1990s [84]. In order to replicate the time lag delay of the lift reaction to changes in the angle of attack, it uses a straightforward first-order Ordinary Differential

Equation (ODE). Two separate lift curves, the fully attached flow curve and a fully detached curve, are used in tandem to achieve this. The interpolation factor (f) is a variable that is used to calculate the distance between these two curves. Using the ODE, this interpolation factor is given a time lag and represents the relative importance of these two lift curves.

The Stig Øye method is a straightforward model that simply requires as inputs the angle of attack (α), the inflow velocity (U), and the interpolation factor (f) from the previous time step. The static drag and moment coefficients are not changed. The dynamic lift coefficient is the only output. Additionally, it merely displays the steady lift value, whether the flow is entirely linked or separated. The Stig Øye method reproduces the stall dynamics on the lift coefficients but not on the drag or moment coefficients or any dynamics in the attached flow.

3.3.2. Beddoes-Leishman method

Beddoes and Leishman created the Beddoes-Leishman (B-L) method initially for use in helicopter applications [83]. The model was modified by Gupta and Leishman to make it appropriate for wind turbine applications.

Modifications

By ignoring the impacts of leading edge separation, caused by the use of relatively thick airfoils on wind turbines, and compressibility, Hansen et al. [85] provided a simplified version of the model. The model has a decrease in the number of tuning factors. However, due to their increased flexibility, the blades now have to withstand higher pitch rates and larger deformations as a result of the development of larger wind turbines with active pitch control (to dampen tower fore-aft vibrations). On thick wind turbine airfoils, leading-edge separation has therefore become likely and needs to be taken into account in modeling [83].

Principle

The B-L model has undergone the most testing of any dynamic stall model in the literature. The primary goal of the B-L model is to recreate the physical processes behind the dynamic stall phenomenon. Mathematically delaying the formation of flow separation, increasing the lift coefficient by a convecting leading edge vortex, and delaying the lift coefficient of connected flow are used to model these flow dynamics.

Modules

The total unstable lift is calculated using a linear combination of the results from the B-L model's four distinct simulations of the controlling physical causes of dynamic stall [83][86].

1. An attached flow model for the unsteady (linear) air loads, based on Duhamel superposition;
2. Separated flow model for the nonlinear air loads;
3. Dynamic stall onset model;
4. Dynamic stall model for the vortex-induced air loads (Vortex Lift Module).

3.4. Structural modeling

As wind turbines grew in size, the structural aspect started to become important [6]. Small turbines were first built with rigid and stiff construction. VAWTs have a risk of flutter, based on the orientation of the blades and the direction of their rotation. When the blades are bent outward, centrifugal forces and relative velocity rise, changing the loads on the structure. Structural dynamics may be employed as a passive control mechanism, depending on the design. Similar to aerodynamics, many methods can be used to mimic the structure.

Computational Structural Dynamics (CSD)

By discretizing a structure into a number of parts, each with distinct physical properties, and specifying the boundary conditions, computational structural dynamics (CSD) can be used to analyze the behavior of a structure [6]. CSD is the most accurate solver when used in combination with Finite Element Method (FEM), but also computationally expensive. CSD is mostly used to analyze static loading instead of an aeroelastic analysis.

Multi-Body Systems (MBS)

Multi-Body Systems (MBS) can be used to analyze the behavior of multiple bodies connected with hinges or joints [6]. The degree of freedom depends on the connection between bodies, while the bodies can either be stiff or flexible. The equation of motion can be solved afterward. If the bodies are flexible, the deformation must be taken into account. When the assumption is made that a body is rigid, it cannot deform. This leads to reducing the computationally cost and accuracy.

Modal analysis
The modal analysis involves analyzing the eigenmodes of a structure while using FEM [6]. A higher order of eigenvalues is required to obtain an accurate solution. Any deflection of the blade can be characterized as a sum of modes, once the eigenmodes have been identified.

Beam method
A structure is modeled in a beam analysis as a connection of beams [6]. Equations, including shear force, slope, moment, and displacement define the elastic deformation behavior. Calculations can be made simpler and costly integration can be avoided by using the Conjugate Beam Theorem:

1. The slope of a beam at any cross-section is determined by the shear force of the conjugate beam;
2. The deflection of the beam at each location is determined by the bending moment of the conjugate beam.

3.5. Design optimization

Every wind turbine design process must start with a load study. Precise load estimates are the cornerstone of every effective design optimization [87]. As constructing prototypes of large VAWTs is very costly and ineffective, this is not desirable for finding an optimal design [6]. Furthermore, different power outputs for the design and therefore its size can be optioned. To find a successful design, the design process calls for several repetitive actions [5]. Iteration is necessary in order to analyze various designs. A design analysis frequently involves several disciplines, including aerodynamics, structural mechanics, and wind turbine control. These disciplines interact, necessitating iteration between them to produce a coherent design analysis. These repeated tasks require a lot of labor because each specialty has a unique tool that is used by a specialist. This multidisciplinary design analysis automation makes it possible to perform numerical optimization. The development of holistic methodologies for the design of the machines has included load analysis into iterative optimization loops [87]. In the past, it was primarily a verification phase. Deterministic load estimating methodologies have, however, often been used as a result of the desire to reduce the complexity and processing costs of the load assessment. To identify the best-fitting rotor geometry that has a low mass while yet converting the most energy feasible, an optimization tool is of utmost importance. There is no rotor optimizer publicly available focusing on a VAWT [6]. Optimization is described as ”The determination of values for design variables which minimize (maximize) the objective, while satisfying all constraints.” by Papalambros [88].

3.6. Upscaling laws

Not much prior research has been done on creating scaling rules for VAWTs. However, there has been a lot of work done on creating scaling laws for HAWTs [5]. In this section, both upscaling laws for HAWTs and VAWTs are discussed.

3.6.1. Upscaling of HAWTs

Analytical relationships between significant parameters that depend on the rotor diameter of the turbine are used to establish linear scaling laws [5]. All geometrical parameters are assumed to scale linearly in the analytical relations. The significant parameters are utilized to calculate the turbine’s energy cost. The ideal turbine size is determined by the turbine’s size for the lowest energy cost. Three distinct assumptions are the base for linear upscaling [89]:

1. Airfoil types, turbine material, drive train, support structure concepts, and the number of blades are the same;
2. The tip speed remains constant;
3. Other geometrical parameters (except gearbox, generator, and power electronics) vary linearly with the rotor diameter.

However, linear scaling laws cannot accurately capture the entire impact of scaling, as they do not allow for a trade-off between the rise in load levels on the rotor and electricity output [89]. None of these linear scaling laws are adequate for examining the technical viability of a turbine. This necessitates the use of a sophisticated model, which could be viewed as the fundamental disadvantage of upscaling with linear scaling laws. However, the linear scaling laws can be particularly helpful in order to comprehend the scaling phenomenon early on in the construction of a wind turbine.

Analyzing the trends of existing turbines and their data is an alternative strategy [89][5]. However, extrapolation is needed to evaluate reasonably large turbine sizes, which have not yet been produced. Extrapolation is prone to errors. Over the years, various pieces of research have been conducted. The

upscaling laws, based on existing data, can be divided into two parts: as a function of the rotor diameter and the mass of different components.

Blade
All of the geometrical parameters for the blade are scaled linearly. When the blade is scaled up, the load levels can raise to a level where they have a negative impact. Furthermore, it can also have the effect of increasing the amount of captured energy. Jamieson [90] formulated linear scaling laws, based on the extreme loads at the blade and as a function of the rotor diameter. The edgewise bending moment scales with size more quickly than the flapwise moment.

Table 3.3: Geometric linear scaling laws for wind turbine blade [89]. R means linear dependency, I means size independency.

Symbol	Description	Size dependency
L	Blade length	R
ω_{rot}	Rotor rotational speed	R^{-1}
$\omega_{rot} \cdot L$	Tip speed	I
$c_{bld}(x)$	Blade chord distribution	R
$t_{bld}(x)$	Blade thickness distribution	R
$\theta_{bld}(x)$	Blade twist distribution	I
M_{flp}	Flapwise moment	R^3
M_{edg}	Edgewise moment	R^3
P_{rot}	Rotor power	R^2
T_{rot}	Rotor torque	R^3
$A_{bld}(x)$	Blade sectional area	R^2
$I_{are}(x)$	Area moment of inertia	R^4
$I_{mas}(x)$	Mass moment of inertia	R^5
M_{bld}	Blade mass	R^3

One of the most crucial factors in the estimation of the dynamic load on the blade and wind turbine is the mass of the blade and its scaling behavior [89]. Mass-diameter trends can be found by a power law fit data of 52 data points from 7 manufacturers. A lower exponent is found than indicated by the linear scaling law. This is mostly due to improved manufacturing technologies, better airfoils, and more aerodynamic designs that have been developed during the past ten years in an effort to reduce bulk and related expenses. Moreover, different aerodynamic design can be chosen based on the operational conditions. With larger wind turbines, the Reynolds number increases and so does the C_l/C_d ratio. Smaller wind turbines need therefore thicker airfoils to perform well.

Tower
Scaling research is conducted using a tubular tower configuration. Table 3.4 below presents the linear scaling rules as a result. Upscaling has less detrimental effects on the tower in an offshore setting than it does onshore. This is because offshore wind generators experience a steeper wind shear profile.

Table 3.4: Linear scaling laws for the tower [89].

Symbol	Description	Size dependency
L_{tow}	Tower length	R
$t_{tow}(x)$	Tower thickness distribution	R
$A_{tow}(x)$	Tower sectional area	R^2
$I_{are}(x)$	Area moment of inertia	R^4
$I_{mas}(x)$	Mass moment of inertia	R^5
$M_{for-aft}$	Fore-aft bending moment	R^3
$M_{sid-sid}$	Side-to-side bending moment	R^3
M_{trs}	Torsional moment	R^3

The studied towers in Jamieson's work [90] are of tubular type, made of steel. The results are only given for the extreme bending moments. The results are not matching with the linear scaling law. The fore-aft bending moment has the lowest exponent, followed by torsional moments.

3.6.2. Upscaling of VAWTs

Gaspar Gohin [91] carried out his Master's thesis on upscaling, analysis, and design of a floating vertical axis wind turbine (FVAWT).

INNWIND project

Initially, Gohin [91] discussed the INNWIND project, in which the 5 MW FVAWT DeepWind concept has been scaled up to 10 MW. The swept area of the Darrieus rotor was doubled in order to double the rated power, using the same physical theory as for HAWT upscaling: geometrical upscaling at a constant tip speed ratio and rated wind speed. The upscaling was made using dimensional analysis. An illustration of the 5 MW and 10 MW rotors in the vertical position, with increased height and radius, is shown in Figure 3.8.

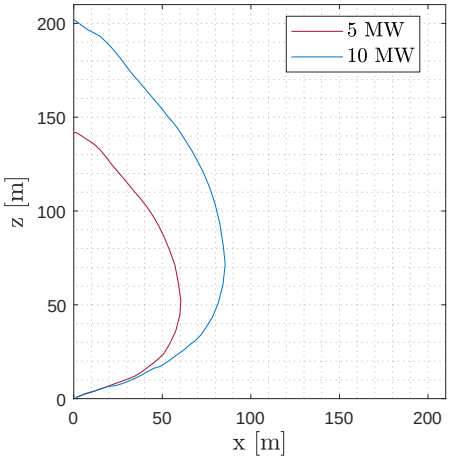

Figure 3.8: Rotor size comparison from DeepWind (5 MW) to INNWIND (10 MW) [91].

As the upscaling increased the bulk of the rotor, the spar had to be redesigned. His thesis is aimed more at spar optimization and improvement of the numerical analysis tool SIMO. One of the available tools used in SIMO is the Double Multiple Streamtube (DMS) for aerodynamics and rigid bodies, and linear stiffnesses for the structural part.

Considerations

As upscaling approaches are typically based on geometric and aerodynamic similarity, the tip speed ratio is kept constant, even if the rotor's size is expanded [91]. The following theoretical scaling principles can be applied to the weight and power, with κ the geometrical scaling factor.

$$M \sim \kappa^3 \tag{3.7}$$

$$P \sim \kappa^2 \tag{3.8}$$

$$L \sim \kappa \tag{3.9}$$

The geometrical scaling factor should be $\kappa = \sqrt{2}$, in order to double the aerodynamic power from 5 to 10 MW. When the aerodynamic power goes from 5 to 20 MW, this geometrical scaling factor will be $\kappa = \sqrt{4}$. Each physical variable has a specific unit, a combination of meters, kilograms, and seconds. Meters scale with κ, kilograms with κ^3 and seconds with κ.

Table 3.5: Upscaling considerations for VAWTs [91].

Design	Parameter	Unit	Scaling factor
Geometry	Length	m	κ
	Mass	kg	κ^3
	Inertia	kg.m^2	κ^5
Aerodynamics	Tip speed ratio	-	1
	Wind speed	m$/$s	1
	Rotor speed	rad$/$s	κ^{-1}
	Torque	kg.m^2.s^{-2}	κ^3
	Power	kg.m^2.s^{-3}	κ^2

It should be noted that these considerations are based on scaling all parameters linearly. However, this does not mean that the optimal design comes out of it. Other scaling options can be considered instead, such as the scaling of the aspect ratio.

4

Methodology

This chapter provides an overview of the methodology of this project. The pre-processing, processing, and post-processing stages of the process are all covered in detail. The overview describes the setup in general. Hereafter, the pre-processing phase is discussed. The reference model shall be recreated in HAWC2 [1][2] using cross-sectional parameters from BECAS [3][4]. During the processing stage, the model is verified and several design drivers are recognized and assessed. The last section discusses how the post-processing phase shall be. The simulation data from HAWC2 are analyzed and based on this, conclusions and discussions can be made.

4.1. Overview

The general methodology of the project involves two main steps: verification and parametric analysis. Figure 4.1 shows the flowchart for the methodology of this project. The first step lies with the pre-processing: the reference model is re-made in HAWC2, while the cross-sectional parameters for the blade and strut are calculated with BECAS. While the reference model is being verified with HAWC2, various design drivers can already be distinguished. The verification guarantees the accuracy and reliability of the results if these are consistent. Afterward, the model is adjusted to look into different design drivers of the vertical axis wind turbine design. Lastly, the impacts of these design drivers on the performance and aeroelastic stability of the turbine are post-processed.

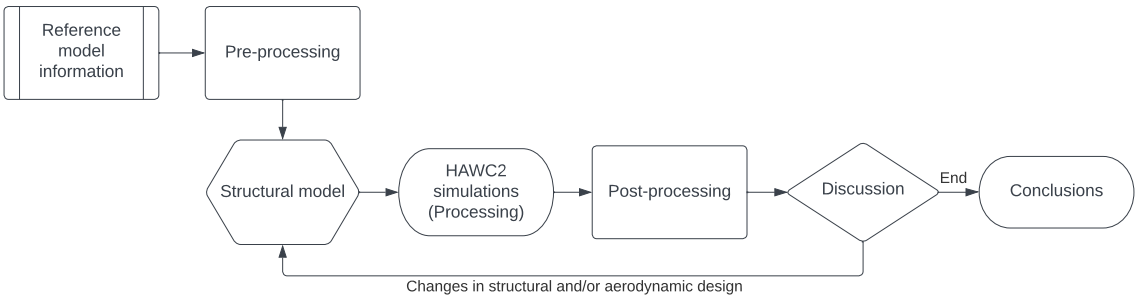

Figure 4.1: Flowchart of the total methodology of this project.

4.2. Pre-processing

In general, the simulations will be done in HAWC2, for which a specific structural input file is needed. This input file can be automated by the cross-section analysis software BECAS [92], which needs the pre-processor Airfoil2BECAS [92]. Airfoil2BECAS makes a mesh that BECAS can read in and process further. Airfoil2BECAS is in need of different inputs, such as an airfoil profile file with the right coordinate system and various material properties. Not only a blade profile can be processed, but other cross-sections can also be utilized. The scheme of the pre-processing can be seen in Figure 4.2.

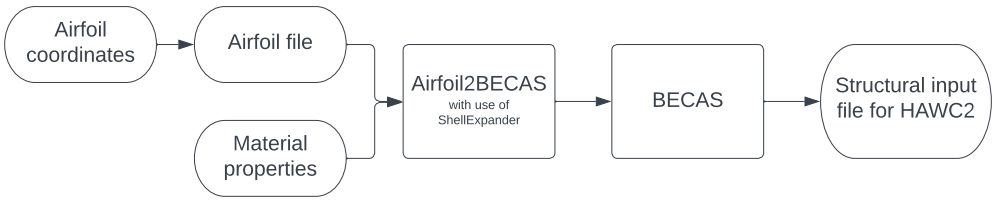

Figure 4.2: Scheme of the pre-process before the first aeroelastic simulations and the optimization.

4.2.1. Structural properties

The first step lies with Airfoil2BECAS. Airfoil2BECAS is a Python code that can generate a 2D mesh of the cross-section and corresponding material and orientation assignments [92]. Airfoil2BECAS makes use of ShellExpander to generate the mesh. Airfoil2BECAS has the main function to generate an input file for the software BECAS, which can do analyses of wind turbine blade cross-sections. It provides the structural properties for the HAWC2 model.

Input

As Figure 4.2 shows, Airfoil2BECAS needs various input information as well. The airfoil coordinates should be given in a file, while the shear webs are specified in the Python code. Every coordinate is a node. Moreover, specific material data is required. Table 4.1 shows the input matrix for the material data, which are material properties for the different material plies [92]. Lastly, Airfoil2BECAS needs information on the lay-up of the laminated in each structural member of the blade or strut.

Table 4.1: Material properties needed to deliver to Airfoil2BECAS [52][92].

Design variable	Symbol	Definition
Material	E_1, E_2, E_3	Young's modulus in three principle directions
	$\nu_{12}, \nu_{13}, \nu_{23}$	Poisson coefficient in three principle directions
	G_{12}, G_{13}, G_{23}	Shear modulus in three principle directions
	ρ	Density

Concept

The shape of the airfoil is defined by nodes and is read from the airfoil coordinate file [92]. The circumferential element size of the final 2D mesh is determined by the spacing between the nodes. With the nodes, the shear webs can be defined while also other regions between nodes (with "keypoints"). For each region and shear web, the layup of its materials should be given (chosen material, thickness, and orientation). An example of the Airfoil2BECAS concept is given in Figure 4.3.

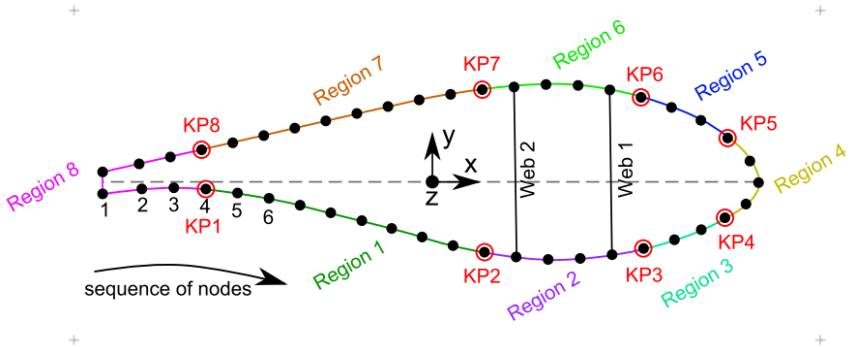

Figure 4.3: Example of the Airfoil2BECAS concept, where the nodes define the airfoil. When there are n nodes defined as key points, there will be n regions [92].

Discontinuities in thickness typically arise where two regions meet [92]. By creating a continuous (node-based) thickness distribution, Airfoil2BECAS eliminates these discontinuities to make mesh production easier. To do this, the thickness at the boundary between the two regions is designated as the lesser of the

two thicknesses. By specifying ”dominant regions”, this default behavior can be modified. The dominant regions control the thickness at region boundaries. In wind turbines, the spar caps carry most of the load. Therefore, it would be a good reason to choose these regions to be dominant. If the thickness here would slightly change, the cross-section stiffness could have a noticeable impact on the stiffness properties.

Limitations
The airfoil can be defined in any number of regions, but the shear webs cannot be divided into multiple regions [92]. The shear web can only be defined as one region for the layup of plies. Furthermore, the shell thickness can be discretized in any number of elements, but the minimum value is the highest number of layers of material layers anywhere in the cross-section.

4.2.2. Cross section analysis

BECAS (short for BEam Cross section Analysis Software) shall be used to generate a structural input file for HAWC2, in which the total VAWT can be simulated. BECAS can convert the precise layup models to structural properties for the HAWC2 model [52]. BECAS was specially created for cross-section analysis [4]. The effects of inhomogeneous material distribution and anisotropy can be accurately predicted by BECAS, which can handle a wide variety of arbitrary section geometries. The cross-section stiffness qualities can be determined by BECAS while accounting for all the geometrical and material-induced couplings based on a definition of the cross-section geometry and material distribution.

Workflow
The workflow of BECAS for structural blade analysis and design is illustrated in Figure 4.4 [3]. In the first place, BECAS can be used as a pre-processor, like in this thesis project. It generates the beam finite elements to represent the blade in the aeroelastic analysis code (HAWC2). A series of pre-defined cross-sections along the blade are analyzed based on a finite element mesh of the cross-section. BECAS can also be used after aeroelastic analyses in HAWC2.

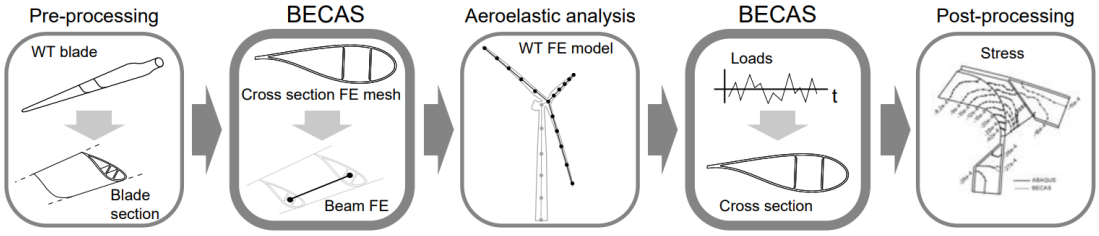

Figure 4.4: The workflow of BECAS when used for the aeroelastic analysis of wind turbine blades [3].

Structural input files for HAWC2
As mentioned before, BECAS generates the structural input file for HAWC2. BECAS can generate two different structural input files based on the fact that the material is an-isotropic or not. When the material is not an-isotropic, BECAS makes a structural file for HAWC2 based on the original beam model. The structural parameters in this file are shortly presented below. A more detailed definition list is given in Appendix A.

- The distance;
- The mass per unit length;
- The mass center;
- The radius of gyration related to elastic center;
- The shear center;
- The modulus of elasticity and the shear modulus of elasticity;
- The area moment of inertia;
- The torsional stiffness constant;
- The shear factors;
- The cross-sectional area;
- The structural pitch;
- The center of elasticity.

When the material is an-isotropic, BECAS generates a structural file for HAWC2 based on the fully populated stiffness matrix. The structural file overlaps for some bit with the structural parameters written down above, but it also contains the cross-sectional stiffness matrix. The stiffness matrix is given at the elastic center rotated along the principal bending axes [1].

4.3. Processing: aeroelastic analysis

The next step is processing, which is the aeroelastic modeling of the wind turbine model for different settings. During this phase, HAWC2 acts as the main simulation tool for analyzing the performance and behavior of the wind turbine model. To ensure its accuracy, the reference model is simulated under similar operating conditions. Afterward, the investigation of numerous design drivers is examined. The advanced capabilities of HAWC2 enable detailed analysis of the turbine's response to various configurations and conditions. This makes it easier to find the best design options in the post-processing phase when the data is analyzed. It should be noted that the three phases (pre-processing, processing, and post-processing) go in a loop. When the first results are found and analyzed, the changes are implemented in the structural model and new simulations are run.

4.3.1. Parametric analysis and verification

The goal of the processing phase is to find the design drivers of the VAWT design and simulate various cases to compare the results in the post-processing phase. This process of examining the design drivers can be referred to as the "parametric analysis". Changes in the design parameters are investigated in relation to the performance and behavior of a vertical-axis wind turbine. At the same, as the model in this project is based on a reference model, the results shall be compared to the report of Schelbergen [5] to verify the model.

4.3.2. HAWC2

The chosen aeroelastic modeling tool is the software named HAWC2. HAWC2 stands for Horizontal Axis Wind turbine Code 2nd generation [52]. The aeroelastic code was created by Risø - Danish Technical University. HAWC2 simulates the wind turbine response in the time domain for onshore, offshore, and floating wind turbines. HAWC2 is based on the Actuator Cylinder (AC) flow theory for VAWTs and is validated [7][52].

Input files

HAWC2 runs a htc-file which contains the model and all their input files for the structure. Figure 4.5 shows an overview of the structural input files. The main input file defines the structure globally: the (number of) bodies, the location of nodes, and the orientation of the coordinate systems. The first input file is the beam cross-sectional data, which contains the cross-sectional properties for the Timoshenko beams [93]. These cross-sectional properties have previously been discussed in Section 4.2.2. Furthermore, the aerodynamic layout and aerodynamic profile coefficients are required. In the aerodynamic layout file, the aerodynamic layout of the blade is defined as a function of the radial position. It contains the chord length (c), the thickness ratio between height and chord (t/c) in %, and the profile coefficient set number. Details about the profile coefficient should also be provided, which is the angle of attack (α) over a range of 360 degrees, the lift coefficient (C_l), the drag coefficient (C_d), and the moment coefficient (C_m),

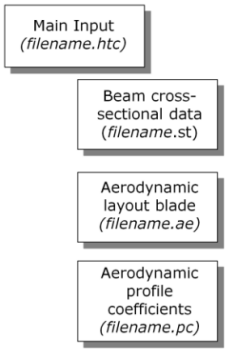

Figure 4.5: Input files needed for the main input of HAWC2 [93].

Structural model

Each component of the wind turbine can be defined into one or more bodies in HAWC2 reference, which have their own reference frame [52]. Furthermore, the body is divided into a collection of Timoshenko beam elements. These elements have a constant mass, stiffness, and inertia. The Timoshenko beam theory that is used in HAWC2 is comparable to the Bernoulli-Euler beam theory model. Timoshenko improved this beam model by including shear. Since a linear formulation is utilized inside each body, only very small deflections are permitted [52]. However, multiple bodies must be modeled in order to high deflections. Figure 4.6 visualizes the multibody formulation in HAWC2 in general. HAWC2 can also accurately model blade twists.

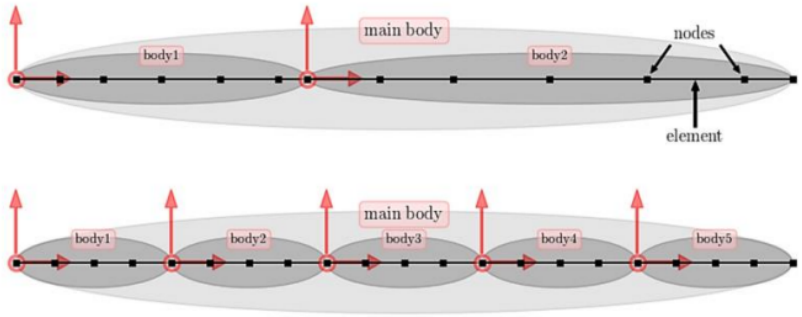

Figure 4.6: Visualization of the multibody formulation in HAWC2 [52].

Coordinate system
For all main bodies in HAWC2, the user can define the coordinate systems [94]. However, the global and blade cross-section coordinate systems are preset. The global Y-direction is positive and points downwind. The global Z-direction is positive downward, which is parallel to the direction of the gravity vector. Figure 4.7 illustrates the different possible coordinate systems in HAWC2 for a HAWT, while Figure 4.8 illustrates the possible coordinate systems for a H-rotor VAWT.

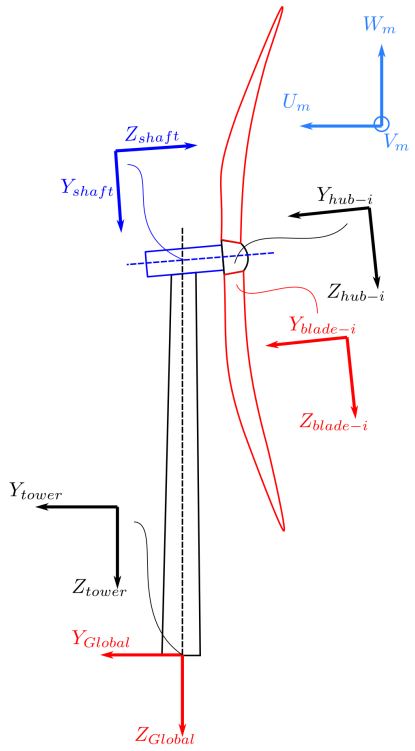

Figure 4.7: Visualization of the HAWC2 coordinate systems for a HAWT [94]. These are the global, tower, shaft, hub, blade, and meteorological coordinate systems.

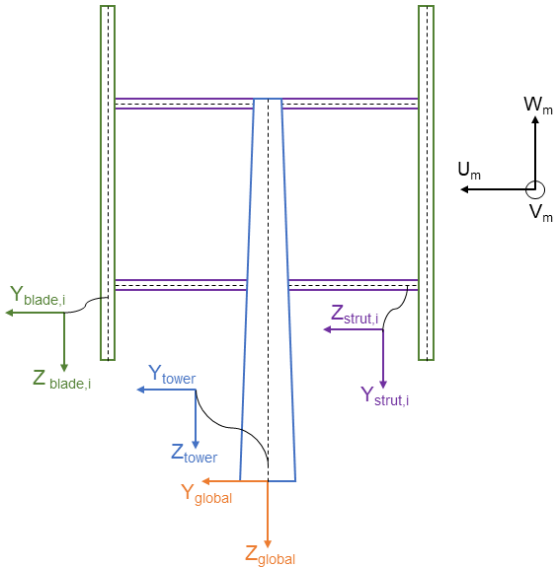

Figure 4.8: Visualization of the HAWC2 coordinate systems for a H-rotor VAWT design. These are the global, tower, blade, strut, and meteorological coordinate systems.

Settings of HAWC2
When the configuration is complete, HAWC2 runs a time-domain simulation of the rotor's behavior. The simulation determines time-dependent aerodynamic forces, structural reactions, power generation, and other performance characteristics. HAWC2 takes into account the general settings of the simulation. Examples of the general settings are the total duration, the time step, and the convergence limits.

Wind model
Not to be forgotten, the wind model should be specified as well. Various general specifications of the wind are required, such as the density and wind speed. Turbulence can be added if wanted, and so are

wind shear and tower shadow. Two aerodynamic methods can be included as well, which are the tip loss method and the dynamic stall method. An example of a wind model within HAWC2 is given below.

```
begin wind;
    density                 1.225;
    wsp                     12.0;
    tint                    0.0;
    horizontal_input        1;                  0=false, 1=true
    windfield_rotations     0.0  0.0  0.0;      yaw, tilt, rotation
    center_pos0             0.0 0.0 -80.5;      at the midpoint of the blade
    shear_format            1  0.0;     0=none, 1=constant, 2=log, 3=power, 4=linear
    turb_format             0;          0=none, 1=mann, 2=flex
    tower_shadow_method     0;          0=none, 1=potential flow, 2=jet
end wind;
```

Aerodynamic model

The aerodynamic model shall be specified as well. The aerodynamics is automatically applied to the rotor. Therefore, the number of the blades should be specified and other data related to the blades and their aerodynamic profile should be provided. Two aerodynamic methods can be included as well, which are the tip loss method and the dynamic stall method. More information about the aerodynamic blocks can be found in the How2HAWC2 manual [1].

```
begin aero;
    nblades             3;
    hub_vec             tower -3;   (normal to rotor plane)
    link    1   mbdy_c2_def     blade1;
    link    2   mbdy_c2_def     blade2;
    link    3   mbdy_c2_def     blade3;
    ae_filename         ./data/MS_ae.dat ;
    pc_filename         ./data/MS_31_pc.dat;
    induction_method    3;   0=none, 1=normal BEM, 2=Near Wake induction, 3=VAWT
    aerocalc_method     1;   0=none, 1=normal
    aerosections        5;
    ae_sets             1 1 1;
    tiploss_method      0;   0=none, 1=normal (Prandtl)
    dynstall_method     2;   0=none, 1=Øye, 2=Beddoes, 3=Gaunaa-Anderson
end aero;
```

Limitations

There are a number of significant HAWC2 limitations that should be considered. These are listed below:

- **Linearity of the material:** In HAWC2, the linear elastic behavior of the material is one of the presumptions made by the Timoshenko beam model [52].
- **Timoshenko beam model:** Internal aeroelastic bend-twist couplings cannot be modeled using the stiffness matrix in HAWC2 [52]. Only the diagonal terms are visible in the stiffness matrix. The stiffness matrix depicts the linear relationship between the forces and moments and the strains and curvatures. Another assumption is that the non-diagonal terms, representing the couplings between bending and torsion in a cross-section, are zero. While this simplification leads to a much faster solving algorithm, it becomes a less accurate model.
- **Eigenvalue analysis:** The eigenvalue solver always assumes that body-to-body restrictions are stiff [95]. This is a limitation.
- **Aerodynamic model:** As mentioned before, the aerodynamic model for VAWTs in HAWC2 is accomplished by condensing the three-dimensional VAWT to a number of two-dimensional cylinders stacked vertically [81]. The model is built on a quasi-steady method and a dynamic inflow model approach familiar to dynamic BEM formulations of HAWT simulations. This model approach still needs to be improved, particularly in terms of determining the appropriate time constants.
- **BEM model:** HAWC2 makes use of the BEM theory, which is founded on a number of simplifying assumptions [52]. Correction models are used to convert the wind turbine into real conditions, but it is still a reduced aerodynamic model. As the BEM model assumes the blade elements are independent, the model does not account for the impact of varying aerodynamic loads from one radiation position to another position. Therefore, variations in induced velocities are flawed.
- **Supported constraint types:** HAWC2 limits the complexity of the model by providing limited supported constraint types [96].

Motivation
This thesis employs two different main tools for simulating the wind turbine under operational conditions. For simulating, HAWC2 is chosen, while BECAS is the pre-processor tool. One of the reasons is the intention to use alternative simulations compared to the reference model. The aeroelastic stability of the model should be looked into, which can be simulated with HAWC2. HAWC2 has the capacity to produce time-domain results.

On the other hand, BECAS is a convenient choice since it can produce structural input files for HAWC2. This makes the pre-processing phase more effective and practical. Both tools are provided by DTU (Technical University of Denmark), which provides the advantage of direct access to specialists and support within the university. Questions and technical issues can be resolved directly with the help of experts. In addition, DTU provides a course on the HAWC2 software, which can be used as a guideline.

4.4. Post-processing

The post-processing phase of the project is highly important for analyzing the enormous amount of data acquired from the simulations run in HAWC2. It turns the raw simulation data into beneficial knowledge and scientific understanding. HAWC2 generates an output file containing data chosen by the user pre-simulation. The chosen post-processing tool is MATLAB since it is widely used and well-known in the academic environment. In order to achieve good comparisons between the models, the collected data is grouped and processed. As a result, useful insights into the performance and behavior of the turbine can be found. This study tries to find the design drivers of the vertical axis wind turbine by conducting rigorous post-processing assessments.

4.4.1. HAWC2 output

The output of HAWC2 is time-series data, which includes information on the aerodynamic behavior, loads, power output, and other variables chosen by the user. HAWC2 provides a wide range of output options to analyze the results of the simulations. These outputs can be accessed through graphical interfaces or exported to other programming tools for further analysis. Moreover, HAWC2 can generate an animation file, in which the wind turbine model can be seen as beams in 3D. The wind turbine model can be visualized over time in the simulation, seeing the deflections and behavior of the wind turbine more physically. Lastly, to check the convergence and errors of the simulation, HAWC2 provides a log file of the simulation.

4.4.2. Post-processing tool

MATLAB is selected as the post-processing tool for this project, as it is a well-known tool in academia and research. MATLAB has a user-friendly interface and extensive functions, which makes it easy for the post-processing phase of such data. The work frame of MATLAB allows for easy editing and presentation of the simulation findings, producing readable graphs for interpreting the data. The comparison between models can be made easily.

4.4.3. Data analysis

As the study tries to find the design drivers of the VAWT design that contribute to improving the effectiveness, performance, and optimization objective, the post-processing analysis can look into various parameters. The impact of the design drivers are evaluated on the power output, structural behavior, and aerodynamic performance of the wind turbine. Therefore, the data analysis leading up to the results is aimed at these parameters. In general, the post-processing exists of the following points:

- Validation of reference model to assess the accuracy and reliability of structural model;
- Statistical analysis of data;
- Comparison between different scenarios;
- Comparison between different designs.

5

Structural design

In this chapter, the structural model which functions as a baseline for the research on finding the design drivers is elaborated. The baseline design is based on the optimized model from Schelbergen's model [5], which is referred to as the reference model. First, the baseline design is discussed, taking into account the optimization outcomes of the reference model. Afterward, the structural models of the wind turbine are described in detail: the rotor consists of the blades, struts, and tower. These are all made as described in the Methodology (Chapter 4). Ultimately, an overview of the rotor model in HAWC2 is presented.

5.1. Reference model

This section gives an overview of the baseline design of the reference model, which is obtained from the work of Schelbergen [5]. Moreover, the geometry and performance parameters have been included in order to create the structural model later on. As the reference model underwent an optimization procedure, the optimization results and the process are also addressed.

5.1.1. Baseline design

The reference model is a H-rotor with 3 blades. The blades consist of the same cross-section over its whole length. Every blade is connected with two struts to the tower. However, as it can be seen in Figure 5.1, the reference model does not contain a tower. How this is fixed for the HAWC2 model will later be discussed in Section 5.5. The struts have a rectangle cross-section and all struts have the same properties.

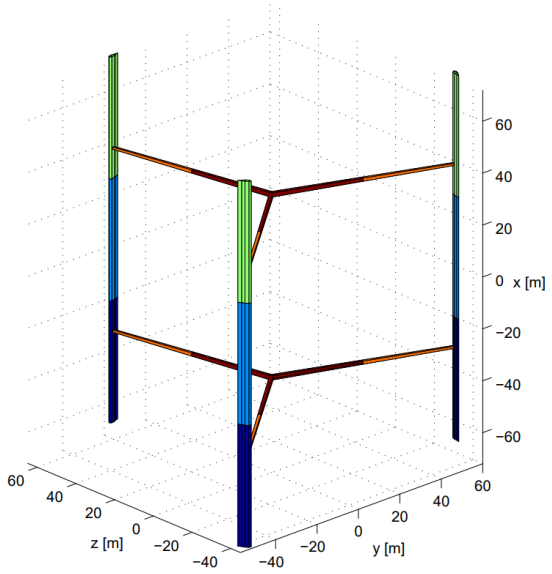

Figure 5.1: The reference model is an evaluated 3-bladed H-rotor [5].

Baseline parameters

In Table 5.1, the geometry and performance parameters of the baseline design are stated. The model has an aspect ratio (diameter-to-height ratio) of 1, which means that the blades have the same length as the diameter of the rotor. The strut itself has half of the length of the blade.

Table 5.1: Baseline geometry parameters of the H-rotor of the reference model [5].

Geometry/Performance parameter	Symbol	Unit	Value
Rotor diameter	D	m	141
Rotor radius	R	m	70.5
Rotor height	H	m	141
Diameter-to-height ratio	D/H	-	1
Chord length	c	m	4.70
Twist	θ_t	deg	-1.5
Projected rotor area	A_p	m^2	19,881
Power capacity	P	MW	9.0

5.1.2. Optimization results

In this subsection, the optimization process of the reference model is shortly summarized, followed by the optimization results for the blade and the strut.

Optimization process

Schelbergen made his optimization code, which can call the FEM solver ”MSC Nastran”. His thesis focuses on optimizing the rotor shape and its structural size. The optimization is based on minimizing the rotor’s cost while maximizing its power output. The power output of a turbine relates linearly with the rotor area, which the rotor’s shape can impact. From this, the mass-to-area ratio is used to evaluate the structural rotor performance. It is assumed that the tip speed ratio and blade solidity are kept constant; thus, the power coefficient shall not change appreciably. This coefficient is held constant as well. Besides, it is assumed that the cost of the rotor is a linear function of the mass of the rotor. Operation and maintenance are neglected as they are independent of the rotor shape. The optimization shall result in changing the laminate thickness of CFRP in the blades and struts.

Blade

The optimization results related to the blade are written down in Table 5.2. The work of Schelbergen [5] provides the results of the optimization in a range for the laminate thicknesses for every structural member (girder, shear web, and skin). The blade contains the same cross-section over its whole length.

Table 5.2: Sizing optimization results of the H-rotor for the blades [5].

Parameter	Parameter	Unit	Value
Number of sections at blade	$n_{\text{sec,blade}}$	-	1
Maximum thickness of girder	$t_{\text{girder,max}}$	mm	28.2
Minimum thickness of girder	$t_{\text{girder,min}}$	mm	-
Maximum thickness of shear web	$t_{\text{sw,max}}$	mm	8.0
Minimum thickness of shear web	$t_{\text{sw,min}}$	mm	-
Maximum thickness of skin	$t_{\text{skin,max}}$	mm	7.9
Minimum thickness of skin	$t_{\text{skin,max}}$	mm	-

Struts

The optimization results for the struts are written down in Table 5.3. The reference model specifies two cross-sections along the strut, one at the tip and one at the base of the strut. The cross-section of struts are two different rectangles.

Table 5.3: Sizing optimization results of the H-rotor for the struts [5].

Parameter	Symbol	Unit	Value
Number of struts	n_{struts}	-	2
-	$n_{\text{sec,struts}}$	-	1
Maximum thickness of struts	$t_{\text{struts,max}}$	mm	22.9
Minimum thickness of struts	$t_{\text{struts,min}}$	mm	-
Height of cross-section at tip	$h_{\text{struts,tip}}$	m	0.72
Width of cross-section at tip	$w_{\text{struts,tip}}$	m	0.80
Height of cross-section at base	$h_{\text{struts,base}}$	m	1.60
Width of cross-section at base	$w_{\text{struts,base}}$	m	1.18

5.2. Material properties

Schelbergen [5] made the decision to use Carbon Fiber Reinforced Plastics (CFRP) based on Ashuri's work [89]. Upscaling of wind turbines is found to be constrained by the rise in blade mass [5]. To reduce the mass of the blades and the inertial loads while also enabling further upscaling, CFRP is chosen in the design over GFRP. As a result, CFRP laminates are the main emphasis of the optimization of Schelbergen. The material properties of a CFRP ply are put in Table 5.4.

The core is made of low-density material, which is used to increase local inertia in specific areas by bridging the gaps between the faces of high-strength material [48]. Table 5.5 shows the material properties of the core.

Table 5.4: Materials properties of standard carbon-fiber UD [97].

Parameter	Unit	Value
E_1	GPa	142
E_2	GPa	7.79
E_3	GPa	7.79
ν_{12}	-	0.34
ν_{13}	-	0.53
ν_{23}	-	0.34
G_{12}	MPa	4.0
G_{13}	MPa	2.55
G_{23}	MPa	4.0
ρ	kg/m^3	1550

Table 5.5: Material properties of the core material [92].

Parameter	Unit	Value
E_1	MPa	50
E_2	MPa	50
E_3	MPa	50
ν_{12}	-	0.4
ν_{13}	-	0.4
ν_{23}	-	0.4
G_{12}	MPa	17.857
G_{13}	MPa	17.857
G_{23}	MPa	17.857
ρ	kg/m^3	80

5.3. Blade

As mentioned in Chapter 4, the structural model of the blade is created in BECAS with Airfoil2BECAS. Firstly, the airfoil profile (airfoil coordinates) are obtained and moved to align with the coordinate system of Airfoil2BECAS. Moreover, the material properties of Section 5.2 are given as input, while the laminate layup for every structural member in the blade is also provided. As a result, the structural input file for HAWC2 is obtained with the important cross-section parameters.

5.3.1. Airfoil

An optimized airfoil profile has been used in the reference model, which can be seen in Figure 5.2. The coordinates have been read and entered in MATLAB, in which the coordinates have been adjusted to the correct coordinate system of Airfoil2BECAS. In addition, the profile is normalized with the chord length (c). It can be seen that the airfoil profile is symmetric over the x-axis.

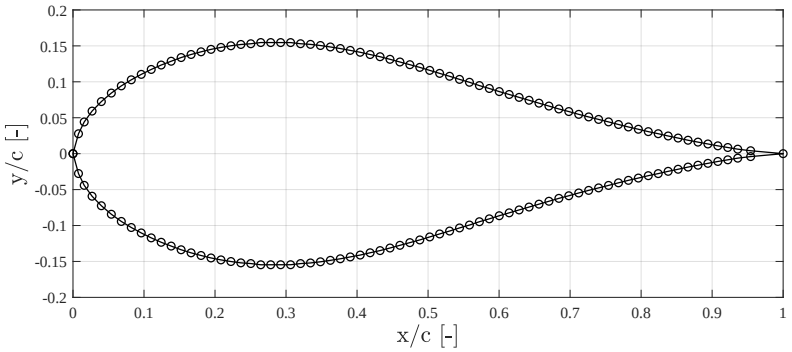

Figure 5.2: Chosen airfoil profile in the reference model, normalized with the chord length (c).

As mentioned before, the cross-section of the blade can be divided into three structural members: spar caps (also named: girders), shear webs, and skin. These structural members are not visualized in Figure 5.2, but the structural members were presented in Figure 2.18. The spar caps are placed at 15% and 45% of the normalized chord. The upper and lower surfaces between these two shear caps are called the spar caps or girders, while the remaining surfaces are called the skin.

5.3.2. Laminate layup

The structural members are built of different laminates, tailored for its application [5]. In Table 5.6, the layup of the laminates per structural member in degrees can be found. The core is placed at the mid-plane of the laminate so at the symmetry plane. The thickness fraction of the core refers to the portion of the overall composite thickness that the core material takes up. The thickness fraction of the core is stated as the ratio of the core thickness to the laminate's overall thickness.

Table 5.6: Layup of laminates per structural member and their thickness fraction of the core [5].

Structural member	**Layup of laminate** [deg]	**Thickness fraction of core** [-]
Skin	$[0_2/90/(45/\text{-}45)_2]_s$	0.65
Shear web	$[0/(45/\text{-}45)_2/90/45/\text{-}45]_s$	0.65
Girder	$[0_6/45/\text{-}45]_s$	-

Figure 5.3 illustrates the build-up of the different laminates for all three structural members of the blade (skin, shear web, and girder).

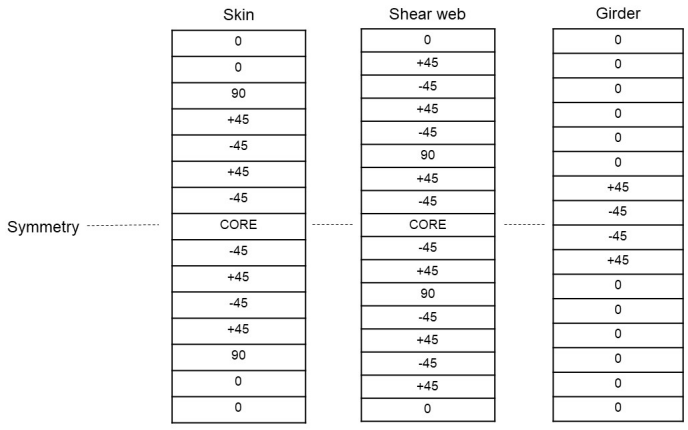

Figure 5.3: Lay-up of the laminates of the structural members of the blade (skin, shear web, and girder).

5.3.3. Structural model

Based on the optimization results of the reference model, the structural model of the blade can be made.

Overview of models

As a thickness range has been given in the optimization results, one model is made based on the maximum thickness of this range. However, as the laminate thickness is also investigated as a design driver, two other models are created as well (V1 and V2). Table 5.7 shows the specific thicknesses for each model. The maximum thickness model (often recalled as max. thickness model or only max) takes the maximum thickness for every structural member. The V1 model has a uniform thickness over the whole section of the blade. The thickness of each structural member is equal to each other and relatively small (5 mm). The V2 model has smaller thicknesses but keeps around the same ratios as the max. thickness model.

Table 5.7: The evaluated models are based on different thicknesses of the structural members in the blade.

	Thickness t [mm]		
Structural member	**Max. thickness model**	**V1**	**V2**
Girder	28.2	5.0	17.6
Skin	7.9	5.4	5.4
Shear web	8.0	5.0	5.0

Mesh

Based on the pre-processing in Airfoil2BECAS, BECAS can make a 2D finite element mesh. It is important to set the half-chord at the origin (0,0). For this reason, the airfoil coordinates need to move to meet this condition. Similarly, the profile must be mirrored so that the sequence of structural members is correct in the software. Figure 5.4 illustrates the mesh while it also provides the elastic center, shear center, mass center, and elastic axes orientated by BECAS.

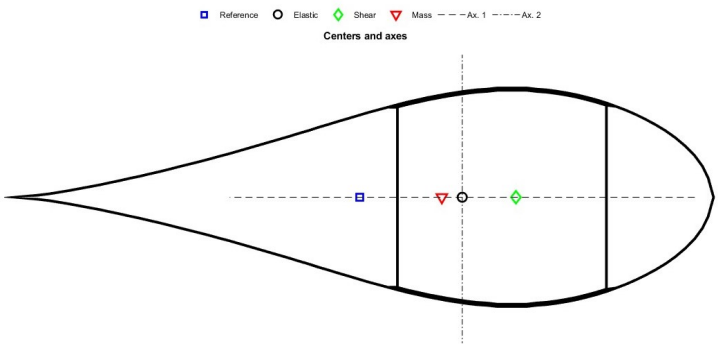

Figure 5.4: Cross-section of an airfoil with the elastic center, shear center, mass center, and elastic axes orientated found by BECAS.

Moreover, Figure 5.5 shows the finite element mesh (total and zoomed-in view of the connection between the spar cap, the girder, and the skin). The meshes for the other blade models can be found in Appendix B.

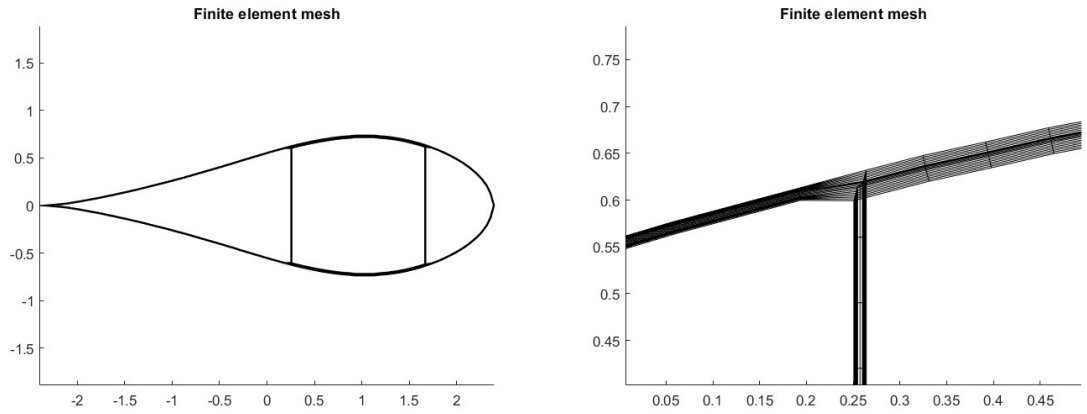

Figure 5.5: The 2D Finite Element Mesh (FEM) of the airfoil produced by BECAS.

Finally, the different materials can be recognized in Figure 5.6. It shows the material number, which can be recognized with a color in the color bar. As there are only two materials in the blade, a good distinction can be made between the two. Thus, it can easily be seen that the girders do not consist of the core material in their layup.

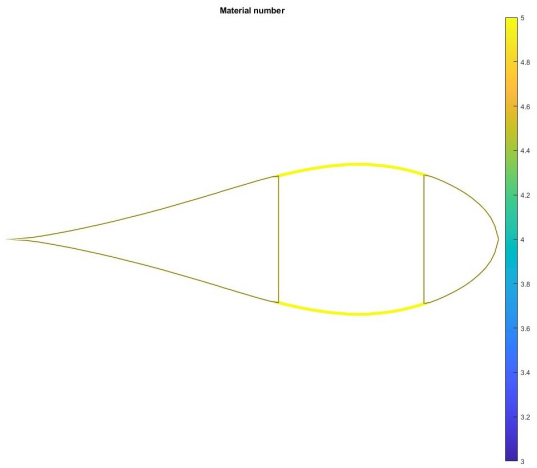

Figure 5.6: The different materials in the cross-section of the airfoil found by BECAS. Each material number, and therefore a color, represent one of the material types used.

5.3.4. Cross-sectional parameters

BECAS automatically generates input for HAWC2, which is based on a fully populated stiffness matrix (FPM) with additional coupling terms. Using FPM allows for the modeling of bend-twist coupling. FPM captures the structural properties more completely than the standard HAWC2 beam model. This is because the material of the airfoil is an-isotropic. Besides the stiffness matrix, the input file also contains the station, mass per unit length, the center of mass, radius of gyration, structural pitch, and the elastic center. The important cross-sectional parameters of the blade for all three models are put in Appendix B.

5.3.5. Aerodynamic input

As mentioned in Chapter 4, HAWC2 requires data on the aerodynamic layout profile and the aerodynamic profile coefficients. The profile coefficients for the airfoil can be obtained with QBlade, which gets the airfoil data in the operational range until $C_{l,max}$ (stall angle). In the software QBlade, which uses XFoil, the NACA0031 profile lays the best on top of the optimized reference airfoil. The choice to choose a NACA profile over the optimized airfoil profile is related to software issues: the software cannot process the optimized airfoil of the reference model. The difference in the airfoil layout can be seen in Figure 5.7.

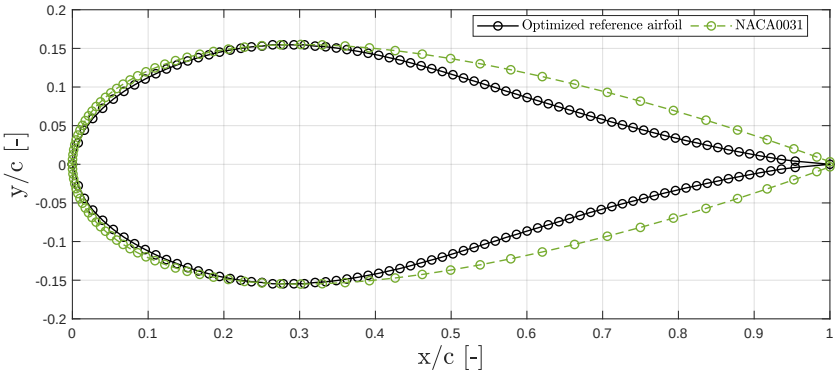

Figure 5.7: The NACA0031 profile lays over the optimized airfoil profile used in the reference model.

QBlade extrapolates the airfoil data (lift coefficient, drag coefficient, and moment coefficient) based on the Reynolds number (Re) and the Mach number (Ma). The Reynolds number and Mach number can be calculated with Equation 5.1. In these expressions, U is the velocity of the rotor and c is the speed of sound in the medium.

$$Re = \frac{\rho U c_s}{\mu} \qquad Ma = \frac{U}{c} \tag{5.1}$$

The wind turbine has a tip speed ratio of $\lambda = 4.5$, while the rated wind speed is $V_{rated} = 12$ m/s. This leads to a moving velocity $U = 54$ m/s. In dry air, the speed of sound is $c_s = 340$ m/s. Moreover, $\rho = 1.225$ kg/m^3 is the density of air, $c = 4.7$ m is the chord length and $\mu = 1.789 \cdot 10^{-5}$ kg/ms is the dynamic viscosity of air. From these expressions, the Reynolds number is found at $Re = 1.54 \cdot 10^7$ and the Mach number at $Ma = 0.159$. The model can eventually consider in-compressible flow due to its relatively low speed ($Ma < 0.3$) [98]. The extrapolated data plots can be found in Appendix C.

Table 5.8: The Reynolds number and the Mach number at operating conditions.

Parameter	Symbol	Unit	Value
Reynolds number	Re	-	$1.7 \cdot 10^7$
Mach number	Ma	-	0.159

5.4. Strut

The strut has a simple geometry, consisting of a tapered beam with a rectangular cross-section [5]. The cross-section is given for two positions along the struts, which are the tip and the base of the strut. The width and the height of the cross-section at both ends of the struts are the variables in the optimization process of the reference model.

5.4.1. Cross-sections

The height and width of the strut are constant and can be read from Table 5.3. Therefore, the cross-sections of the strut can be visualized in Figure 5.8. The centroid of both rectangles is at (0,0).

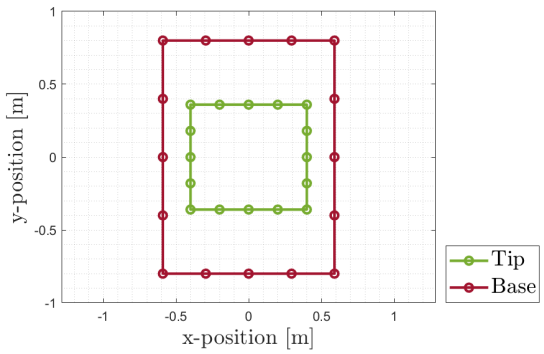

Figure 5.8: The cross-sections of the strut.

5.4.2. Placement of struts

The struts are placed with a distance x_{strut} from the center line (the midpoint of the blade). A visualization of this can be seen in Figure 5.9.

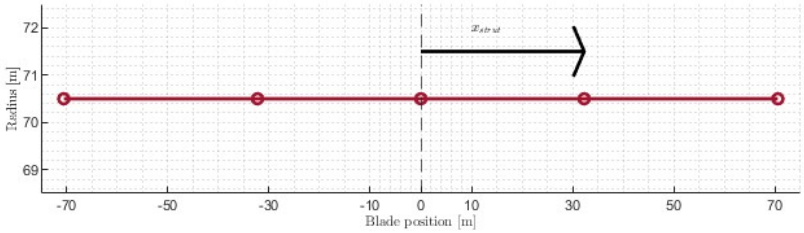

Figure 5.9: The blade as a beam, with the position of the strut defined as x_{strut}.

In the reference model, the position of the struts on the blade is set at $x_{\text{strut}}/H = 0.25$, in which H is the length of the blade. Table 5.9 provides an overview of the main geometry parameters of the strut itself.

Table 5.9: Geometry parameters of the struts.

Parameter	Symbol	Unit	Value
Length of strut	L_s	m	70.5
Position of strut from the blade's middle-point	x_{strut}	m	35.25

5.4.3. Laminate layup

The struts are made of CFRP as well. The layup of the laminates is visible in Table 5.10, while providing the thickness fraction of the core. The thickness fraction of the core is the ratio between the thickness of the core and the thickness of the laminate.

Table 5.10: Layup of laminates of the strut and its thickness fraction of the core [5].

Structural member	**Layup of laminate** [deg]	**Thickness fraction of core** [-]
Strut	$[0_6/45/\text{-}45]_s$	0.65

5.4.4. Structural model

The structural design of the struts is made out of two cross-sections: one at the tip and one at the base of the strut.

Input

For every structural model (max. thickness model, V1, and V2), the same strut is utilized. Table 5.11 presents the thickness of the strut laminate, while the height and width of the two cross-sections can be read from Table 5.3.

Table 5.11: The evaluated models all have the same thickness and therefore cross-section of the strut.

Parameter	Symbol	Unit	Value
Thickness of strut	t_{struts}	mm	22.9

Mesh

Based on the optimization results of the reference model, the finite element mesh of the strut can be made. BECAS can also make a 2D finite element mesh of other shapes than airfoils. The cross-section of one point at the strut can be seen in Figure 5.10, which also provides a visualization of the elastic center, shear center, mass center, and elastic axes orientated. The elastic center, shear center, and mass center all align at one point. Besides, Figure 5.11 shows the distinction between the two materials in the strut.

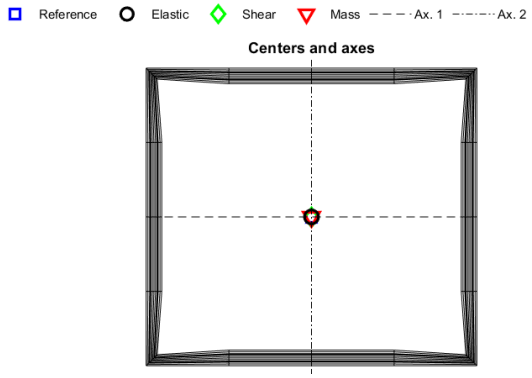

Figure 5.10: Cross-section of the strut with the elastic center, shear center, mass center, and elastic axes orientated found by BECAS.

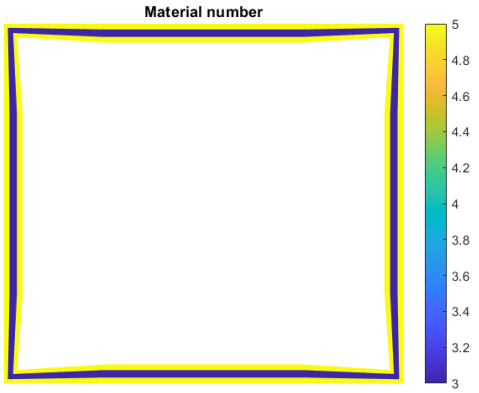

Figure 5.11: The different materials in the cross-section of the strut found by BECAS.

In addition, better visualization of the 2D finite element mesh can be seen in Figure 5.12. It provides also a zoomed-in view of one of the corners. It can be observed that the thickness becomes smaller at the corners. As the cross-section is a rectangle with sharp corners and it is one continuity in regions (one), Airfoil2BECAS makes the sharp corners smoother.

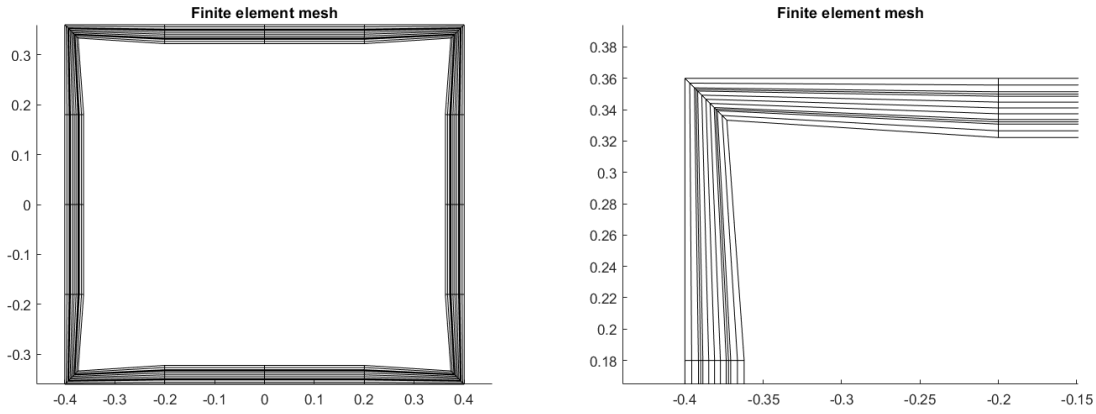

Figure 5.12: 2D Finite Element Mesh of the strut cross-section made in BECAS.

5.4.5. Cross-section parameters

The output file for HAWC2 is calculated with BECAS. The calculation is based on the fully populated stiffness matrix. Besides the stiffness matrix, the input file also contains the station, mass per unit length, the center of mass, the radius of gyration, structural pitch, and the elastic center. Those cross-sectional parameters are put in Appendix B.

5.5. Tower

The reference model was analyzed without a tower. However, for HAWC2 simulations, a tower is needed and therefore added. The tower is based on the design of Huisman. As Huisman made a design that is similar in size which is ideal to use, the tower can be adjusted to fit the reference model. The material of the tower will be structural steel. Structural steel has various advantages that can be named. It is a lightweight, durable material and has a high strength-to-weight ratio [99]. Structural steel offers the structural advantages of a high load capacity. Other advantages are that structural steel has tremendous tensile strength and is corrosion-resistant. Moreover, steel has a low wastage rate because of its versatility. Compared to other metals, structural steel is typically lower in cost. However, due to the complex fabrication and assembly of steel components, the manufacturing costs can be higher with longer lead times [100]. On top of that, towers made of steel can be large and heavy, making them more difficult to move. The use of specialized transportation methods could raise costs and complicate logistics.

5.5.1. Structural model

The tower is a thin-walled cylinder, and it is divided into three cross-sections. The cross-section of the tower is a circle, but the diameter changes over the height. This can be seen in Figure 5.13. The distances h_1 and h_2 are dependent on the rotor's size and the placement of the struts. At h_1 the lower strut is positioned, while at h_2 the upper strut is positioned.

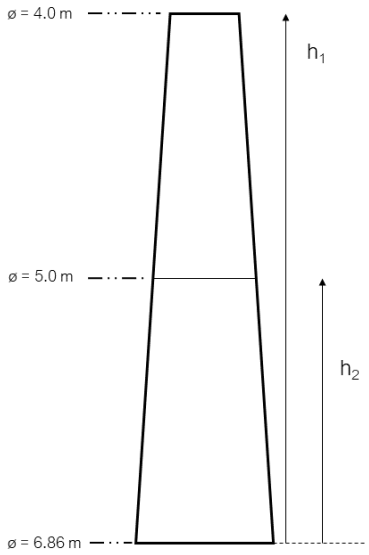

Figure 5.13: Visualization of the tower in front view with the diameters and heights (h_1 and h_2) defined.

The varying diameters of the tower laying over each other can be seen in Figure 5.14. The diameter becomes smaller with the height of the tower.

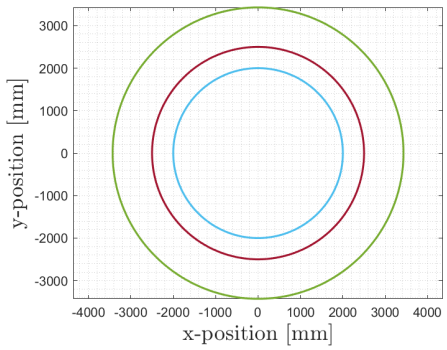

Figure 5.14: The three cross-sections of the tower are circles.

The thickness distribution of the tower is stated in Table 5.12. It gives an overview of the section

heights, the diameter of the tower, and its thickness. The first section is at the base connection. The second section is in the middle of the tower and the last section is at the top. In each section, the wall thickness is constant.

Table 5.12: Wall thickness distribution of the tower.

Height h [m]	**Outer diameter** $\varnothing$ [m]	**Thickness** t [mm]
0.00	6.86	40
h_2 = 43.25	5.00	40
h_1 = 86.50	4.00	40

5.5.2. Material properties

The material properties of structural steel (St52) are written down in Table 5.13. The material type can also be found under the name ”S355JR”.

Table 5.13: Material properties of structural steel (St52 / S355JR) [101].

Property	**Symbol**	**Unit**	**Value**
Young’s modulus	E	GPa	210
Tensile stress	σ	MPa	345
Shear’s modulus	G	MPa	80.7
Poisson’s ratio	ν	-	≈ 0.3
Density	ρ	kg/m^3	7850

5.5.3. Cross-section parameters

The cross-section parameters are calculated based on equations from the work of Bak et al. [102] on the DTU 10 MW Reference Wind Turbine. Below, they are written down for each cross-sectional parameter. In Appendix A, an overview of the needed parameters and their definition is provided.

Cross-sectional area

The cross-sectional area (A_{cs}) can be calculated with Equation 5.2, in which D is the outer diameter and d is the inner diameter [102].

$$A_{cs} = \left(D^2 - d^2\right) \frac{\pi}{4} \tag{5.2}$$

Mass per unit length

The mass per unit length (m) can be calculated with Equation 5.3, in which ρ is the mass density of the material.

$$m = A_{cs} \cdot \rho \tag{5.3}$$

Radius of gyration

The radius of gyration (r_g) is given by Equation 5.4, which is around the principal bending axis (y_e). Due to symmetry, r_{iy} is equal to r_{ix} [m] [103]. In Figure 4.5, the principal bending axes can be seen.

$$r_g = \frac{1}{4}\sqrt{D^2 + d^2}. \tag{5.4}$$

Second moment of area

The second moment of area (I) can be calculated with Equation 5.5.

$$I = \left(D^4 - d^4\right) \frac{\pi}{64} \tag{5.5}$$

Torsional stiffness constant
The torsional stiffness constant (K) can be calculated with Equation 5.6.

$$K = \left(D^4 - d^4\right) \frac{\pi}{32} \tag{5.6}$$

Elastic and shear center
The elastic center (x_e, y_e) is the intersection point for the principal bending moments. As the tower is axisymmetric around z, this point is at the origin [103]. Furthermore, the shear center (x_s, y_s) and the elastic center are at the same point, as the cross-section is symmetric about x and y. Therefore, it can be concluded that: $x_e = x_s = 0$ and $y_e = y_s = 0$.

Results
Table 5.14 lists all the mass properties and the cross-section stiffness of the tower.

Table 5.14: Cross-section stiffness and mass properties of the tower.

Height [m]	**Cross section area** [m^2]	**Mass per unit length** [ton/m]	**Radius of gyration** [m^4]	**Second moment of area** [m^4]	**Torsional stiffness constant** [m^4/rad]
0.00	0.85	6.67	2.39	4.85	9.71
h_2	0.62	4.89	1.75	1.92	3.83
h_1	0.50	3.91	1.40	0.98	1.95

5.6. Overview of the rotor
The total structural model of the wind turbine is made in HAWC2. A visualization of this model can be seen in Figure 5.15. There is no controller available for a VAWT in HAWC2. Therefore, the simulations can only be done at a fixed, constant rotational speed.

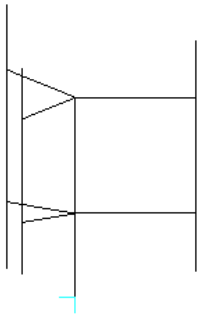

Figure 5.15: The HAWC2 model of the H-rotor.

5.6.1. Bodies
Every component is represented as a beam. Each blade and strut are a main body, while the blade consists of three bodies within. The strut does only have one body, and so do the base and tower. The bodies are divided among the number of nodes. Meanwhile, the nodes are placed symmetrically around the middle point of the blade. The twist of the blade is added to their main bodies.

5.6.2. Connections
In order to create more intricate systems, HAWC2 offers a variety of constraints (connections) [96]. When using HAWC2, only the mentioned constraints in this section can be used when bodies are connected. Firstly, there are multiple bearing options. For this model, type Bearing 3 is used. Bearing 3 is a bearing with a constant specified angle velocity. The fixed bearing speed is set at the rotational speed of the rotor. The bearing is set between the base body and the tower body.

Furthermore, HAWC2 also has other constraint types which are not bearing-based. First of all, the wind turbine will be fixed to the ground. For this, ”Fix0” will be used, which indicates that the body is clamped to the ground. The reference model simulates the connection of the strut to the tower by clamps. This can be

modeled in HAWC2 with ”Fix1”, which indicates a clamped connection. Moreover, the reference model simulates the blade-strut connection with the use of rigid body elements. The nodes connected by the rigid body elements may move relative to one another only as a unit. In HAWC2, this is also connected by ”Fix1”.

The two constraint types and the bearing type used in this project and their restricted Degrees of Freedom (DoF) are noted in Table 5.15. All types of bearings and constraints can be read in Appendix D.

Table 5.15: The restricted Degrees of Freedom for the two different constraint types used in the HAWC2 model.

Constraint type	# DoF	Degrees of Freedom	Between bodie(s)
Bearing3: Fixed speed bearing	1/6	Rotate around its axis with constant angular velocity	Base & tower
Fix0: Fixed to the ground	0/6	None (All translations & rotations)	Base
Fix1: Clamped connection	0/6	None (All translations & rotations)	Tower & struts, struts & blade

6

Results

This chapter delivers the results of the HAWC2 simulations, looking into various aspects of the wind turbine model. The simulations are done at the operating conditions described in Section 6.1. The simulations are intended to evaluate design drivers on their impact on the structural integrity, aeroelastic stability, and performance of the rotor. Different sections of this chapter will cover various investigations to design drivers, such as the blade laminate thickness and strut placement. An overview of the simulations and what they investigate can be found in Section 6.2. Section 6.3 provides the simulation settings in HAWC2. The results of the investigations are put in Section 6.4 to Section 6.8. The investigations are provided with results based on performance, aerodynamic loads, natural frequencies, and blade behavior. Moreover, the reference model is compared with the work of Schelbergen [5] to the found results in Section 6.4 and Section 6.5. The results contribute to the understanding of the VAWT design and they can offer valuable guidance for the design and performance of VAWTs.

6.1. Operating conditions

In the simulations of the reference model, the evaluated load conditions are constrained to normal operating conditions in upwind (UW) and downwind (DW) positions. The assumed normal operating conditions are listed in Table 6.1. Both aerodynamic, centrifugal, and gravitational loading are taken into consideration. Moreover, the turbine is intended to have a 20-year lifespan, of which 35% of that time will be spent operating at rated wind speed.

Table 6.1: Normal operation conditions for the model of Schelbergen [5].

Parameter	Symbol	Unit	Value
Rated wind speed	V_{rated}	m/s	12
Tip speed ratio	λ	-	4.5

With the wind condition given in Table 6.1 and the expression in Equation 2.22, the rotational speed of the rotor can be derived with the tip speed ratio. The rotational speed is set at $\omega = 0.766$ rad/s for a tip speed ratio of $\lambda = 4.5$. Additionally, to look at the wind turbine's behavior, different tip speed ratios are shortly investigated as well. This is done by changing the rotational speed to match the tip speed ratio with the constant operating conditions in HAWC2. An overview is given in Table 6.2.

Table 6.2: Constant rotational speed for each tip speed ratio under the same operating conditions.

TSR [-]	**Rotational speed** ω [rad/s]	**TSR** [-]	**Rotational speed** ω [rad/s]
1	0.17	6	1.02
2	0.34	7	1.19
3	0.51	8	1.36
4	0.68	9	1.53
4.5	0.77	10	1.70
5	0.85		

6.2. Overview of simulations

Table 6.3 provides an overview of all models and their specifications which will be compared to one another. This is done to investigate certain influences on the wind turbine. This is also specified in Table 6.3. Moreover, their case numbers are specified. Note that some models can have the same specifications but are noted with different case numbers. The different blade models (Max, V1, and V2) have all different laminate thicknesses, which can be found back in Table 5.7 in Chapter 5. The Huisman model is featured in Chapter 7, along with its outcomes.

Table 6.3: Overview of all simulations and the comparisons made between some to investigate certain parameters of the wind turbine.

Model speficiations	Stiff / Flexible	Blade model	Dyn. stall model	#	To investigate
Reference model	Flexible	Max.	Øye	A1	Aerodynamic behavior of model
Reference model	Stiff	Max.	Øye	A2	
Reference model	Flexible	Max.	Øye	L1	Laminate thickness
Reference model	Flexible	V1	Øye	L2	
Reference model	Flexible	V2	Øye	L3	
Reference model	Flexible	V1	Øye	D1	Dynamic stall model
Reference model	Flexible	V1	MHH B-L	D2	
Struts at x/H =0.20	Flexible	V1	MHH B-L	P1	Placement of struts
Struts at x/H =0.23	Flexible	V1	MHH B-L	P2	
Struts at x/H =0.25	Flexible	V1	MHH B-L	P3	
Struts at x/H =0.27	Flexible	V1	MHH B-L	P4	
Struts at x/H =0.29	Flexible	V1	MHH B-L	P5	
Struts at x/H =0.33	Flexible	V1	MHH B-L	P6	
Struts at x/H =0.35	Flexible	V1	MHH B-L	P7	
Reference model	Flexible	V1	MHH B-L	S1	Additional diagonal strut
Model with diagonal strut	Flexible	V1	MHH B-L	S2	
Reference model	Flexible	V1	MHH B-L	U1	Upscaling effects
Upscaled to H/D = 1.25	Flexible	V1	MHH B-L	U2	
Upscaled to H/D = 1.5	Flexible	V1	MHH B-L	U3	
Huisman model	Flexible	NACA0021	MHH B-L	H1	

6.3. Simulation settings

In this section, a thorough overview of the simulation parameters in HAWC2 is given. The simulation settings include several parameters that are important for effectively simulating and researching the wind turbine's behavior. With this summary, a clear knowledge of the simulation framework should be created. Furthermore, it would facilitate replication of the results found in the subsequent analyses by specifying these parameters.

Time stop

The simulations run for at least 350 to 400 seconds. It is expected that in the first $\sim$ 100/150 seconds, the wind turbine will start up. This is the transient period of the simulation. Therefore, results should be looked at after this moment, when there are no effects visible anymore.

Solver type

The solver type is set at "sparse Newmark", which is faster than the dense Newmark (default setting) [1]. This type is recommended.

Convergence limits

There are various convergence limits that must be obtained at every step [1]. These can be read below.

- Residual on internal-external forces (5.0E-6);
- Residual on increment (1.0E-6);
- Residual on constraint equations (1.0E-4);

Maximum iterations

The number of maximum iterations within a time step is set at 500.

Newmark-beta solution
The computation time is almost real-time (for a land-based turbine), which is obtained using a Newmark-beta solution scheme together with Newton-Raphson iterations within each time step [104]. To solve certain differential equations, the Newmark-beta solution is a numerical integration technique [105]. It is frequently used to numerically evaluate the dynamic reaction of solids and structures, such as when modeling dynamic systems with finite elements.

Newton-Raphson method
The Newton-Raphson method, sometimes known as Newton's method, is a technique for locating a (non-linear) equation's roots [106]. The method is named after Isaac Newton, who first discovered it in 1736, and Joseph Raphson, who first described it in 1690. The method is based on an initial guess, then linearizing the function, and then iteratively refining the solution to a certain accuracy (convergence limit). The method might not converge appropriately on the desired root if the initial guess is too far from the root.

Newmark settings
The parameters γ and β are used to govern the numerical integration scheme for solving second-order ordinary differential equations (ODEs) in the time domain. The Newmark settings are set at default: beta value is $\beta = 0.27$ and gamma value is $\gamma = 0.51$ [1]. Furthermore, the time increment is set at $\Delta t = 0.02$ seconds.

Aerodynamics
The parameters of the aerodynamic specification of the rotor are set up with the main command block "aero". First of all, the number of blades is specified ($B = 3$). Files containing aerodynamic layouts and profile coefficients are needed. The aerodynamic calculation method chosen is the normal setting. The dynamic stall model is specified for each simulation and comparison.

6.4. Aerodynamic behavior of wind turbine

This section thoroughly examines the aerodynamic output produced by the HAWC2 model. The wind turbine has two versions, which shall be compared to one another. The flexible model is based on the reference model, while the other model is absolutely stiff. The model specifications can also be read in Table 6.3.

By examining the stiff model (A2), pure aerodynamic behavior can be separated from any structural impacts. The combined effects of structural dynamics and aerodynamics can be examined with the flexible model (A1). By making the wind turbine very stiff, the primary goal is to isolate and study the aerodynamic properties. The stiff model assumes little flexibility in the structural components, the aerodynamic performance is more accurate. With the stiff model, the aerodynamic behavior and the impact of aerodynamic parameters on power production can be examined. Then, by comparing the very stiff wind turbine model to the flexible one, the structural characteristics of the wind turbine can be researched. This comparison aids in evaluating how the more flexible model affects the power output. The relationship between aerodynamic and structural features may be fully understood by contrasting the flexible and stiff models.

6.4.1. Power output

For a number of reasons, it is necessary to examine the power output of both the flexible model and the stiff wind turbine model. Foremost, the aerodynamic power output is directly related to the production of electrical energy. By comparing the models, the effects of the flexibility of the rotor on power generation are evaluated. As higher power output can result in more revenue and a better return on investment, measuring the power output also aids in the economic viability and cost-effectiveness of wind turbine designs.

Power vs. Tip speed ratio
A power vs. tip speed ratio (TSR) curve is made for both models. The curve offers important details regarding the aerodynamic capabilities of the wind turbine design. Furthermore, the ideal operating region can be determined where the turbine generates the most power by examining the curve. The ideal rotor speed (or TSR) can be pinpointed at which the turbine performs at its peak efficiency. Additionally, the curve makes it easier to assess how the turbine will behave in various wind situations. It reveals how the turbine reacts to changes in rotor speed or wind speed. Finally, the curve can be used as a standard for comparing the performance of various wind turbine designs. By contrasting the power curves, design revisions can be evaluated.

In Figure 6.1, the power vs. tip speed ratio curve for both the very stiff model and the flexible maximum thickness model is shown. The stiff model demonstrates that the aerodynamic input in HAWC2 is adequate. It exhibits effective power generation under varying tip speed ratios (TSRs). As there is no controller in HAWC2, the different TSRs are obtained by changing the rotational speed of the rotor and keeping the wind speed the same. The flexible, original design performs well up to a TSR $= 4$. Unexpectedly, the power drops off at TSR $= 4.5$, which corresponds to the defined optimum tip speed ratio of the reference model. At TSR $= 5$, the power increases again.

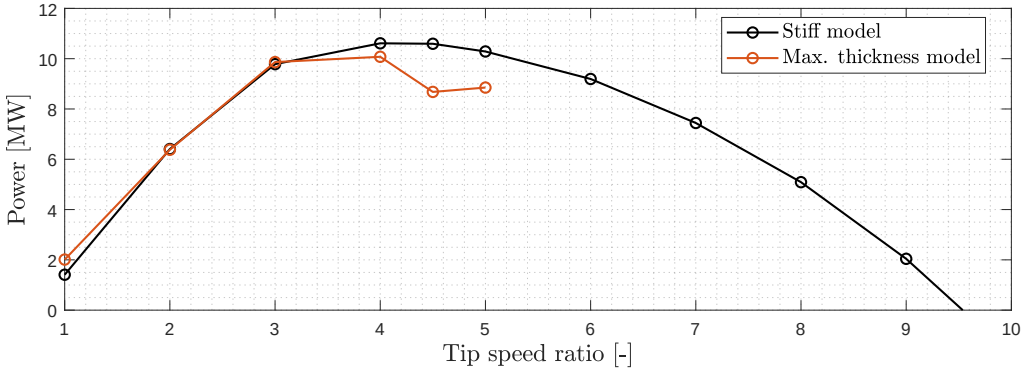

Figure 6.1: The power (P) as a function of the tip speed ratio (TSR), for both the stiff model as the flexible maximum thickness model.

However, when the tip sped ratio is increased once more, the model deteriorates. This can be related to structural instability and the sensitivity to higher TSR values. In reaction to the dynamic forces of the wind, the flexible model's blades are more likely to deform and deflect. This distortion could result in unpredictable and unstable behavior of the rotor. Furthermore, the flexible model may experience non-desired high forces, which could cause the structure to collapse. The reference model is optimized for constant operational conditions, mentioned in Section 6.1. Examination of higher TSRs is not conducted in the report of Schelbergen [5]. The results show that it is crucial not to retain a higher rotational speed of the rotor, as it can lead to system collapse and a decrease in power output.

Even though the power curve does not seem to go correctly at TSR = 4.5, both models will be compared with this specific TSR. This is done to investigate the specific differences and what possibly can lead to such a decrease in power.

Power over time

The stiff and flexible models' power outputs are measured and plotted over time. This can be seen in Figure 6.2. The plot makes it possible to compare the power generation capacities of the two models side by side. The analysis of power output over time shows that the stiff model consistently produces more power, despite the range of fluctuations being similar across the two models. In contrast to the stiff model, the flexible model notably shows a minor delay in attaining its peak power output. The dynamic reaction and the deflection of the blades and struts may be reasonable for this delay.

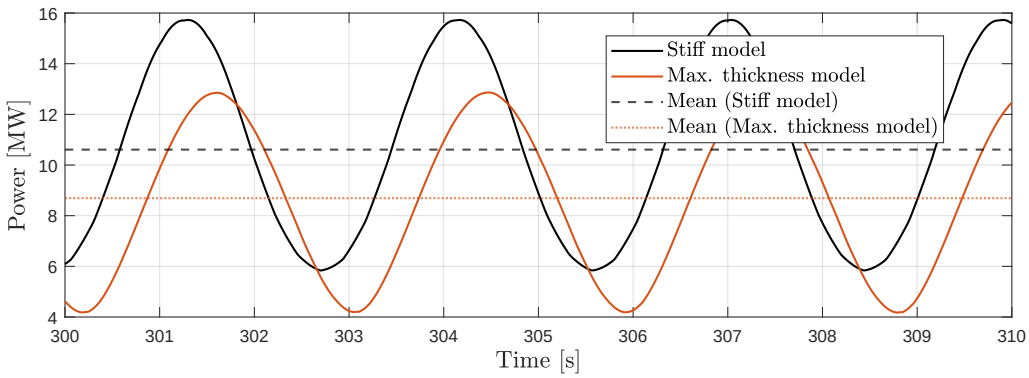

Figure 6.2: The aerodynamic power (P) as a function of time for the stiff model and the maximum thickness model. Their means are provided as well.

Comparison stiff and flexible model
The difference in power output between the stiff and flexible models (max. thickness model) is shortly discussed. In Figure 6.3, it can be seen that range of the angle of attack (AoA) differs significantly. The stiff model reaches higher angles of attack, which corresponds to a larger lift coefficient. This is demonstrated in Appendix C. A larger lift means more torque and therefore power. It is most likely that the flexible model deforms and deflects under wind conditions over a rotation, while the stiff model will not. The flexible model's reduced ability to harness the wind's energy results in less power being produced.

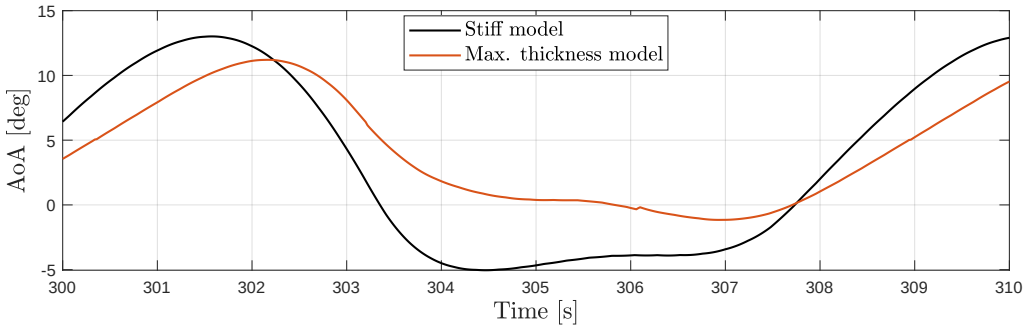

Figure 6.3: The angle of attack (AoA) as a function of the time for the stiff model and the maximum thickness model.

Now, the circular motion of the tip of the blade for both models can be seen in Figure 6.4. The azimuthal angles of one blade are taken by using the bearing angle. As previously mentioned, the flexible model deflects significantly while the stiff model shows no deflections over the rotation due to the high stiffness of the rotor. A total maximum deflection is found around w = 6.4 meters.

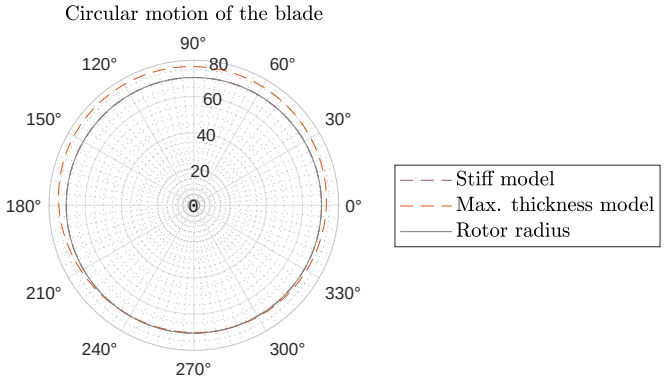

Figure 6.4: Circular motion of the tip of the blade for the stiff and flexible (max. thickness) models.

Thrust
Understanding a wind turbine's aerodynamic performance and power output requires an understanding of its thrust. The power generation is influenced by the aerodynamic forces operating on the blade, which are directly connected to the thrust. Figure 6.5 shows the thrust coefficient (C_T) over time. Due to its rigid construction and lack of flexibility, the stiff model displays no thrust. The aerodynamic forces operating on the turbine do not produce any thrust if the blades are not deflected or bent. This outcome is thus consistent with the properties of a stiff model. Nevertheless, the flexible model shows low but mostly positive thrust. Though somewhat less significant than in a stiff type, the capacity of the blades to bend and deflect helps to generate thrust. These variations in thrust between the stiff and flexible models highlight the impact of structural parameters on aerodynamic performance and underline the significance of taking flexibility into account when developing wind turbine designs.

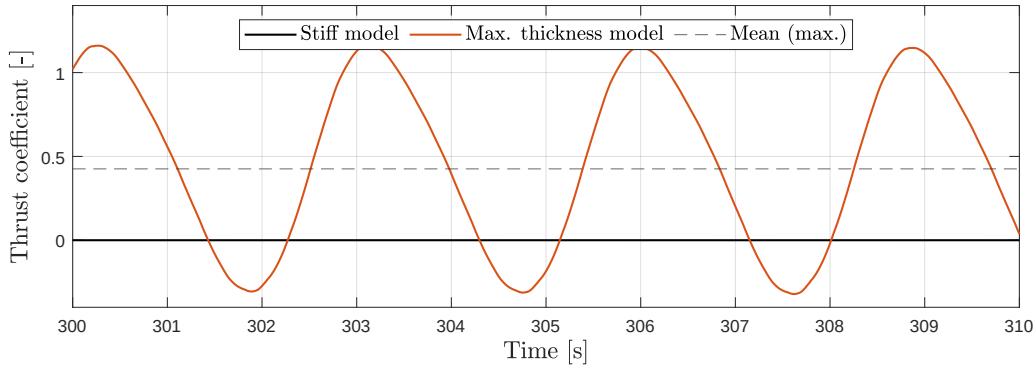

Figure 6.5: The aerodynamic thrust coefficient (C_T) as a function of time for the stiff model and the maximum thickness model.

Thrust and power coefficient

The thrust coefficient (C_T) shows how much force the wind is applying to the rotor, which is a vital factor in determining how much the wind turbine is being loaded aerodynamically. The thrust coefficient can be calculated with Equation 2.19. The power coefficient (C_p) measures how effectively a wind turbine converts wind energy into mechanical power. The power coefficient can be calculated with Equation 2.17, when the power and the turbine's geometry properties are known. Table 6.4 provides an overview of the thrust and power coefficients of the reference model and the maximum thickness model (flexible). The reference model does only give an equivalent power capacity, and from this, the power coefficient is derived. The difference in power output is minimal. There is no available information about the thrust nor the thrust coefficient coming from his report. The mean thrust coefficient (C_T) is also written down.

Table 6.4: Comparison between the mean power, power coefficient, thrust, and thrust coefficient of the reference model and the maximum thickness model.

Parameter	Symbol	Unit	Reference model	Max. thickness model
Power (mean)	P	MW	9	8.69
Power coefficient	C_p	-	0.43	0.41
Thrust coefficient	C_T	-	-	0.43

6.4.2. Aerodynamic loads

For a number of reasons, it is critical to examine aerodynamic loads, including variables like lift coefficient (C_l), drag coefficient (C_d), and angle of attack (α). First off, these variables shed light on the wind turbine's efficiency and performance in terms of aerodynamics. By examining the lift and drag coefficient, it can be assessed how well the turbine produces lift and reduces drag, maximizing its capacity to produce electricity. Figure 6.6 shows the angle of attack, instantaneous lift coefficient, and drag coefficient at the bottom of the blade over one rotation, as a function of the bearing azimuthal angle.

The angle of attack (AoA) varies over one azimuthal revolution, impacting the turbine's performance. The fluctuating relative velocities of the blade and the incoming wind cause the angle of attack to vary continually as the blade spins around the vertical axis. The angle of attack experienced by the blades at various azimuthal points throughout a full rotation affects the aerodynamic forces operating on the blades.

Therefore, analyzing the angle of attack distribution during the course of the rotation enables a thorough evaluation of the turbine's effectiveness and performance. As can be seen in Figure 6.6, it is possible to pinpoint the ideal angle of attack ranges and where the blades along its rotation produce the most lift while producing the least amount of drag.

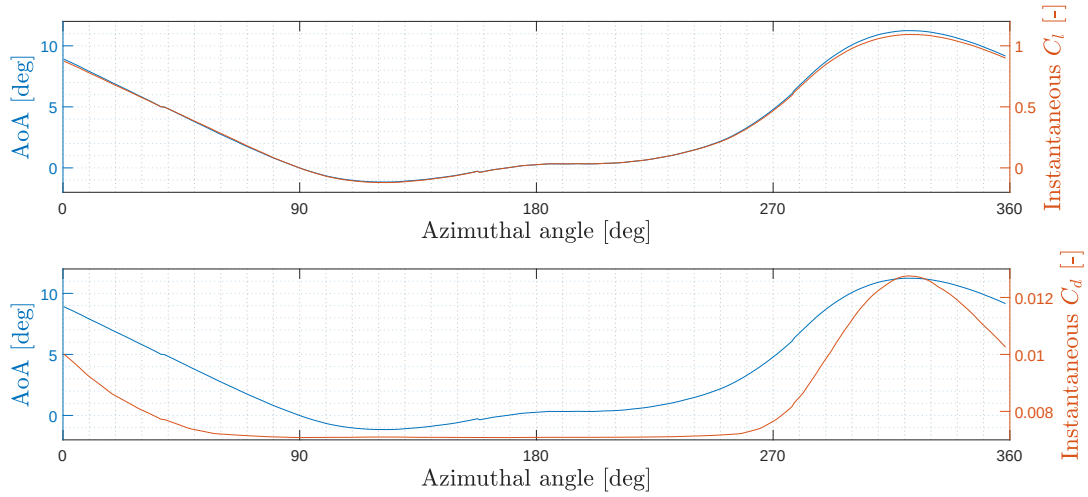

Figure 6.6: The angle of attack (AoA) is plotted as a function of the azimuthal angle (over one rotation) together with the instantaneous lift coefficient (C_l) and the instantaneous drag coefficient (C_d).

Angle of attack as a function of the TSR

From Figure 6.7, it can be seen that the angle of attack (AoA) range changes as the tip speed ratio (TSR, λ) varies. The angle of attack is taken at the bottom of the blade. A VAWT blade will encounter a continuously oscillating angle of attack as a result of the cycloidal design. A greater range of angle of attack can be achieved with lower tip speed ratios. As the tip speed ratio decreases, the blades rotate at a slower speed in relation to the incoming wind. Conversely, at higher TSRs, the blades rotate faster, leading to a narrower angle of attack range. As mentioned before, the angle of attack influences lift and drag generation and therefore the turbine performance. It is important to select the optimal TSR to ensure that the blades operate within the favorable angle of attack range. The favorable angle of attack range is connected to the polars of the airfoil, which can be seen in Appendix C. A range of AoA = $\pm$ 20 degrees minimized the drag coefficient while achieving high lift coefficients. Therefore, a TSR around 4 or slightly lower seems the most optimal value to reach higher aerodynamic performance (power output).

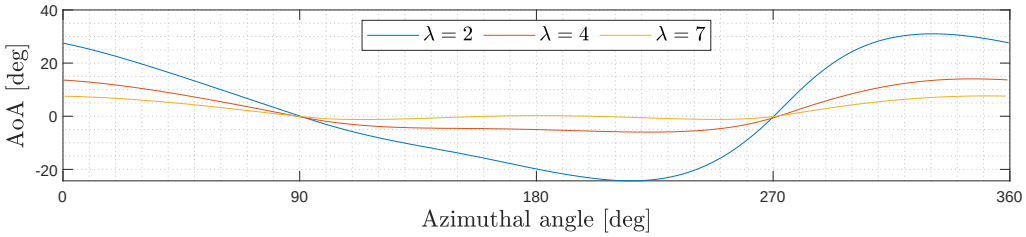

Figure 6.7: The angle of attack (AoA) for different tip speed ratios (λ) as a function of the azimuthal angle over one rotation (for the stiff model).

The angle of attack range will be substantially outside the stall limitations for a specific Reynolds number and airfoil section for low tip speed ratios [107]. Depending on the airfoil profile, Reynolds number, and solidity, a high angle of attack can generate a dynamic stall cycle with each blade rotation and maybe complete separation for portions of the azimuth. The VAWT design can be optimized based on the relationship between the TSRs and AoA, ultimately improving the aerodynamic performance and power generation.

6.4.3. Mass

The masses of the wind turbine models are the same in both the stiff model and the flexible model; the stiffness parameters (the stiffness matrix) are the sole difference. The results of these models can still be contrasted with the reference model on which they were built. It is crucial to remember that the findings will not line up precisely because of the wide range of laminate thicknesses provided by the reference model. It is possible that variations in power output, structural behavior, and other examined characteristics will result from variations in laminate thickness.

The masses of several parts (blade, strut, tower, and base) for the reference model and the maximum thickness model are contrasted in Table 6.5. It should be noted that the mass is per one amount of the total and not the total mass (so one blade, one strut). The findings show variation in component masses, which can be explained by the reference model not explicitly stating which laminate thicknesses are used. The highest option within the provided range was chosen for the maximum thickness model, which leads to an anticipated increase in mass when compared to the reference model. It surpasses the mass of the reference model. In addition, the reference model lacked a tower and base, although the model in HAWC2 does. Therefore, it is impossible to compare these components.

Table 6.5: Mass comparison of different components between the reference model and the maximum thickness model.

Parameter	Symbol	Unit	#	Reference model	Max. thickness model
Blade mass	m_B	kg	1	24,875	34,796
Strut mass	m_S	kg	1	4,146	11,037
Tower mass	m_T	kg	1	-	497,715
Base mass	m_B	kg	1	-	66,060

6.4.4. Natural frequencies

Natural frequencies of a VAWT design are one of the main critical failure modes. Therefore, examining the natural frequencies of the design is highly important. The natural frequency is the frequency at which a body will vibrate if it is activated by an outside source [108]. The natural frequency of a body varies depending on its mass and stiffness. The body needs to be aroused in order to vibrate. The dynamic behavior, stability, and potential resonance problems can be evaluated. The risk of excessive vibrations or structural failures can be reduced by optimizing the designs, ensuring that the turbine works within acceptable operational limits, and taking into account the natural frequencies. The natural frequencies of the blade, strut, and total structure are elaborated in this subsection.

Even though the design is not in its final stages and, therefore the natural frequencies of the components can vary later on, they should be taken into account for now as they can influence the simulation results. The blade design is most likely to be realistic, and so is the tower, but the strut design is not considered yet. It is most likely that the strut design shall be adjusted to have a more aerodynamic profile.

Strut

Firstly, the natural frequencies of the struts used in the reference wind turbine design are examined. The undamped natural frequencies (f_n) of the strut are written down in Table 6.6. It can be seen that the first mode lies far from the operational range (see: Table 6.2). The desired operational condition is at the design tip speed ratio. To reach this design speed, the rotational speed is adjusted for every wind speed. Therefore, the rotational speed will always be lower than the found rotational velocity at design TSR. For higher wind speeds, either rotational speed can be kept constant or the tip speed ratio and rotational velocity can decrease.

Table 6.6: Undamped natural frequencies (f_n) of the strut.

Mode nr.	Undamped natural frequency f_n [rad/s]
1	2.59
2	3.71
3	25.43
4	31.40
5	59.11

Blade

From Table 6.7, the natural frequencies of the blade (maximum thickness model) are shown. It can be seen that the first mode comes close to the rotation speed of the turbine at the current operating conditions (V = 12 m/s, λ = 4.5). This can lead to critical failures, as the wind turbine can deviate easily from its operational rotational speed. It must be confirmed that the wind turbine is not operated in a manner where

the 1P and 3P frequencies for three-bladed turbines are closer than $\pm$ 10% to the turbine's first natural frequency in order to prevent increased dynamic loads and resonance.

Table 6.7: Undamped natural frequencies (f_n) of the blade for the maximum thickness model.

Mode nr.	**Undamped natural frequency** f_n [rad/s]
1	0.74
2	1.17
3	4.63
4	7.31
5	12.94
6	19.61

Tower
Moreover, Table 6.8 provides the natural frequencies of the tower (undamped). It can be seen that the natural eigenfrequencies of the tower are higher than the operational range, meaning that they seem not to give any issues to the wind turbine design.

Table 6.8: Undamped natural frequencies (f_n) of the tower.

Mode nr.	**Undamped natural frequency** f_n [rad/s]
1	3.60
2	3.60
3	18.94
4	18.94
5	63.40
6	63.95

Total structure
Ultimately, the natural frequencies of the whole rotor structure are referred to in Table 6.9. The natural frequencies come close to the design tip speed ratio of TSR $=$ 4.5. As Table 6.9 shows the undamped natural frequencies, damping has though been added to the HAWC2 model. The damping is tuned so that the logarithmic decrement for the structure is lower than 3% for the first ten modes.

Table 6.9: Undamped natural frequencies (f_n) of the whole rotor structure for the maximum thickness model.

Mode nr.	**Undamped natural frequency** f_n [rad/s]
1	0.88
2	0.90
3	0.90
4	0.97
5	0.98
6	0.98

Reference model
The report of Schelbergen [5] provides a Campbell diagram for the H-rotor VAWT. The relation between the eigenfrequencies and the rotational speed of the rotor is illustrated in the Campbell diagram of Figure 6.8. The dashed lines represent harmonic lines corresponding to the rotation frequency. At points where the harmonic lines intersect with the eigenfrequencies of the modes, resonance can occur. It is believed that the harmonic lines of 5P and higher do not induce resonance due to their insufficient energy content. The eigenmodes of the struts (SM) intersect with the 2P line near the design speed of the rotor, indicating resonance at rated wind speed. Note that these identifications are the undamped, free-vibration modes. As the structural model is different than the reference model, the models cannot be compared properly.

Schelbergen [5] only mentions a range of laminate thickness while never specifying the actual used thickness in the end. Different thicknesses can lead to significantly different masses and varying stiffness properties.

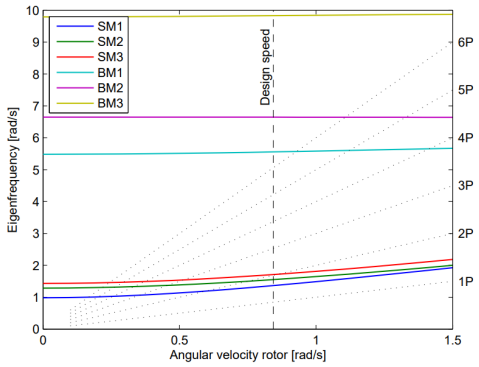

Figure 6.8: Campbell diagram of the H-rotor presented by Schelbergen [5].

6.4.5. Discussion

Based on the obtained results, it can be discussed if the model with the maximum thickness of laminates in the blade should be considered. It can be observed that the specific laminate thickness under investigation does not yield the desired or accurate solution. Relying on the results of that model can lead to incorrect or unreliable answers. This suggests the need for further investigation into alternative laminate thicknesses. In the next Section 6.5, two different models with other laminate thicknesses will be explored if they give a more steady power-TSR curve.

6.5. Laminate thickness of the blade

This section examines two other wind turbine models with different laminate thicknesses in the blade (V1 and V2). Differences between the models can be read in Table 5.7. Various parameters are studied. Power output, natural frequencies, masses, blade behavior, and aerodynamic loads are among the parameters that are examined. Not only the most optimum laminate thickness blade model is aimed to be found, but also the effects of different laminate thicknesses are investigated. This section aims to learn more about how laminate thickness affects power production, structural response, and aerodynamic performance.

6.5.1. Mass

The blade is the main factor that distinguishes the two models (V1 and V2) with varying laminate thicknesses when comparing them in terms of mass. This can be seen in Table 6.10. Both models have the same struts, which are more than double that of the reference model. The blade of the V1 model is significantly lower (around 10,000 kg), while the V2 model comes closest to the mass of the reference model.

Table 6.10: Mass comparison of different components between the reference model and V1 and V2 models.

Parameter	Symbol	Unit	#	Reference model	V1	V2
Blade mass	m_B	kg	1	24,875	14,524	22,512
Strut mass	m_S	kg	1	4,146	11,037	11,037
Tower mass	m_T	kg	1	-	497,715	497,715
Base mass	m_B	kg	1	-	66,060	66,060

6.5.2. Power output

This subsection focuses on comparing the V1 and V2 models in terms of power output. Due to the distinctive behavior seen in the earlier research of the maximum thickness model, the analysis of power output is essential. These models' power output can be evaluated in order to learn more about their performance characteristics and the possible effects of changing design parameters (the laminate thickness in the blade). This analysis aids in a better understanding of the variables affecting energy production and offers helpful recommendations for enhancing the design and operational parameters of the turbine.

Power vs. tip speed ratio
Figure 6.9 shows the power output for the V1, V2, and the whole stiff model as a function of the tip speed ratio (TSR). The power outputs for the V1 model exhibit good performance, maintaining steady power generation until TSR = 5. After this point, the V1 model deteriorates due to structural instability and sensitivity. On the other hand, the V2 model shows a higher power output around the optimum tip speed ratio, but the power quickly drops afterward. This is not favorable. These differences in power production across various TSRs offer insight into the advantages and disadvantages of the two models. A deeper comprehension of the behavior of the two models is aided by additional study.

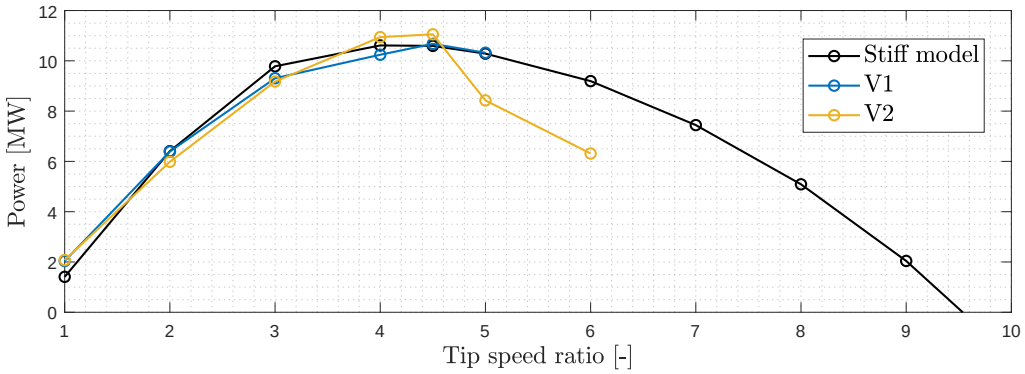

Figure 6.9: The power (P) as a function of the tip speed ratio (TSR), for both the stiff model as the V1 and V2 model.

Power over one rotation
In Figure 6.10, the aerodynamic power is plotted over the azimuthal angle (one rotation) for both models. This is done for a tip speed ratio of TSR = 4.5. As mentioned before, the V2 has a larger mean power output as it also displays a wider range of power values. In contrast, the V1 model shows a smaller range of power but seems to have steeper oscillations throughout the rotation.

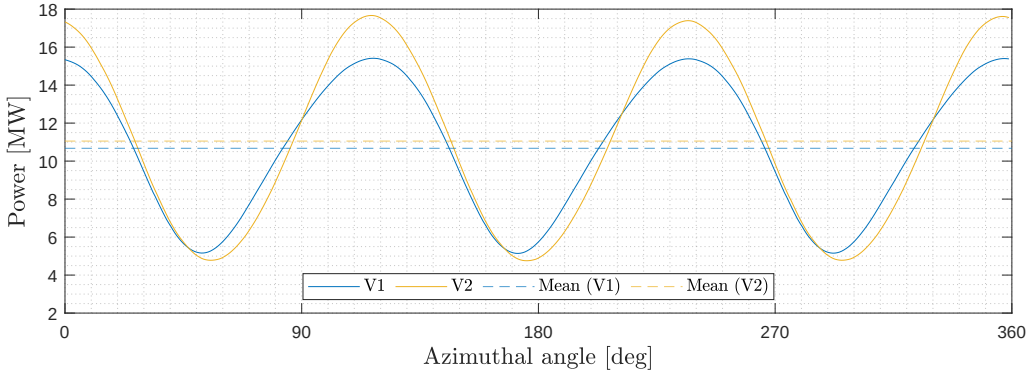

Figure 6.10: The power (P) as a function of the azimuthal angle for both the V1 and V2 model.

6.5.3. Natural frequencies
As mentioned before, the natural frequencies of the wind turbine design are critical. The models vary in the blade design and therefore the overall structure is impacted as well. Table 6.11 shows the undamped natural frequencies (f_n) of the blade and the whole structure for both the V1 and V2 model. It can be seen that the V2 model like the maximum thickness model has an eigenmode close (within 10%) to the operational rotational velocity of the rotor at the design tip speed ratio. This is not the case for the first eigenmode of the V1 model. Moreover, the structure's frequencies lay significantly higher than those of the maximum thickness model (Table 6.9). These higher natural frequencies are preferred over lower ones, as resonance is then less likely during operation.

Table 6.11: Undamped natural frequencies (f_n) of the blade and the whole structure for the V1 and V2 model.

	Undamped natural frequency f_n [rad/s]			
	V1		**V2**	
Mode nr.	**Blade**	**Structure**	**Blade**	**Structure**
1	0.55	1.27	0.74	1.07
2	1.35	1.30	1.19	1.10
3	3.47	1.30	4.61	1.10
4	8.42	1.30	7.45	1.18
5	9.73	1.40	12.89	1.19
6	16.74	1.40	19.79	1.19

6.5.4. Aerodynamic loads

The aerodynamic loads that the design is subjected to are analyzed in this subsection. The lift coefficient (C_l) and the drag coefficient (C_d) are plotted together with the angle of attack (AoA) over one rotation. It should be noted that the azimuthal angle is taken from the bearing angle for one specific blade. The aerodynamic parameters are taken from the bottom of the blade. The complex interaction between the turbine blades and the incoming wind flow is studied by examining these parameters. The orientation of the blade can be understood in terms of how it impacts the lift and drag forces. Additionally, the study of the lift and drag coefficient can provide important knowledge of the performance of the turbine in producing lift and reducing drag. Figure 6.11 shows the angle of attack (AoA) together with the lift coefficient (C_l) and the drag coefficient (C_d). It can be seen that the angle of attack and lift coefficient both follow each other well, while the models vary from each other. The V1 model reaches a lower angle of attack around an azimuthal angle of θ = 260 degrees, while the V2 model has a smoother angle of attack and obtains a higher maximum. The drag coefficient does not follow the same angle of attack pattern, while their maximums can be found together with the angle of attack maximums. The drag coefficient is very small.

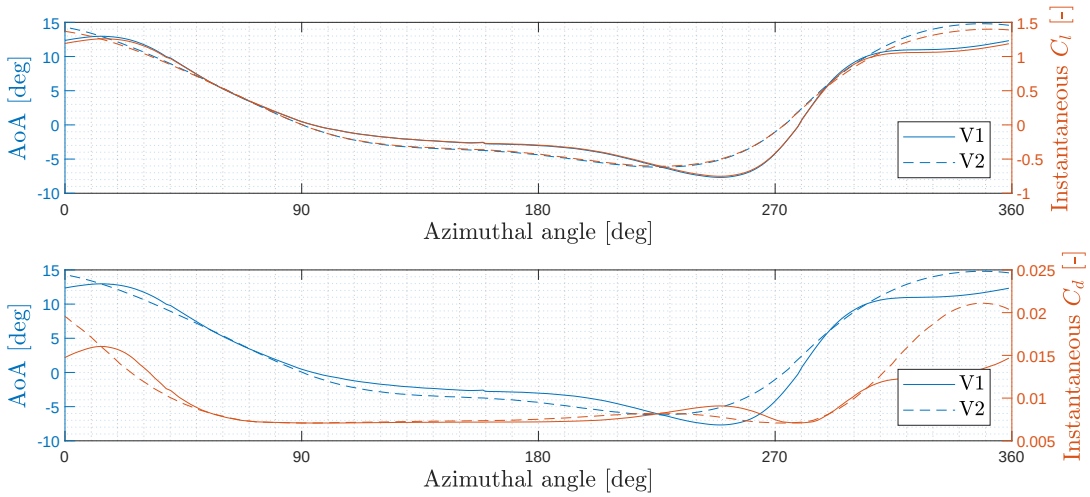

Figure 6.11: The angle of attack (AoA) over one rotation plotted with the instantaneous lift coefficient (C_l) and the instantaneous drag coefficient (C_d) for the V1 and V2 model.

6.5.5. Blade behavior

This section thoroughly discusses the results related to the behavior of the blade. The focus lies on the deflection and torsion. The purpose of this part is to provide insight into the blades' dynamic response of the two models. Furthermore, the structural integrity of the designs and the reaction to aerodynamic forces can be assessed.

Deflection

Table 6.12 provides the total possible maximum deflection the blade can experience along its length for both models. It can be seen that the tip deflects the most, followed by the bottom part of the blade. When

comparing the two models, the V1 model exhibits greater deflection along the blade's length. For HAWTs, a limit of blade deflection can be taken as 5% of the blade length [109]. If this would be applied to the reference model, the limit of deflection can be set to 7 meters. However, the VAWT design is different, as the blade is connected with struts at two points. As the limit based on the blade length is quite high, and while there is no limit found in the literature, an acceptable deflection is taken with the rotor radius. 5% of the rotor radius gives an acceptable deflection of 3.5 meters. It can be seen that the V1 model exceeds this at the tip.

Table 6.12: Total possible maximum deflection along the blade of the V1 and V2 models.

Parameter	Symbol	Unit	V1	V2
Max. deflection bottom of blade	w_b	m	1.55	0.59
Max. deflection position of bottom strut	w_{bs}	m	0.96	0.47
Max. deflection middle of blade	w_m	m	0.90	0.68
Max. deflection position of upper strut	w_{us}	m	0.93	0.91
Max. deflection position of tip	w_t	m	4.77	3.22

The circular motion of the blade at the tip of both models is visible in Figure 6.12. As the tip of the blade has the highest maximum deflection, only the tip will be illustrated. The other plots can be found in Appendix F. It can be seen that the V1 has over the whole rotation higher deflection (moving from the rotor radius).

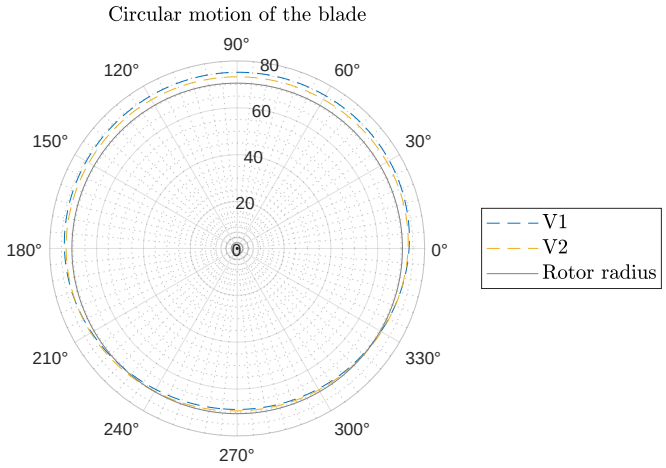

Figure 6.12: Circular motion of the tip of the blade for the V1 and V2 models.

In addition, Figure 6.13 illustrates the movement of the blade in the z-direction. It can be seen that both modes move up similarly, but the V1 model deflects more down with a meter difference between the two models. It should be noted that the bearing angle of the turbine is used to represent the azimuthal angle for one particular blade. As the blade deflects significantly up and down, it is most likely that the struts are not stiff enough and deflect under these operating conditions. Increasing the stiffness could help maintain a more stable rotor, while the struts would less deform.

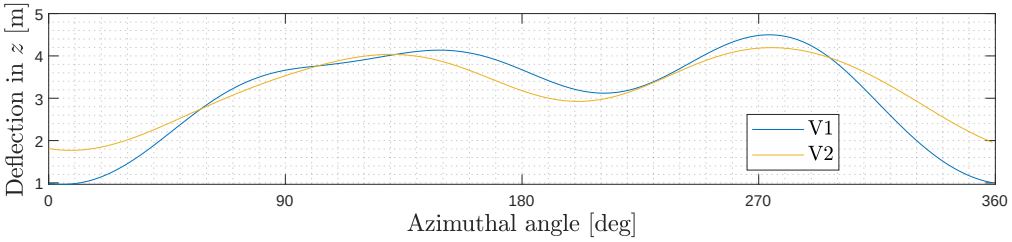

Figure 6.13: The deflection in the z-direction for the V1 and V2 model over one rotation.

Torsion
The elastic deformation (R_z) of the bottom part of the blade over one rotation is shown in Figure 6.14. It can be seen that the torsion in the V1 model varies more over the rotation, while the V2 model has a more steady elastic deformation.

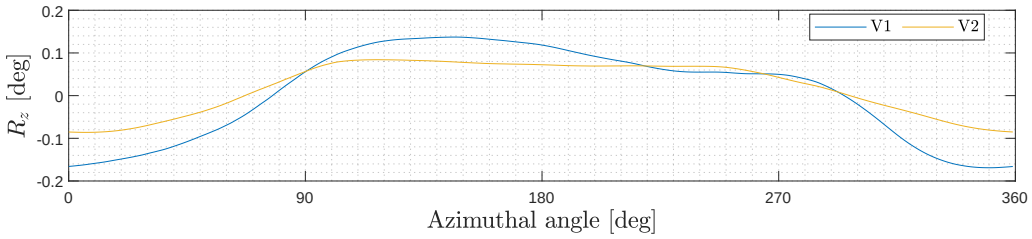

Figure 6.14: The elastic deformation (R_z) at the bottom of the blade over one rotation for the V1 and V2 model.

At the tip of the blade, the elastic deformation is significantly increased. This can be seen in Figure 6.15. This lines up with the deflection of the blade, as the tip of the blade experiences much higher deflections than the bottom part.

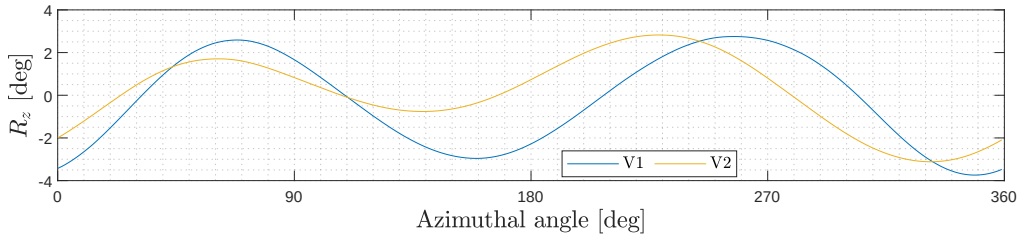

Figure 6.15: The elastic deformation (R_z) at the bottom of the blade over one rotation for the V1 and V2 model.

Figure 6.16 shows different screenshots taken of the V1 model over its rotation. The screenshots are from the animation file made by HAWC2. It can be seen that the tip rotates more and deflects more than the bottom part of the blade, explaining the torsional deformation results presented before.

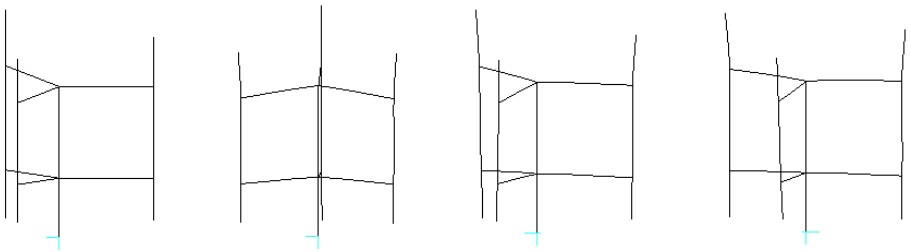

Figure 6.16: Screenshots taken of the V1 model over its simulation from the Animation data file, obtained from HAWC2.

6.5.6. Optimum tip speed ratio

The best tip speed ratio can be adjusted toward TSR $= 4$ according to the examination of the results, specifically the power vs. tip speed ratio plot and the natural frequencies. According to this conclusion, operating at this tip speed ratio may result in better performance and the highest power output. The system is also closer to its failure threshold with a higher tip speed ratio, thus, there may be a trade-off between improved performance and increased risk of failure of the WT. The power drops quickly after $\lambda = 4.5$, which makes it a tricky choice. It can be expected that the wind turbine reaches, without aiming for it, quickly a slightly higher tip speed ratio.

6.5.7. Optimum laminate thickness

Based on the obtained results, there are several reasons to consider choosing a model with smaller laminate thicknesses, like the V1 or V2 model. The V1 model has a lower mass than the other models, which not only translates to lower expenses but also suggests a lightweight design. It would satisfy the objective to lower the mass over the swept area the most. Additionally, the V1 model shows a good overall performance in terms of power generation. The power output for this model does not show any notable drop at a certain tip speed ratio, showing consistent performance. The maximum thickness model seems to give incorrect and unexpected values during the analysis, and therefore, it is better not to continue working with this model. Moreover, as the V2 model has the first eigenmode of the blade relatively closer to the optimal rotational velocity (within 10%), the V1 model can be preferred over the V2 model. However, the V1 model seems to have less structural stability in the design as the V1 has larger deflections of the blade. Therefore, this should be kept in mind.

6.5.8. Verification

The results can be compared to those of the reference model. This phase can be named verification. A direct comparison was however constrained, as the reference model offered a broad range of laminate thicknesses as opposed to a specific thickness. For this reason, the structural models will never be totally equal to one another. It is clear that the results differ from the reference model greatly. These disparities can be caused by a number of things, which will be described in the discussion in Chapter 8. However, the model functions and shall be used further with the chosen optimum thickness.

Side-to-side comparison

The angle of attack over one rotation for the V1 model can be seen in Figure 6.17. The azimuthal degree is adjusted to match that of the reference model. Figure 6.18 shows the angle of attack as a function of the blade azimuth of the reference model. The V1 model, in contrast to the reference model, has smoother variations in the angle of attack. This can be related to the chosen time step of the simulations in HAWC2. With a smaller time step, the model might capture the same fluctuations at the negative angle of attacks during one rotation. The V1 model and reference model behave similarly in terms of angle of attack (AoA), showing that the HAWC2 simulations successfully captured the general anticipated aerodynamic characteristics. The main difference can be named the trough of the V1 model around $\theta = 150^{\circ}$. It can be seen that the V1 model in HAWC2 reaches a higher maximum and it stays longer around a higher angle of attack. It should be mentioned that the reference model uses a different airfoil profile, which is optimized. Moreover, the angle of attack comes not from a simulation, but from Carlos Simão Ferreira [5]. Blade-wake contact happens throughout the windward, downwind, and leeward portions of the blade rotation, according to Simao Ferreira's research [80]. The angle of attack at these rotating sections fluctuates as a result of this interaction. As the torsion and the deflection differ along the blade, so does the angle of attack over the blade, so at different points on the blade, the angle of attack can differ.

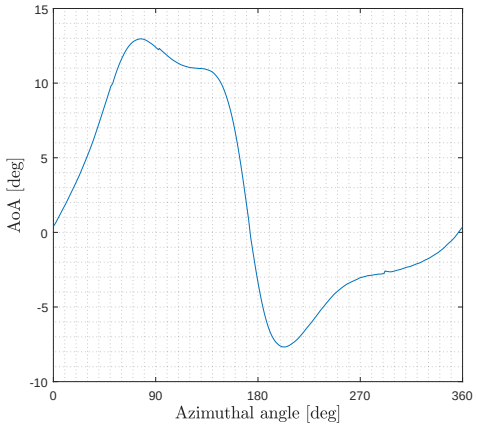

Figure 6.17: The angle of attack over one rotation (moved to match the reference model) for Blade 1 of the V1 model.

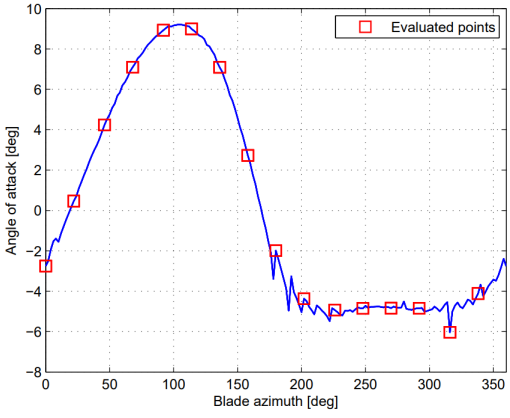

Figure 6.18: The angle of attack as a function of the azimuthal blade positions, taken from the reference model [5].

Other parameters cannot be compared well, which will also be discussed in Chapter 8.

6.6. Dynamic stall model

Dynamic stall is one of the unsteady aerodynamics phenomena and it impacts the performance and behavior of VAWTs. For this reason, it is important to simulate different dynamic stall methods in order to comprehend how dynamic stall affects VAWTs. VAWTs are pertinent to the concept of dynamic stall, due to their cyclic fluctuation in the angle of attack over one rotation. The lift and drag are therefore influences, and so does the power generation of the turbine. If no dynamic stall method is applied, an important factor that influences the behavior and performance of VAWTs will be missed.

Prior comparisons were conducted using the Øye dynamic stall model. However, this section adds another dynamic stall model, so that two models can be compared: Øye and Beddoes-Leishman (B-L). With the use of these two different dynamic stall models, the performance and behavior of the V1 model will be evaluated and contrasted in this comparative analysis.

6.6.1. Simulation model

The dynamic stall is investigated with the V1 model based on prior research. The model has proven to have advantageous qualities. Furthermore, operating conditions can be kept at either TSR = 4 or TSR = 4.5. The V1 model has shown good aerodynamic behavior with the Øye model.

6.6.2. Power output

Foremost, it is essential to consider looking at the power output when comparing the two dynamic stall models. The power output is a performance indicator. It can be evaluated how well each dynamic stall model captures wind energy and maximizes the power output. Secondly, the dynamic stall models directly affect the lift and drag forces generated by the turbine blades. The aerodynamic loads will be discussed in Section 6.6.3. The power output variations reveal changes in the effectiveness of lift creation and drag reduction.

Power over time

The power output over time for the two dynamic stall models is shown in Figure 6.19. The Øye model demonstrates a substantially greater range of power variations. As a result, the Øye model has a higher mean than the B-L model. In contrast, the B-L model has lower peaks and minima, resulting in lower mean power. These varying results point out that there are significant differences between the two dynamic stall models. These results show how important choosing the right dynamic stall model is.

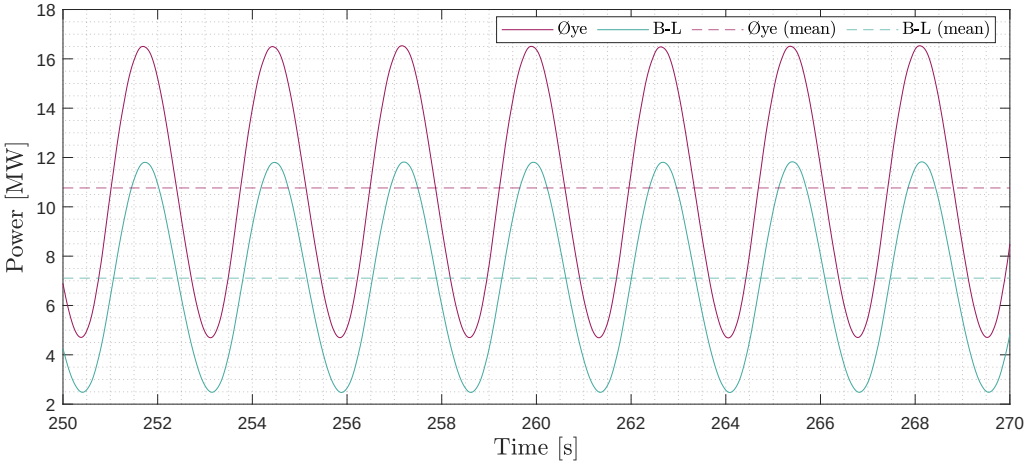

Figure 6.19: The power (P) as a function of the time for the Øye and Beddoes-Leishman dynamic stall models and their means.

6.6.3. Aerodynamic loads

Figure 6.20 illustrates the angle of attack (AoA) and the instantaneous lift coefficient (C_l) over one rotation. It should be recalled that the azimuthal angle of one specific blade is represented by the bearing angle of the rotor. The aerodynamic parameters are taken from the bottom of the blade. Both dynamic stall models show an identical graph for the angle of attack, only varying after θ = 270 degrees. From this point, the Beddoes-Leishman model simulates a lower angle of attack. Moreover, the B-L model provides a smaller

range of the lift coefficient than Øye's dynamic stall model. This shows that the B-L model might produce less lift, which could explain the lower power output.

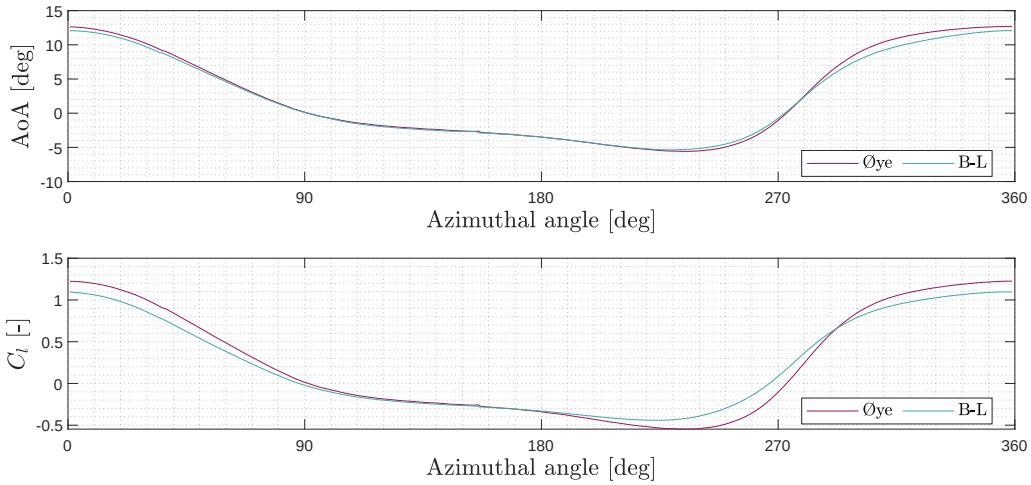

Figure 6.20: The angle of attack (AoA) and the instantaneous lift coefficient (C_l) as a function of the azimuthal angle, simulated for different dynamic stall models (Øye and Beddoes-Leishma).

The fluctuations of the drag coefficient (C_d) and the relative velocity (V_{rel}) for one rotation for the two dynamic stall models are shown in Figure 6.21. Again, the aerodynamic parameters are taken from the bottom of the blade. The relative velocity is almost identical between the two models, except at around θ = 270 degrees. Here, the B-L model experiences a larger relative velocity compared to Øye's model. Over the rest of the rotation, the relative velocity is lower than Øye's model. Nevertheless, total differences can be found for the instantaneous drag coefficient. The drag coefficient is the most important distinction found. In comparison to Øye's model, the B-L model has significantly greater drag coefficients. This would suggest more aerodynamic resistance, which can lead to decreased overall performance and power. These findings highlight the crucial part that the dynamic stall models play in affecting the drag forces generated by the turbine blades. Øye's model can reproduce the stall dynamics on the lift coefficients but has no dynamics in attached flow, nor on the drag and moment coefficients [110]. This is what is observed here as well. The aerodynamics can better be solved using Hansen's Beddoes-Leishmann model, which reproduces both attached flow and stall dynamics.

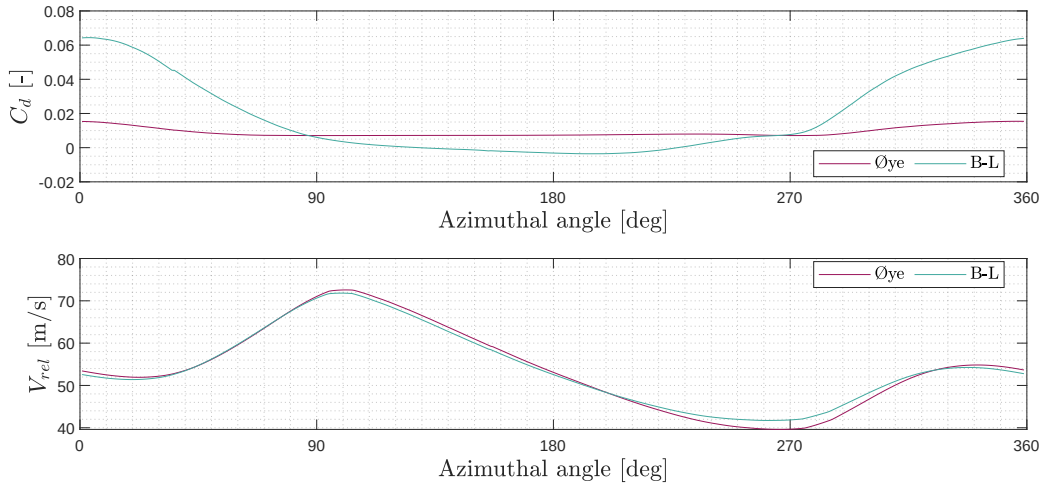

Figure 6.21: The instantaneous drag coefficient (C_d) and the relative velocity (V_{rel}) as a function of the azimuthal degree, simulated for different dynamic stall models (Øye and Beddoes-Leishman).

6.6.4. Discussion

The two dynamic stall methods, Beddoes-Leishman and Øye, provide different results. These differences can be ascribed to how the two models calculate the drag and lift coefficient in different ways. Øye's model

can reproduce stall dynamics on the lift coefficients but not on the drag or moment coefficients. Although the Beddoes-Leishman model is widely seen to be more accurate, it is noteworthy that when compared to the reference model, its power output is substantially less than expected. Based on these findings, additional research on the dynamic stall models implemented in HAWC2 is suggested.

6.7. Placement of struts

One of the main variables impacting the wind turbine's aerodynamic performance is the strut [111]. The strut is a crucial support structure that connects the vertical axis wind turbine blade to the rotating shaft and it transfers torque. Therefore, the first design driver of the VAWT that will be looked into is related to the strut. It is the placement of the struts in relation to the length of the blade (x_{strut}/H, or shortened to x/H). Figure 5.9 shows the position of the strut, while the blade is presented as a beam. In this context, the struts are all assumed to be installed symmetrically to the midpoint of the blade.

6.7.1. Literature observations

The work of Miao et al. [111] discusses the placement of the struts at the end span (tips) of the blade. When the struts are placed at the end, they lead to greater aerodynamic efficiency, according to the findings of Marsh et al. [112] and Villeneuve et al. [113]. The struts do not interrupt the high-performance area of the blade surface and they help to reduce tip losses. However, both the aerodynamic performance and the required structural support, which is even more crucial for large-scale VAWTs, should be taken into account [111]. The maximum stresses for the blade with struts at their ends were roughly five times higher than those with quarter-span struts [49][50]. The structural and aerodynamic performance is more balanced when the struts are placed at a quarter.

Table 6.13: Placement of struts, previously found and done in the literature.

	Reference model	Wind turbine of Huisman	Literature
x_{strut}/H	0.25	0.27	0.29

In other research, the struts are also placed around a quarter. In the work of Fiedler et al. [114], the struts are placed at 25% and 75% span locations. While the works of Hameed et al. [50] and Ahmadi-Baloutaki et al. [49] found the optimum placement to reduce bending stresses of the two struts at 21% and 79%. Table 6.13 provides three different placements of the struts. Schelbergen [5] found his optimal placement at $x_{\text{strut}}/H = 0.25$, while the wind turbine model of Huisman chose initially for $x_{\text{strut}}/H = 0.27$.

6.7.2. Beam deflection constraint

Initially, the optimum placement of the two struts can be found with beam deflection calculations. A beam will represent the blade, which will be held at two positions. To find the optimum placement, the following constraint can be set:

- The deflection in the middle of the blade $x = 0$ should be the same as the tip deflection of both sides.

The Euler-Bernoulli beam theory can be used to resolve this problem.

Distributed load

Only the centrifugal forces are considered, which is given in Equation 6.1. The mass (m) is defined as the blade mass per meter. Therefore, the centrifugal force is also given as force per meter.

$$q_c = q = m\omega^2 R \tag{6.1}$$

The beam is therefore thought to be carrying a distributed load.

Deflection

The deflection ($w(x)$) can be expressed as a function of the position on the beam, with $x = 0$ the midpoint. The expression is given in Equation 6.2, in which q is the distributed load, E is the elastic modulus of the material, and I is the moment of inertia of the cross-section. The position of the strut is defined as $x_{\text{strut}} = b$. The constants C_1 and C_2 can be found with the boundary conditions.

$$w\left(x\right) = \left(\frac{q}{24EI}\right)\left(x^2 - b^2\right)^2 + C_1 x + C_2 \tag{6.2}$$

Boundary conditions
The boundary conditions are defined below:

- The deflection at $x = 0$ should be equal to the deflection at the ends: $w(0) = w(L/2) = w(-L/2)$;
- The slope at $x = 0$ is zero: $w'(0) = 0$;
- The beam is fixed at $x = b$ and $x = -b$, and there is no deflection here: $w(-b) = w(b) = 0$.

Solving the problem
The slope of the beam is found by differentiating the deflection $w(x)$ to x.

$$w'(x) = (\frac{q}{6EI}) \cdot x \cdot (x^2 - b^2) + C_1 \tag{6.3}$$

The second boundary condition leads to $w'(0) = C_1 = 0$. The first boundary condition and the third can be used to find b:

$$b = x_{strut} = L/(2 \cdot \sqrt{2}) = 0.35 \ldots L \tag{6.4}$$

Assumptions
For this calculation, several assumptions are made [115][116]:

- The cross-section is uniform over the beam;
- The distributed load (centrifugal force) is constant;
- The deflection and rotation of the beam are small ('small deflection' assumption);
- The material of the beam is linearly elastic and follows Hooke's law (the deflection will become inaccurate for plastic deformations);
- The shape and geometry of the cross-sections in the beam are not significantly altered when transverse loads are applied (the cross-section can be treated as a rigid surface that can only rotate);
- The cross-sections in the beam remain plane and parallel to its deformed axis through deformation;
- The strut is described as fixed points. Therefore, at these points, there are no deflections (vertical and horizontal deflections are assumed to be zero), no rotation and no axial deflection (no change in length due to axial forces).

Discussion
It is essential to remember that these assumptions are not always strictly valid for real-life beams. This makes the Euler-Bernoulli beam theory an idealization that may not be applicable in this scenario. However, it can still give a good indication sometimes. More intricate beam theories, like the Timoshenko beam theory in HAWC2, can be required instead to predict the behavior of beams more accurately.

6.7.3. Models

The different placement of the struts can be simulated in HAWC2. Based on previously found positions of the struts, the range where the optimum strut can lay is $0.2 < x_{\text{strut}}/H < 0.36$. The chosen placements to investigate with HAWC2 lay in this region: $x_{\text{strut}}/H = 0.2, 0.23, 0.25, 0.27, 0.29, 0.33, 0.35$. Note that for each option, the mass and area of the rotor stay the same, as the strut is only moved up or down. In Figure 6.22, four of these models can be seen (from the animation output file of HAWC2). The tower of all models is kept the same height (the height of the original model, x/H = 0.25) and the upper strut is placed at the top of the tower. Enough space is kept below the blade so that it does not hit or interfere with the ground.

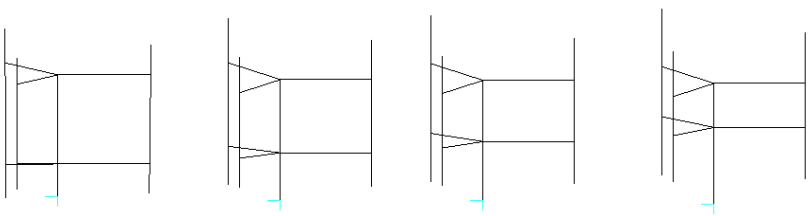

Figure 6.22: Four models with different placement of the struts in HAWC2. From left to right: x_{strut}/H = 0.20, 0.25, 0.29 and 0.35.

6.7.4. Power output

From the simulations in HAWC2, the power output can be obtained. The mean power output (P) is plotted as a function of the strut position x_{strut}/H in Figure 6.23 with the MHH B-L dynamic stall model respectively. From these results, it can be seen that the model produces the most power how higher the strut is placed. If the struts are placed above x_{strut}/H = 0.29, the power decreases again. However, the power varies only within $\approx$ 6%. This means that the power output is not influenced significantly by the placement of the struts.

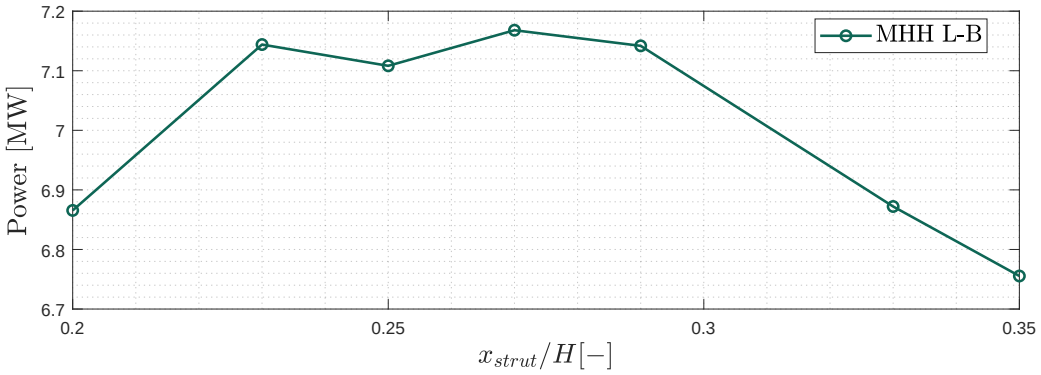

Figure 6.23: The power (P) as a function of the strut position (x_{strut}/H), with the MHH B-L model applied for the dynamic stall.

6.7.5. Blade behavior

This section looks into the blade behavior of all models, including the deflection, torsion, and angle of attack (AoA). The structural impact of the different placement of the struts is assessed on these parameters. The analysis of the blade deflection offers insight into the flexibility and integrity of the blades when struts are placed differently. The ideal placement of the struts can be suggested based on the different blade behaviors, allowing for improved turbine design and higher overall performance.

Maximum total deflection

The greatest total deflection of the blade for the various rotors is displayed in Figure 6.24. Three points are chosen, which are the tip, middle, and bottom of the blade. The blade tip shows the greatest maximum deflection over all models. Both the tip and the bottom reach almost 10 meters of deflection for a strut placement of x_{strut}/H = 0.35. Comparatively less deflection is experienced near the middle of the blade, which suggests greater stability and resistance to deformation due to the placement of the struts. This is expected because the middle part is more likely to experience less strain and stress than the tip and bottom sections. The bottom section, however, demonstrates higher deflection when the struts are placed closer to the middle of the blade.

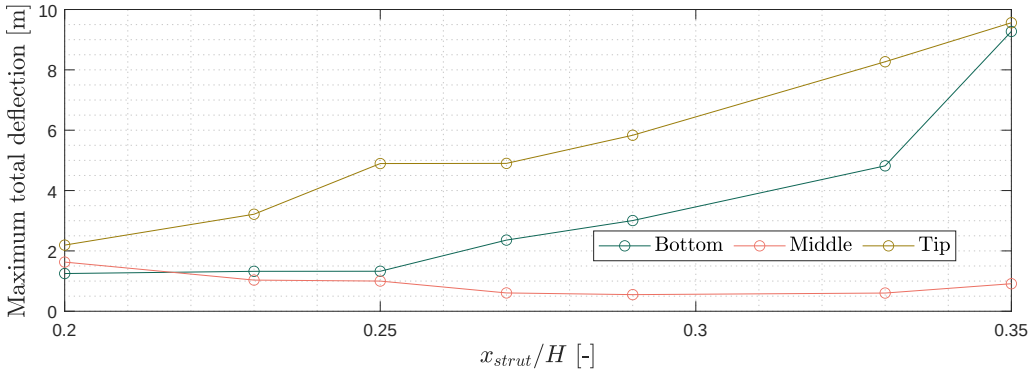

Figure 6.24: The maximum total deflection of the blade at the tip, middle, and bottom for rotors with different placements of the strut (x_{strut}/H).

It should be noted that these findings differ from the average deflection over one rotation, as the total maximum deflection is found with polar coordinates, as described in Appendix E.

Discussion
When taking into account how the strut placement affects the deflection behavior of the blade, an optimal placement of the struts can be suggested. The ideal strut placement is found within the range of $x/H =$ 0.2 to $x/H = 0.27$ based on the results from the maximum total deflection. The deflection is reduced in this range in all three points of the blade. By reducing the deflection, the structural integrity of the blade is improved. This would assure the longevity and dependability of the wind turbine design.

Angle of attack
The behavior of the rotors can be investigated with the angle of attack (AoA) over time, shown in Figure 6.25. This is from the bottom of the blade. It can be seen that all positions show similar behavior, which does not vary much over time and seems to be stable. The exception is $x_{\text{strut}}/H = 0.33$ and 0.35, which varies from the other rotors.

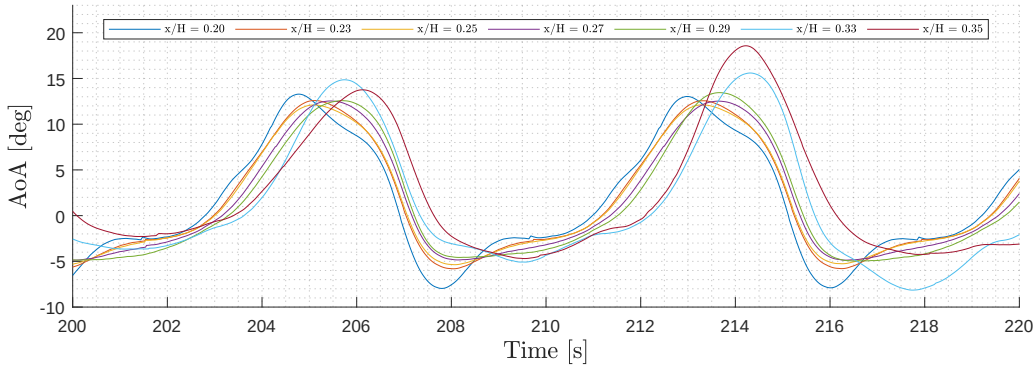

Figure 6.25: The angle of attack (AoA) as a function of time for rotors with different placements of the strut (x_{strut}/H).

Torsion
Figure 6.26 shows the torsion (M_z) at the bottom of the blade as a function of time for all different positions of the struts (x_{strut}/H). The torsion is in the local axis of the blade. Local is around the local beam's main bending directions. It can be seen that when the struts are placed toward the middle of the blade, these moments become higher. High peaks can be observed, which is not favorable.

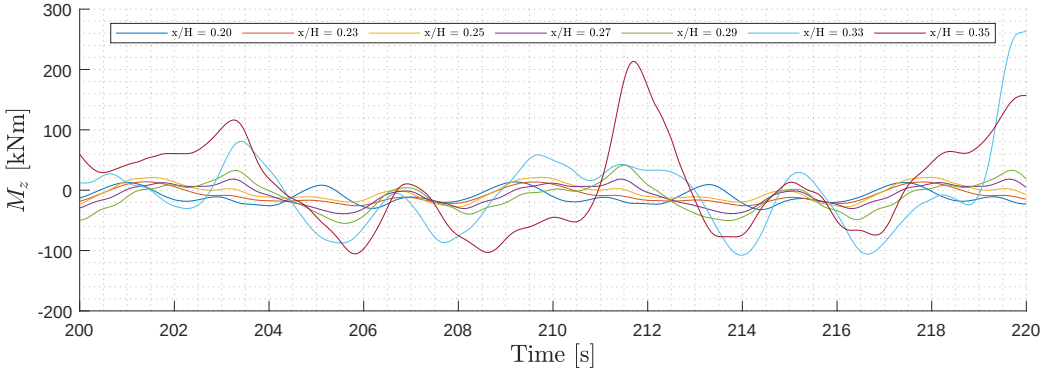

Figure 6.26: Torsion (M_z) at the bottom of the blade as a function of time for rotors with different placements of the strut (x_{strut}/H).

6.7.6. Conclusion
In conclusion, it has been established that the ideal placement of the struts can be found around $x_{\text{strut}}/H =$ 0.23 to 0.27. This placement brings several benefits. First, this placement brings higher power output, even though it is not significantly increasing. In addition, it has been shown that the maximum deflections around this placement are comparatively modest compared to the other strut placement. This suggests that there is a well-maintained balance between the performance and structural stability of these models, in comparison with other strut placements. Moreover, the found results in HAWC2 contrast with the result of the beam deflection calculation.

Due to the project's timetable, additional investigation has been done with the original strut placement. The original strut placement is found within the optimal range.

6.8. Additional diagonal strut

The main objective of this section is the comparison between the standard H-rotor design and a modified H-rotor design that incorporates an additional diagonal strut. It is examined how the additional diagonal strut affects the turbine's behavior and performance. To evaluate the design, key parameters such as the power output and aerodynamic loads are examined in depth again. Moreover, the comparison aims to assess the potential advantages and disadvantages of this additional strut.

6.8.1. Literature observations

Most of the H-rotors in literature have no more than two struts per blade. However, it is more likely to have the struts installed at an angle, in addition to the usual horizontal configuration. Huisman made their original design with an extra strut while placing all struts under an angle. The benefit of adopting inclined struts for a straight-bladed VAWT is that the tower height and the center of gravity of the rotor can be decreased [111].

Two struts configuration

De Marco et al. [117] proposed a combined horizontal and inclined VAWT strut. Their numerical simulations and experimental results showed that the inclined part could capture additional wind energy and compensate for its own drag [111]. The non-vertical connection of the inclined strut to the blade will provide a bending moment. Therefore, a horizontal strut for large-scale VAWTs is suggested by Hand et al. [48]. However, there is not much research about how inclined struts affect aerodynamic performance [111]. Aihara et al. [118] modeled a VAWT with inclined struts with mounting angles of $\pm$ 17.6°. Villeneuve et al. [113] also investigated different incline angles of the struts (10°,22.5°,45°). It should be noted that in this case the struts were connected to the ends of the blade.

Specific configuration

Even though no literature observations are found for the specific configuration of a rotor with three struts, the model is still investigated and compared to the original rotor with two horizontal struts. The operating conditions, described in Section 6.1, are used again as well. Furthermore, the two horizontal struts are placed at their original position and not the found optimal placement.

6.8.2. Modified design

In Figure 6.27, the HAWC2 model can be seen for the modified model with the additional strut. The strut is placed under a 45° angle between the lower strut and the tower. The strut design is exactly the same as the two horizontal struts, but the length of the additional strut is increased due to its diagonal placement.

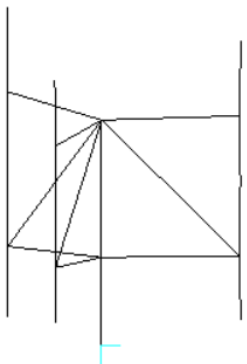

Figure 6.27: The new rotor design in HAWC2: The rotor has three struts per blade, with the additional diagonal strut being placed under an angle of 45°.

6.8.3. Power output

Figure 6.28 illustrates the aerodynamic power output of the two models (original and modified with the additional diagonal strut) over time. It can be seen that the models provide almost an identical mean power

output, while the range of the original model is slightly smaller. This can be related to small variations in the angle of attack, which will be investigated shortly.

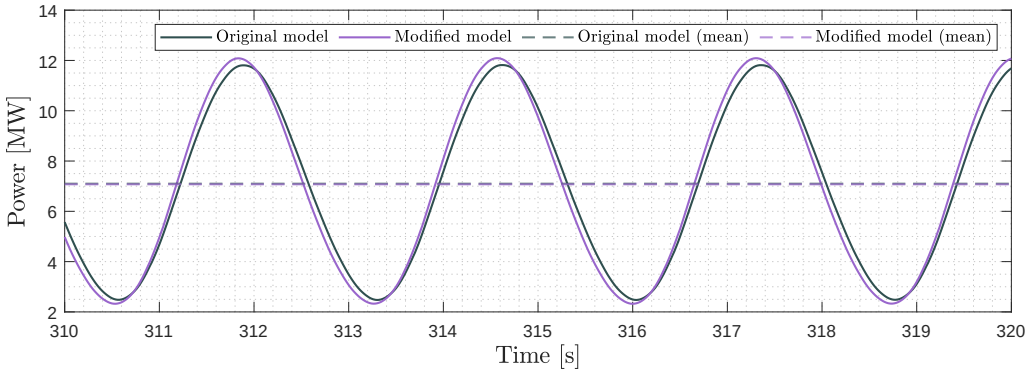

Figure 6.28: The power (P) as a function of time for the original model and the modified model with the additional diagonal strut.

6.8.4. Aerodynamic loads

Figure 6.29 shows the angle of attack (AoA) and the lift coefficient (C_l) for the original and modified models over one rotation. It should be remembered that the azimuthal angle of a single blade is expressed by the bearing angle of the rotor. These aerodynamic data are gathered from the bottom of the blade. For both models, the angle of attack and lift coefficient show a strong correlation. The original model operates more smoothly, which can be seen in the angle of attack and subsequently the lift coefficient. Moreover, it can be observed that the modified model has a clear peak around $\theta = 180$ degrees, followed by a fall. These differences can be the reason for a larger range of power output while keeping the same mean power. Furthermore, the findings demonstrate that the structural adjustment in adding a diagonal strut influences the aerodynamic behavior of the wind turbine.

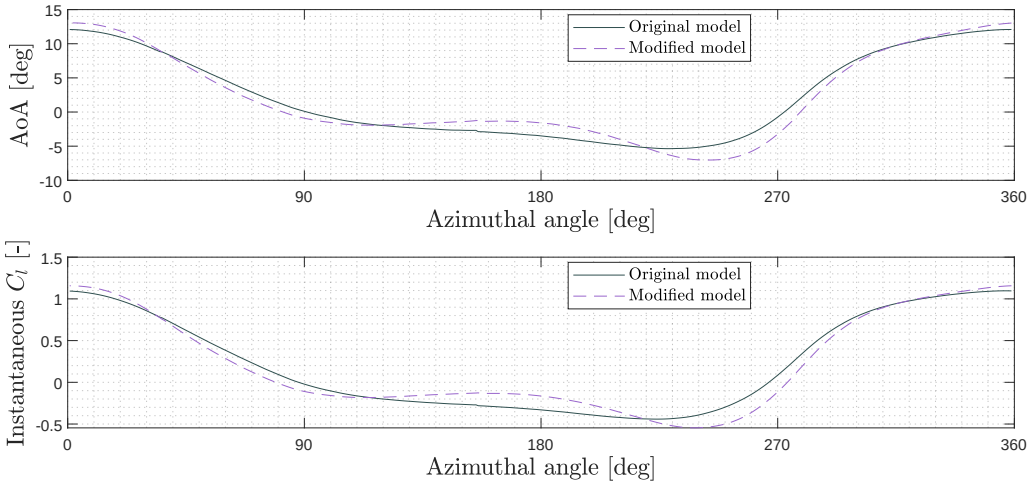

Figure 6.29: The angle of attack (AoA) and the instantaneous lift coefficient (C_l) over one rotation for the original model and the modified model with the additional diagonal strut.

As can be seen in Figure 6.30, the modified model and the original model have a similar course of the instantaneous drag coefficient (C_d) over one rotation. One observation can be made that the modified model reaches a higher drag coefficient. Moreover, the relative velocity of the blade (V_{rel}) fluctuates more over one rotation for the modified model, reaching higher peaks and lower falls.

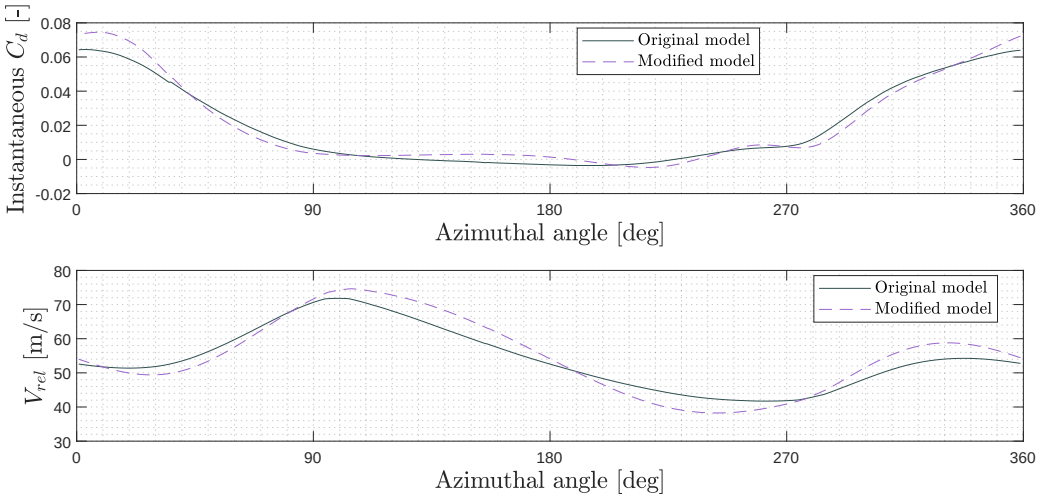

Figure 6.30: The instantaneous drag coefficient (C_d) and the relative velocity of the blade (V_{rel}) over one rotation for the original model and the modified model with the additional diagonal strut.

6.8.5. Blade behavior

In this subsection, the analysis of the blade behavior for both models is explored. It aims to investigate the influences of the additional diagonal strut on the blade and its structural response. The maximum blade deflection at different positions is first compared, while the torsion is also examined afterward.

Deflection

The circular motion of the blade at the tip is shown in Figure 6.31. Both the original model and the modified model are illustrated. First of all, it should be noted that the findings of the original model (V1) vary with Section 6.5 due to the implementation of another dynamic stall model. It can be seen that the modified model comes closer to the perfect circle (the rotor radius) in most parts of the rotation.

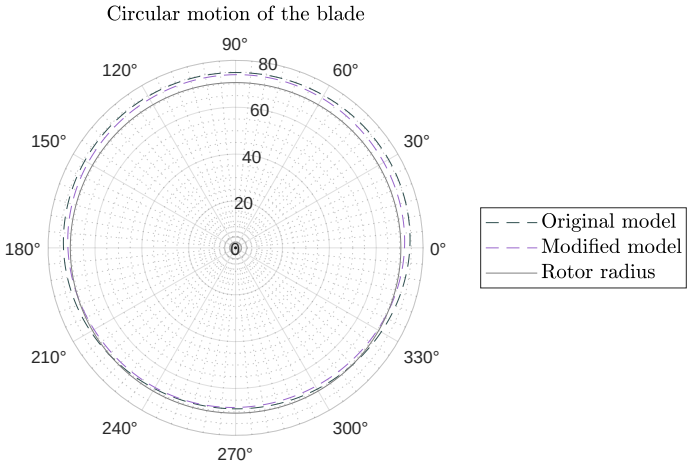

Figure 6.31: Circular motion at the top of the blade for the original model and the modified model with the additional diagonal strut.

The maximum deflections are written down in Table 6.14. It can be seen that the modified model with an additional diagonal strut experiences a lower maximum deflection over the blade. It should be noted that this is a piece of a snapshot of the whole rotation. As it can be seen in Figure 6.31, the deflection is the same over every azimuthal angle.

Table 6.14: The total possible maximum deflections along the blade of the original model and the modified model with an additional diagonal strut.

Parameter	Symbol	Unit	Original model	Modified model
Max. deflection bottom of blade	w_b	m	1.37	0.66
Max. deflection position of bottom strut	w_{bs}	m	0.42	0.35
Max. deflection middle of blade	w_m	m	1.00	0.98
Max. deflection position of upper strut	w_{us}	m	0.92	0.75
Max. deflection position of tip	w_t	m	4.88	3.45

As it can be seen in Figure 6.32, the deflection of the blade in the z-direction is very different for the original model compared to the modified model. The blade deflects significantly less in the z-direction when an additional diagonal strut is placed. The original model is never in its original placement. It should be recalled that the azimuthal angle is given by the bearing angle for a single blade.

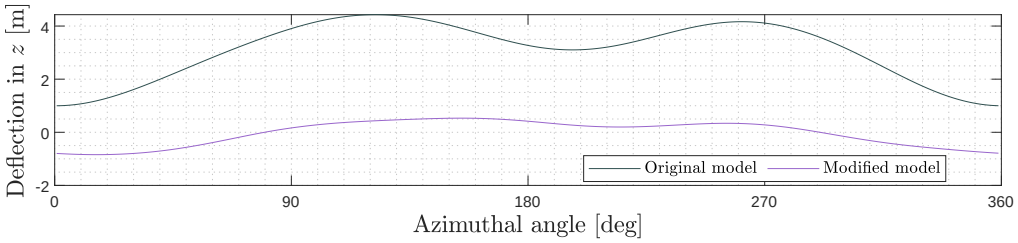

Figure 6.32: The deflection of the blade in the z-direction of the original model and the modified model with the additional diagonal strut.

Torsion

Figure 6.33 illustrates the elastic rotation (R_z) at the bottom part of the blade for the original model and the modified model with the additional diagonal strut. It can be seen that the elastic rotation of the modified model is around 90 and 270 degrees slightly larger than the original model.

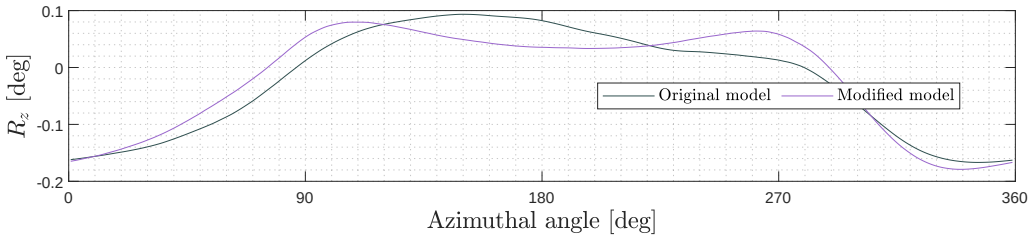

Figure 6.33: The elastic rotation (R_z) at the bottom of the blade over one rotation for the original model and the modified model with the additional diagonal strut.

Moreover, it can be seen in Figure 6.34 that the elastic rotation (R_z) becomes larger compared to the bottom of the blade. However, no extreme variations can be seen as in Figure 6.33.

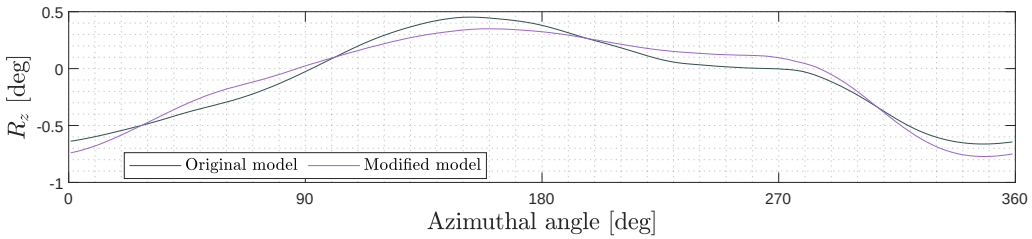

Figure 6.34: The elastic rotation (R_z) at the strut placement on the blade over one rotation for the original model and the modified model with the additional diagonal strut.

Figure 6.35 illustrates different screenshots which are taken from the animation software. It shows the modified model with the additional diagonal strut at four-time snaps over its rotation. It can be seen that the deflection is at the tip higher, while also the blade rotates around its axis.

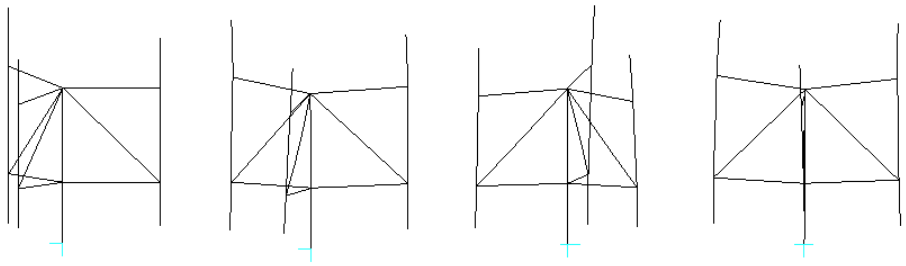

Figure 6.35: Screenshots taken of the modified model with the additional diagonal strut over its simulation from the animation data file, obtained from HAWC2.

6.8.6. Natural frequencies

As the designs of the blade and the strut remain identical, their natural frequencies do not differ from the original rotor design. The only changes can be seen in the natural frequencies of the total structure, which are written down in Table 6.15. The modified model with the additional diagonal strut exhibits larger natural frequencies than the original model. This suggests that the modified model has enhanced structural rigidity and increased stiffness. The higher natural frequencies can improve the stability of the wind turbine design.

Table 6.15: The undamped natural frequencies (f_n) of the whole structure are compared for the original model and the modified model.

Mode nr.	Undamped natural frequency f_n [rad/s]	
	Original model	Modified model
1	1.27	1.31
2	1.30	1.37
3	1.30	1.37
4	1.30	1.64
5	1.40	1.64
6	1.40	1.65

6.8.7. Conclusion

First, the modified model has some structural advantages that can be named. By adding the diagonal strut in the design, the natural frequencies of the structure increase positively out of operational range. As a result, this improves the stability of the turbine and the resilience during operation. Moreover, the blade experiences lower deflection except at the bottom section. A significant difference from the original model can be found in the deflection of the blade in the z-direction. When the diagonal strut is added to the design, the blade moves less up and down and stays more steady at its original placement.

However, the wider effects of adding an extra strut from a cost and optimization standpoint should be considered. The objective of the optimization of VAWT designs is to minimize the mass over the area, to reduce the costs, and to raise the power [6]. The modified model requires three extra struts (one for each blade), which raises the rotor's overall mass greatly. As a result, the crucial parameter for the objective is negatively impacted, leading to higher manufacturing and material costs. So even though the diagonal strut enhances some structural performance and stability of the turbine, the overall financial implications should be considered as well. The updated design must strike a balance between the enhanced structural properties and the corresponding increase in mass. Therefore, it is essential to conduct a thorough cost-benefit analysis, to see if the design options are economically viable as well.

6.9. Upscaling with the aspect ratio

This section focuses on the upscaling effects of the VAWT design. The aspect ratio is changed to achieve the upscaling, by varying the height of the blade while keeping the rotor radius constant. The following investigation provides important insight into the possible scalability of the design to maximize the power output.

6.9.1. Literature observations

The work of Brusca et al. [119] examines the design of a VAWT to maximize the power coefficient. The power coefficient increases as the Reynolds number of the blade does. The report shows that the rotor solidity (σ) and the Reynolds number (Re) have an impact on the power coefficient (C_p), based on calculations based on the Multiple Stream Tube Model. It was discovered that the aspect ratio (H/D) influences both the Reynolds number and the power coefficient. It was found that a lower aspect ratio brings a higher power coefficient, while there is also a structural advantage of having a thicker blade (less height and greater chord). Moreover, a greater inertia moment of the rotor can provide greater stability.

According to the work of Ahmadi-Baloutaki et al. [49], a rotor aspect ratio of between 0.5 and 2 is excellent from an aerodynamic standpoint, whereas a ratio of 1 results in the highest performance [46]. It would seem preferable to choose a low aspect ratio with a fixed VAWT swept area in order to maximize the chordal Reynolds number [49]. In fact, increasing the VAWT radius will permit the blade chord to increase and thus the chordal Reynolds number. However, with a low aspect ratio, blades will experience higher blade tip losses. The blade tip loss effects are the most significant. For this reason, a higher aspect ratio with longer blades is crucial to obtain. The theory of finite wings states that the blade tip vortices are caused by the pressure difference between the sides. Figure 6.36 displays the flow visualization by the smoke of an H-rotor blade tip vortex [80].

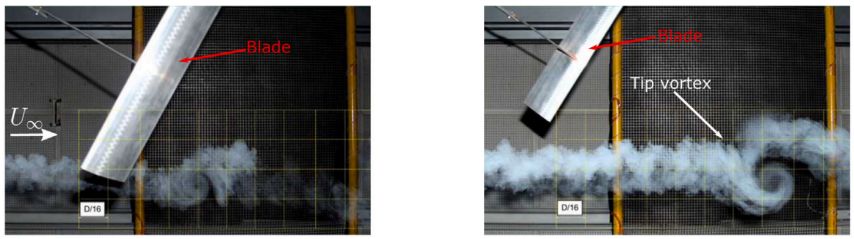

Figure 6.36: Flow visualization of the blade tip vortex of an H-rotor VAWT after interacting with a smoke streamline [49][80]. Left: before the streamline interaction, right: after the streamline interaction.

6.9.2. Models

In Table 6.16, an overview of the models which are used for the upscaling effects with the aspect ratio is provided. It can be seen that the rotor diameter (D) is kept constant over the simulations and only the blade length (H) is scaled up to obtain higher aspect ratios. This is done after researching the literature. Table 6.16 provides also the strut placement of each model, which is kept at x_{strut}/H = 0.25. It should be noted that the chord is kept constant over the models, to only look at the effect of increasing the aspect ratio with the blade length. Nevertheless, the tower height is increased with the rotor aspect ratio. It is done so that the blade does not touch the ground, and there are 10 meters taken for this. Therefore, no geometric scaling assumption is applied. The models are all taken to be flexible instead of stiff, to see the upscaling effects of the blade without changing the laminate thicknesses or struts.

Table 6.16: Comparison of geometry parameters between the models which are upscaled with the aspect ratio.

Model	**Aspect ratio** H/D [-]	H [m]	D [m]	x_{strut}/H [-]	**Tower height** [m]
1	1	141	141	0.25	115.75
2	1.25	176	141	0.25	142
3	1.5	247	141	0.25	169

6.9.3. Power output

Figure 6.37 provides the mean power of the three models. It can be seen that the mean power increases with the aspect ratio, demonstrating a positive correlation between the aspect ratio and the mean power

output. This can be explained by the fact that an increase in the blade length leads to a larger swept area. More lift shall be produced, translating into increased torque and power generation. This is as one would expect with a larger blade length. The lift coefficient will be analyzed in Section 6.9.6.

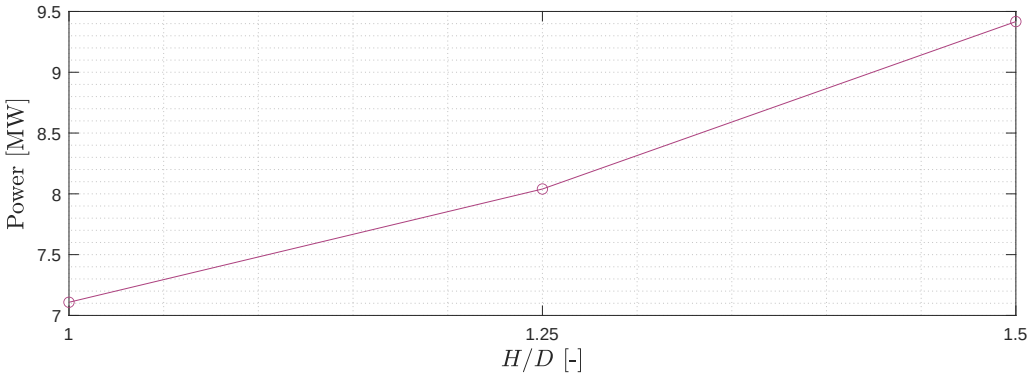

Figure 6.37: The mean power (P_{mean}) as a function of the aspect ratio (H/D).

6.9.4. Natural frequencies

As the strut and the rotor radius stay unchanged, the natural frequencies of the strut are kept the same in the three models. Therefore, only the natural frequencies of the blade and the overall structure are looked into. It can be seen in Table 6.17 that the natural frequencies decrease as the blade increases. Moreover, the natural frequencies of the structure also decrease. The first eigenmodes of the upscaled models are well without $\pm$ 10% of the rotational speed of the turbine.

Table 6.17: Comparison of the undamped natural frequencies (f_n) of the models with different aspect ratios and their components.

	Undamped natural frequency f_n [rad/s]					
	H/D = 1		H/D = 1.25		H/D = 1.5	
Mode nr.	**Blade**	**Structure**	**Blade**	**Structure**	**Blade**	**Structure**
1	0.55	1.27	0.36	1.14	0.25	0.96
2	1.35	1.30	0.87	1.14	0.60	0.96
3	3.47	1.30	2.23	1.14	1.54	1.01
4	8.42	1.39	5.42	1.21	3.75	1.10
5	9.73	1.40	6.26	1.22	4.32	1.10
6	16.74	1.40	12.29	1.22	8.50	1.10

6.9.5. Mass

In Table 6.18, a comparison between the masses of the blades can be seen. As the blade length is scaled linearly and the cross-section is constant over the whole length, the masses also scale linearly. The struts are kept the same, but the tower length will be increased so that the blades do not touch the ground.

Table 6.18: Mass comparison of the blades for different aspect ratios (H/D). The mass is of one blade for each model.

Parameter	**Symbol**	**Unit**	H/D = 1	H/D = 1.25	H/D = 1.5
Blade mass (1)	m_B	ton	14.52	18.13	21.84

6.9.6. Blade behavior

In this subsection, the blade deflection at the tip and the torsion are investigated shortly.

Blade deflection

Figure 6.38 shows the total circular motion of the blade's tip for models with different aspect ratios (H/D). Moreover, the rotor radius is plotted as well. As the investigations previously showed that the tip generates

the most deflection, only the tip is chosen to compare the models with different aspect ratios. The models with higher aspect ratios show considerably more deflection, as expected: the blades are much longer.

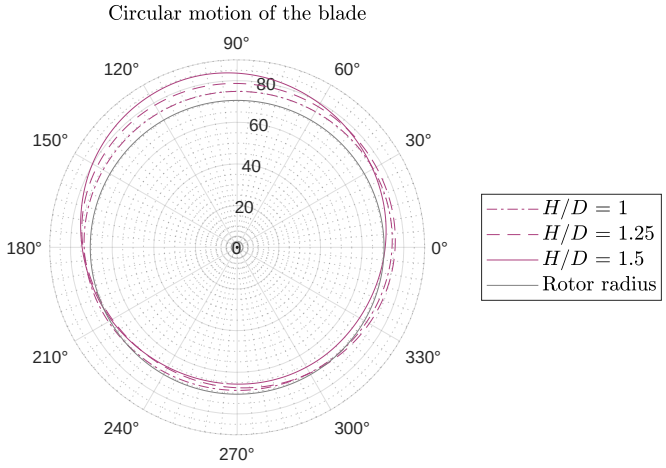

Figure 6.38: The rotation of the tip of the blade in the global coordinate system for different aspect ratios (H/D) compared to the rotor radius.

The maximum deflections of the tip of the blade are written down in Table 6.19. It can be seen that the deflection in the x-direction for all models lies within a range of 4 to 5 meters, while the maximum deflection in the y-direction increases with the aspect ratio. The y-direction is the wind direction, explaining why the deflection is the largest here.

Table 6.19: The found maximum deflections of the tip of the blade in the x- and y-direction for different aspect ratios (H/D).

Parameter	**Symbol**	**Unit**	H/D = 1	H/D = 1.25	H/D = 1.5
Max. deflection in x at top	$w_{t,x}$	m	3.92	5.39	4.6
Max. deflection in y at top	$w_{t,y}$	m	4.30	8.13	13.20

Moreover, the blade can move downwards in the z-direction. Figure 6.39 shows this for the different aspect ratios (H/D) over one rotation. It can be seen that the blade of the model with the highest aspect ratio (H/D = 1.5) moves the most up and down. An explanation can be described by the increase of the blade masses, while the struts and their cross-sectional parameters are unchanged.

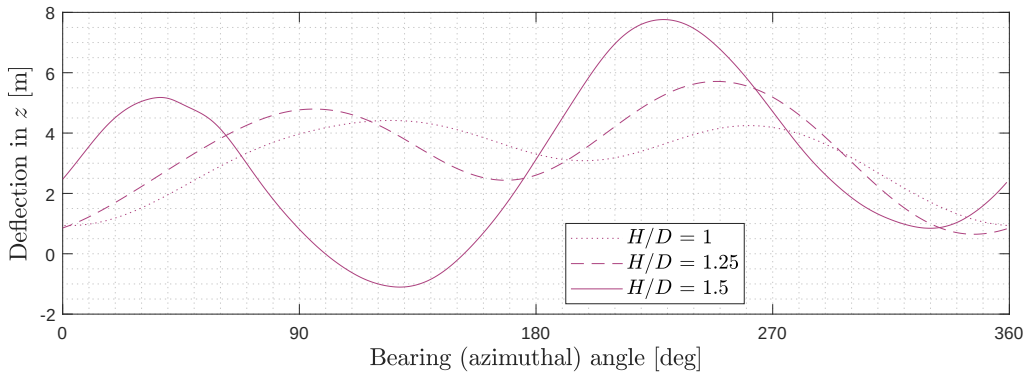

Figure 6.39: The deflection in z-direction for different aspect ratios (H/D) over one rotation.

Circular motion of blade

As it can be seen in Figure 6.39, the peaks of maximum deflection are reached at different positions of the bearing angle. This can be explained by the circular motion of the blade. The blade and strut may bend

as they rotate, changing the moment when the blade is at certain azimuthal angles. This is illustrated in Figure 6.40, without deflection of the blade. For this reason, the peaks of the models with different aspect ratios differ.

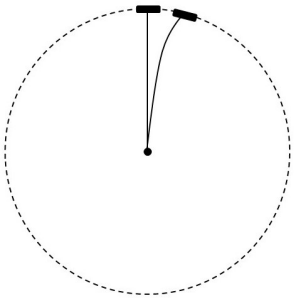

Figure 6.40: As the blade rotates, the blade and strut can deform so that the blade is later at certain azimuthal angles. The circulation is visualized without deflection of the blade.

Through a series of screenshots from the animation, Figure 6.41 shows the rotation of the rotor with an aspect ratio of H/D = 1.5. Firstly, it can be seen that both the strut and the blade show large deformations and deflections. These deformations lead to different motion patterns of the blade throughout one rotation. As a result, the blade's movement of the different models differs. Because of these deformations and dynamic behavior, graphing the position of the blade throughout a full rotation will not line up together when plotted with the bearing angle.

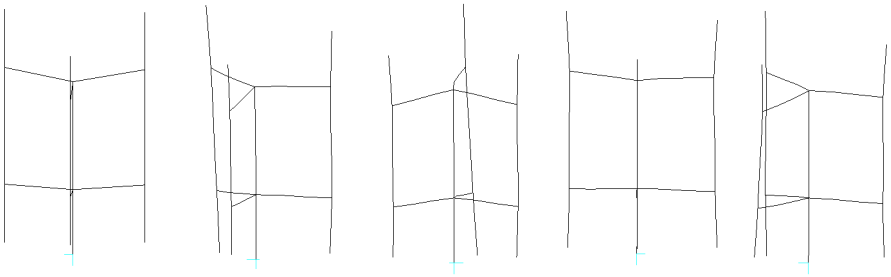

Figure 6.41: Screenshots taken of the model with H/D = 1.5 over its simulation from the animation data file, obtained from HAWC2.

Torsion

In Figure 6.42 and Figure 6.43, the elastic deformation (R_z) over one rotation is shown for the different aspect ratios (H/D) for the bottom part and the tip of the blade. The model with the largest aspect ratio also shows the largest degree of torsion over one rotation, which is consistent with the observation of the blade's deflection. This result is expected, since the models with larger aspect ratios have longer blades, making them more vulnerable to deflection and torsional effects brought by the wind conditions.

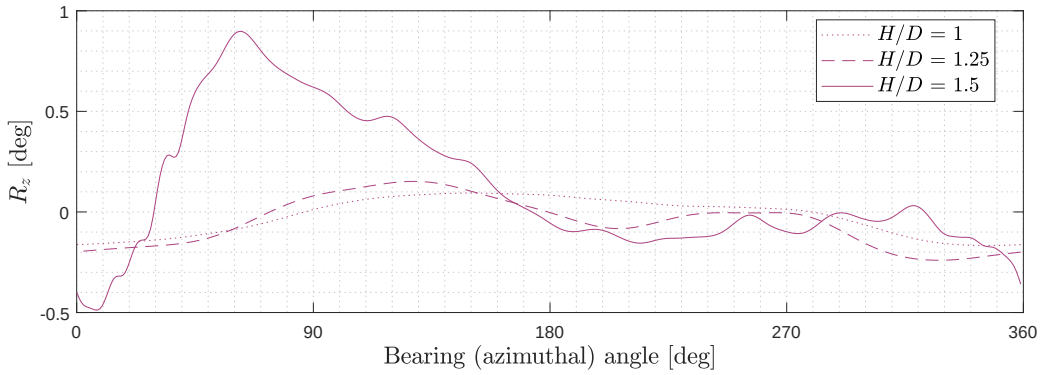

Figure 6.42: The elastic deformation (R_z) at the bottom of the blade over one rotation for models with different aspect ratios (H/D).

Moreover, looking at the elastic deformation at the tip of the blade reveals similar patterns. The elastic deformation over one rotation for the different models is illustrated in Figure 6.43. Though, noticeable larger magnitudes are found, which are also consistent with the larger tip deflections. The model with an aspect ratio of H/D = 1.5 shows significantly greater values, while also a change in the direction of elastic deformation can be seen. This emphasizes the aspect ratio's effect on structural behavior even further and shows how torsion sensitivity increases when the aspect ratio is increased.

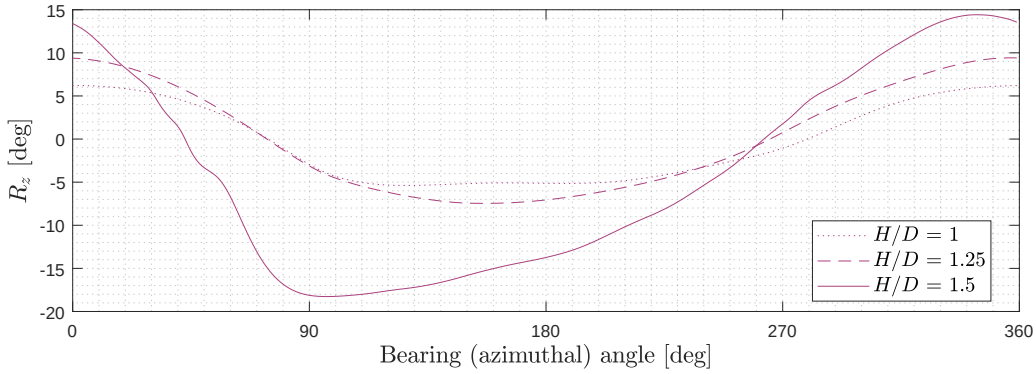

Figure 6.43: The elastic deformation (R_z) at the tip of the blade over one rotation for models with different aspect ratios (H/D).

6.9.7. Conclusion

The rotor can be upscaled with the aspect ratio. The aspect ratio is changed by increasing the blade length while keeping the rotor radius unchanged. The results show significant trade-offs between the power output and the structural behavior. The power output increases with the aspect ratio, as there is a greater blade surface area. However, the deflection of the blade increases as well, which could lead to structural issues. This necessitates further testing, to guarantee of the turbine can be used in the long term. Moreover, as the blades become longer with the aspect ratio, the mass will rise. As a result, the material costs will go up as well. To balance power generation efficiency and structural integrity, these factors should carefully be taken into account while designing VAWTs. Maintaining aeroelastic stability and avoiding resonance problems remain crucial when scaling up to higher power outputs. It is discovered that when the aspect ratio increases, the eigenfrequencies of the blade and the total structure also decrease.

7

Huisman design

This chapter delves into the design and the results of the company's simplified VAWT design. First, the baseline parameters are discussed that differ from the reference model. As the design has a different airfoil profile, the aerodynamic input is changed. This has a significant impact on the performance of the turbine. Moreover, the specified operational conditions are discussed, such as the rotational speed of the rotor. Subsequently, the results are presented, with an emphasis on the power output, other aerodynamic impacts, and blade behavior.

7.1. Baseline design and simplifications

Huisman originally designed a VAWT design that is shown in Figure 7.1. The VAWT is designed to be placed on a floating structure offshore, to harness powerful wind resources. The design uses a three-blade H-rotor layout, each supported by three struts, to create a reliable structure that can handle the dynamic forces present in offshore conditions. Moreover, the design has an expected power output of 10 MW, while potential scalability to higher power outputs is aimed for.

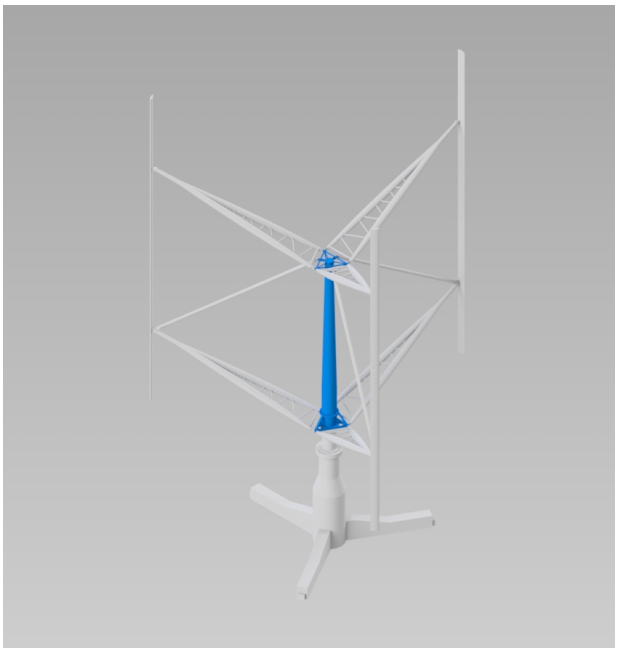

Figure 7.1: Original Huisman VAWT design.

7.2. Baseline parameters

This project simplifies the design to see the differences due to geometry changes. The tower for the reference model is based on the Huisman design, and therefore, this is unchanged. Moreover, as the strut design is not fixed yet, the same struts (design and cross-sectional parameters) are used. However, they are adjusted to a larger length due to the increased rotor radius. In Table 7.1, the baseline geometry parameters of the Huisman design are visible. It can be seen that the rotor radius is increased and so is

the blade height, but the chord length is smaller than the reference model. The Huisman model has also an aspect ratio of 1. Moreover, it should be noted that originally the blades of the Huisman model are most likely made of GFRP instead of CFRP. However, as only the aerodynamic effects of the resizing to the Huisman model are looked into, the possible change in material is not taken into account.

Table 7.1: Baseline values for the Huisman design.

Geometry parameter	Parameter	Unit	Value
Rotor radius	R	m	80
Blade height	H	m	160
Aspect ratio	H/D	-	1
Chord	c	m	4.0
Swept area	A_s	m^2	25,600
Solidity	σ	-	0.075
Twist angle	θ_t	deg	0
Number of blades	B	-	3

Table 7.2 provides the baseline values for the performance parameters of the Huisman VAWT design. The rated power is estimated higher than the reference model (10 vs. 9 MW). Moreover, the cut-in and cut-out wind speeds are provided.

Table 7.2: Baseline values for the performance parameters of the Huisman VAWT design.

Parameter	Symbol	Unit	Value
Rated power	P_{rated}	MW	10
Cut-in wind speed	V_{cut-in}	m/s	4
Cut-out wind speed	$V_{cut-out}$	m/s	25

7.3. Aerodynamic input

The Huisman model has a different airfoil profile: the NACA0021. The NACA0021 profile can be seen in Figure 7.2. The aerodynamic input shall thus need to be changed to match the correct airfoil profile. In Appendix C, the extrapolation of the NACA0021 polars is illustrated. The maximum thickness of the airfoil is 21%, found at 30% of the chord [120]. Even though a higher maximum thickness increases the structural strength, it implements a higher drag coefficient at lower angles of attack [42]. The maximum chamber is found to be 0%, at 0% of the chord (meaning, there is no chamber).

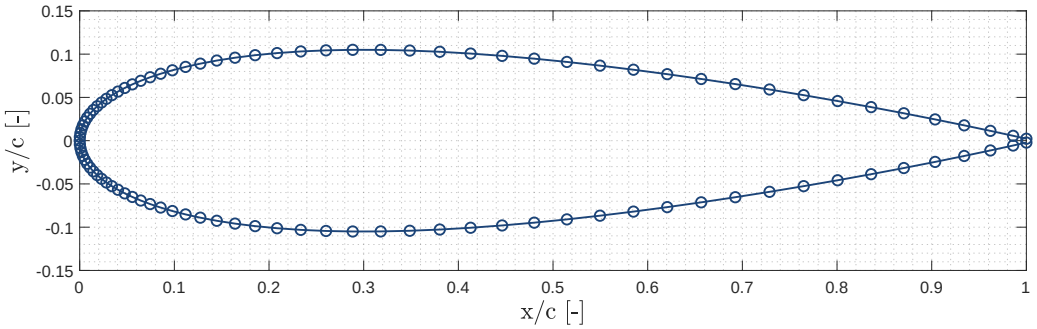

Figure 7.2: The NACA0021 profile normalized with the chord length (c).

7.4. Operational conditions

The operational conditions of the Huisman design are described in Table 7.3. As can be seen, the design tip speed ratio is λ = 4. The rotational speed is kept constant after higher wind speeds than rated. Even though the design is aimed to have a rated wind speed of 11 m/s, the wind speed is set at 12 m/s to

simulate similar conditions of the reference model. The rotational speed is then found with the tip speed ratio at ω = 0.6.

Table 7.3: Performance and operating parameters of the Huisman design.

Performance parameter	Parameter	Unit	Value
Power output	P	MW	10
Design tip speed ratio	λ	-	4
Wind speed	V_{wind}	m/s	12
Rated rotational speed	ω	rad/s	0.6

7.5. Results

The results of the simulation are provided in this section. It starts with the results related to the power output, which are shortly compared to the company's findings. Moreover, the differences between the dynamic stall models are checked for this HAWC2 model as well. In addition, the blade behavior is looked into as well as the natural frequencies. Ultimately, the results are compared to a report of the company.

7.5.1. Power output

Figure 7.3 illustrates the power output over one rotation. The mean power out of HAWC2 is higher than the design power of the design. This is a promising observation, as the design can go to higher operational ranges and the rated wind speed can be extended. According to this finding, the turbine may generate more power than anticipated under the existing operating circumstances. The mean power is found at $\approx$ 10.55 MW. This simulation has been executed with the B-L dynamic stall method.

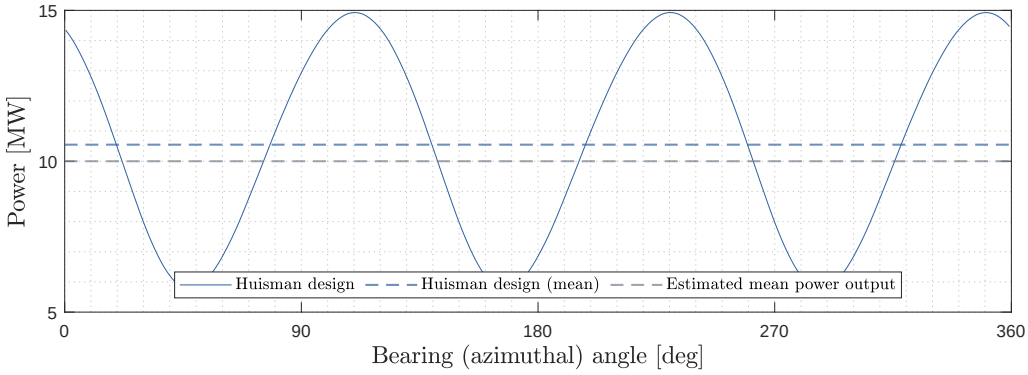

Figure 7.3: The power (P) over one rotation of the simplified Huisman design.

Table 7.4 provides a comparison of performance parameters between the simplified Huisman model simulated in HAWC2 with the company's findings. It should be noted that the rated wind speed of the Huisman model is at 11 m/s, and therefore, the optimal power coefficient (C_p) lies higher than what is found in Table 7.4 due to different operational conditions. The optimal power coefficient found by the company is $C_p = 0.48$.

Table 7.4: Comparison of the performance parameters between the simplified Huisman model and the company's findings.

Parameter	Symbol	Unit	Simplified model	Huisman model
Mean power	P	MW	10.55	10.01
Power coefficient	C_p	-	0.39	0.37

7.5.2. Dynamic stall model

Figure 7.4 shows the power output of the simplified Huisman design while two different dynamic stall models are applied. Their corresponding means are also shown. As has been previously noted, the

Øye model gives a higher power output than the Beddoes-Leishman model. The different lift and drag coefficient calculations could be the cause of this variance in power output. The next section (Section 7.5.3) will investigate the lift and drag coefficients in order to obtain a thorough grasp of these aerodynamic phenomena.

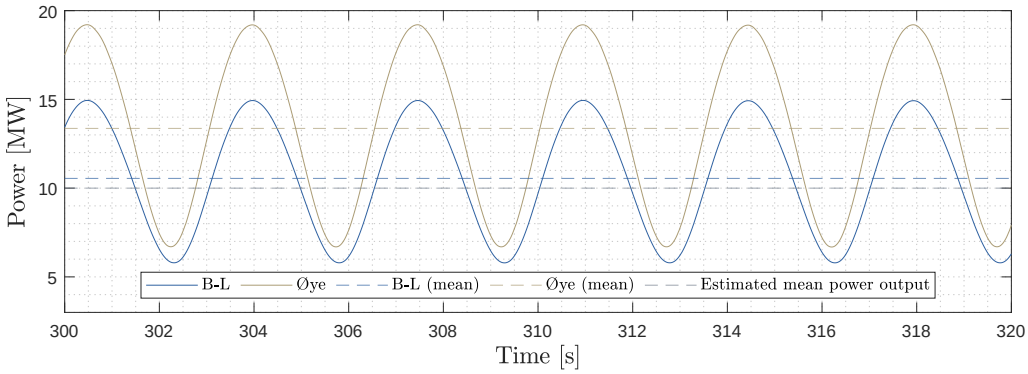

Figure 7.4: The power (P) as a function of time for the two different dynamic stall models.

7.5.3. Aerodynamic loads

As can be seen in Figure 7.5, the dynamic stall differs significantly in producing the drag coefficient. Once again, the aerodynamic parameters, shown in Figure 7.5, are taken from the bottom of the blade. The Øye model has a very small drag coefficient over the whole rotation, which leads to less drag and therefore higher power output of this model in comparison to the Beddoes-Leishman model. This has been also observed in Section 6.6.

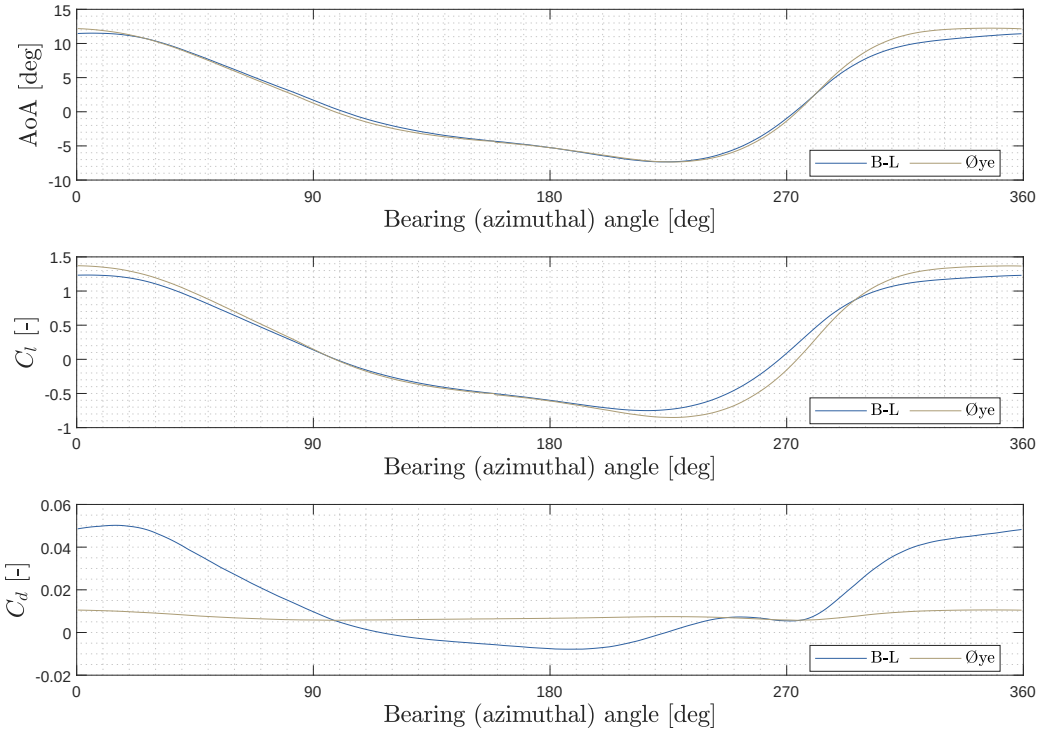

Figure 7.5: The angle of attack (AoA), the instantaneous lift coefficient (C_l), and the instantaneous drag coefficient (C_d) over one rotation for the simplified Huisman design, comparing the two dynamic stall models (Øye and Beddoes-Leishman).

7.5.4. Blade behavior

This subsection provides the results of the blade behavior of the simplified Huisman design. First, the overall deflection of the blade is offered at three different positions: the tip, middle, and bottom. An

understanding of the structural integrity and performance of the blade is thus acquired. In Table 7.5, the maximum values of the total deflection along the blade are written down. It concludes that the tip of the blade deflects the most, up to almost 8 meters. The bottom of the blade has the smallest deflection.

Table 7.5: Total possible maximum deflection along the blade of the simplified Huisman model in HAWC2.

Parameter	Symbol	Unit	Value
Max. deflection bottom of blade	w_b	m	1.19
Max. deflection position of bottom strut	w_{bs}	m	1.04
Max. deflection middle of blade	w_m	m	2.25
Max. deflection position of upper strut	w_{us}	m	2.27
Max. deflection tip of blade (up)	w_t	m	7.96

The circular motion of the tip of the blade can be seen in Figure 7.6. Only the upper tip is chosen to be visualized due to its highest found maximum deflection in Table 7.5. From Figure 7.6, it can be seen that the deflection fluctuates over the rotation, and the upper part of the rotor experiences the higher deflections.

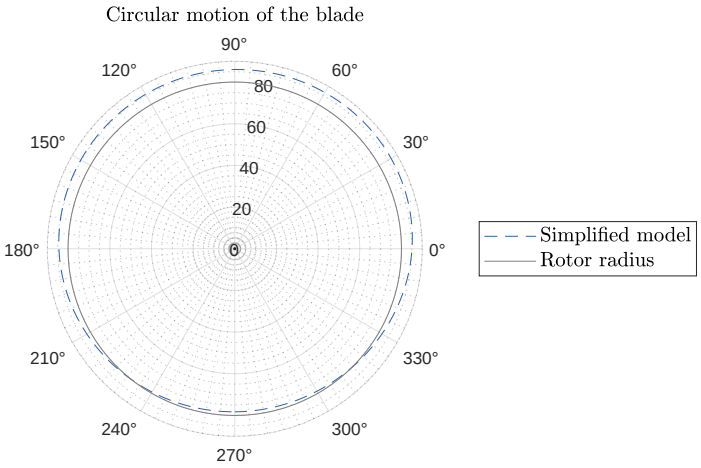

Figure 7.6: Circular motion of the tip of the blade for the simplified Huisman model.

In Figure 7.7, the deflection in the z-direction of the blade is shown over one rotation. It can be seen that the blade moves approximately 3 meters up and down.

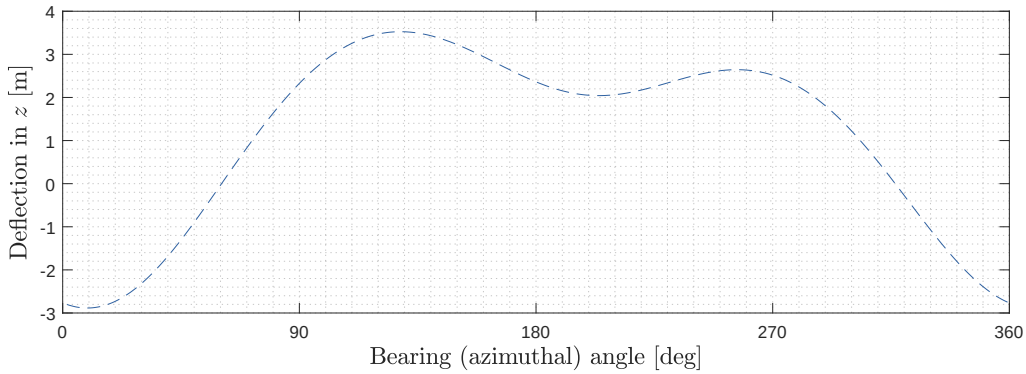

Figure 7.7: The deflection in z-direction for the simplified Huisman model over one rotation.

7.5.5. Natural frequencies

The undamped natural frequencies of the simplified Huisman model's structure and components are written down in Table 7.6. The examination of natural frequencies attempts to evaluate any potential inference

with the simulation results. As the model is simplified, the natural frequencies are not specific but only function as a base. It can be seen that the first eigenmodes are more than $\pm$ 10% away from the turbine's rotational speed. To prevent resonance and failures by vibrational effects, it is crucial to have natural frequencies outside of this range. As a result, the vibrations can be minimized and the structural integrity can be preserved.

Table 7.6: Undamped natural frequencies (f_n) of the model's structure and components (blade and strut).

	Undamped natural frequency f_n [rad/s]		
Mode nr.	**Blade**	**Strut**	**Structure**
1	0.49	2.02	0.88
2	0.79	2.45	0.88
3	3.05	19.78	0.88
4	4.94	24.39	0.97
5	8.58	52.09	0.99
6	13.90	187.53	0.99

7.5.6. Comparison with company's findings

As the Huisman model is also examined by the company (Huisman), the model can also shortly be compared to their findings. This subsection compares different results from the HAWC2 model to the Finite Element Method (FEM) analysis of Huisman.

FE model

A FEM analysis is done on the Huisman model. The structure is represented by beam elements in a simple FE model. However, the structure is more complex and kept closer to the original design than the HAWC2 model of the simplified Huisman model. The materials are identical, however, CFRP has slightly different characteristics. The material for the CFRP is thought to match the T700 type of carbon fiber, with a volume of 60–65%. The models have the same material configuration: hub (St52), struts (CFRP), and blades (CFRP).

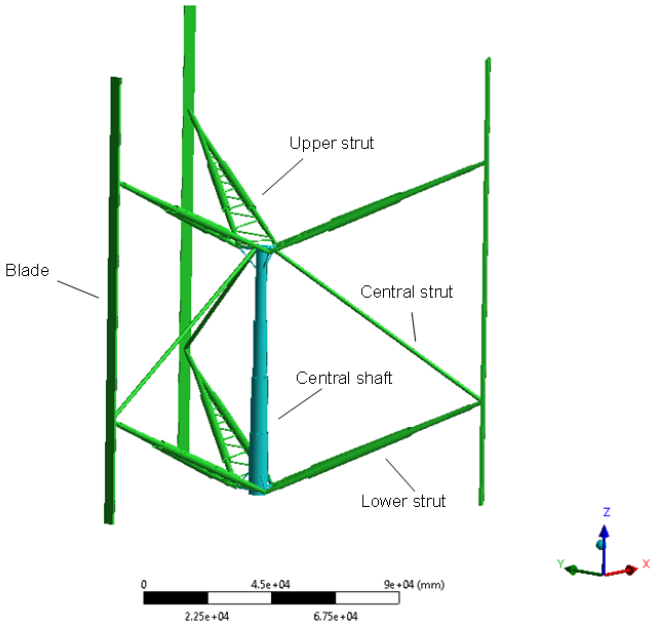

Figure 7.8: Visualization of the FE model of the VAWT design, in which beam elements are used [101].

Loads on VAWT come from an aerodynamic model that TU Delft gave, which consists of forces and moments on the blades. Two types of loads are investigated: operational loads (including angular velocity) and survival loads (without angular velocity, the turbine is locked). Each blade receives a uniformly distributed load applied to it along its whole length. The two connecting nodes between each blade and the

struts are where the moment on each blade is applied. Gravity is applied to every scenario, while angular velocity is only applied to the operational load cases.

Results
Table 7.7 summarizes the FEM results of the deformations of the configuration that matches the simplified Huisman model in HAWC2. The report [101] notes a few things about the results. First of all, deformation determines the strut and blade structures (not stress). If larger stresses are allowed, deformations shall increase unrealistically large. The maximum deflection of the blades is only slightly impacted by optimizing the blade cross sections over the length. Due to the way the struts support the blades, a constant cross-section is near to being the blades' ideal shape.

As can be read in Table 7.5, the simplified model in HAWC2 reaches a total maximum of almost 8 meters at the tip. This is significantly more than the FEM results, in which the maximum deformation is also found for the blade tip. Given the size of the rotor (blade length of 160 meters), a deformation of the blades of roughly 3 meters is seen as acceptable. For the other part of the blade, the deflection stays within 2.5 meters. Furthermore, the blade moves much more in the z-direction. The simplified HAWC2 model moves up and down in total more than three meters. The FEM analysis says that the maximum and minimum deformation deviates by 1 meter.

Table 7.7: FEM results of the deformation by Huisman.

Parameter	Symbol	Unit	Value
Deformation all max	w_{max}	m	2.452
Deformation Z min	$w_{z,min}$	m	-0.585
Deformation Z max	$w_{z,max}$	m	0.497

Because of the impact on the angular velocity, the mass of the blades has a substantial impact on their stress and deformation. A comparison of the components' masses can be seen in Table 7.8. The blade mass is slightly higher, compared to the FEM model. This can be related to the laminates in the blade, their thickness and layup are taken from the reference model and applied to the new airfoil. The struts cannot be compared well, as the Huisman model has three different struts. In general, it can be said that the strut mass is found in the ranges of the minimum and maximum masses of the struts. Moreover, as the tower is increased in height in the HAWC2 model, the hub mass is larger. The report mentions that due to the low-stress levels in the shaft and the hub, structural steel can be used for the shaft where no loads are applied and there are no stress concentrations [101].

Table 7.8: Comparison of the masses between the FE model by Huisman and the simplified Huisman model in HAWC2.

Parameter	Symbol	Unit	#	FEM	HAWC2
Blade mass	m_B	ton	3	45	65.7
Strut mass (upper/central/lower)	m_S	ton	3	23 / 5 / 41	30.7
Hub mass	m_H	ton	1	585	646

7.6. Discussion

There are a number of reasons why the results determined by the HAWC2 model and the Finite Element Analysis (FEA) analysis differ. In this subsection, the main possible reasons are shortly discussed.

Differences in models
The HAWC2 model is simplified so that the model could easily be implemented in HAWC2. The specific struts are difficult to simulate in HAWC2. HAWC2 has a global coordinate system, which is used to establish the orientation of each coordinate system [1]. Each body has its own coordinate system. A reference system and a selection of Euler angles that alter the orientation of the former are now used to define each coordinate system. Figure 7.9 illustrates a transformation from the original reference coordinate system of X_0, Y_0, and Z_0 to the new system of X_2, Y_2 and Z_2 using three more Euler angles. For this reason, it is difficult and time-consuming to model the entire struts. For this reason, the struts are kept the same as the reference model (two horizontals), but therefore, the results can deviate.

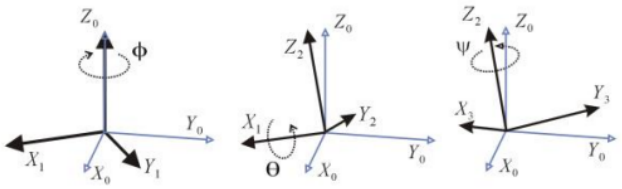

Figure 7.9: Euler angles can be used to change the coordinate system orientation [96]. Above, an example of a rotation sequence is shown: (1) Rotation around Z_0 axis of -60 degrees, (2) Rotation around Z_1 axis of 30 degrees, and (2) Rotation around Z_2 axis of 45 degrees.

Besides, as mentioned before, the material properties of CFRP differ. As BECAS requires more input values of the material (see: Table 4.1), the material properties of CFRP which are used for simulating the reference model are utilized.

Therefore, the simplifications and assumptions in the HAWC2 do not fully represent the same behavior of the wind turbine. These simplifications might not accurately reflect the complexity of the structural behavior, which could result in differences between the found deflections from the more in-depth FEA analysis.

Tools

Secondly, it can also be explained by differences in the tools. Both modeling tools are based on different numerical models and approaches. While HAWC2 uses aeroelastic modeling with some assumptions that may alter the results, the FEA normally uses a more precise and detailed depiction of the structural components. In addition, the boundary conditions can be different, leading to variations in the results.

Moreover, HAWC2 is a tool that specializes in simulating aeroelastic effects. The aerodynamic loads are therefore assumed to be incorporated better. HAWC2 takes into account the dynamic effects, like the dynamic stall. These effects can affect the results in comparison with FEA. FEA might not adequately account for these dynamic impacts.

7.7. Conclusion

In conclusion, the Huisman model is simplified with the parts of the reference model so that it can be simulated in HAWC2. Due to these simplifications, it is difficult to make direct statements about the structural characteristics of the model. The blade has higher blade deflection than the reference model itself, principally as a result of longer blades and a larger rotor radius. However, the aerodynamic output looks promising and close to the aimed power output of Huisman. The power output is slightly higher than the original design (around 10 MW). Furthermore, the natural frequencies are not close to the rotational velocity of the rotor so a critical failure mode can be avoided.

Ultimately, the results look good next to the Finite Element Analysis of Huisman. The only sharp observation is the significantly larger deflection at the tip of the simplified HAWC2 model. However, it should be noted that the model is simplified and elements of the reference model are used instead of the original model (such as the laminate layup and thicknesses, and the cross-sections of the struts).

8

Discussion

The discussion of this project provides a thorough evaluation of potential reasons for observed outcomes that differ from the original reference model of Schelbergen [5] or for results that might be less reliable due to the software limitations and assumptions. There might be underlying factors that have influenced the results. In addition, methodological considerations that are encountered during the research project are examined. Even though the project's models are not definitive, the results can inspire further studies and discussions.

8.1. Comparative analysis with the reference model

This section examines the potential causes of the observed differences between the HAWC2 and reference model. The two models under consideration are different regarding the analysis software they use and their structural properties. The differences between both structural models will be discussed first, highlighting differences in design elements like the tower and the laminate thickness. These variations might affect the performance and behavior of the wind turbine and the comparison with the reference model. Additionally, differences in the use of software are discussed. Different results could be caused by variations in meshing methods, wind models, or solver settings. By looking at these factors, the reasons behind the differences between the outcomes can be explained.

8.1.1. Structural model

Foremost, the differences between the structural models used in the current project and the reference model are covered in detail in this subsection. By mentioning these differences, such as the laminate thickness, the deviations in results can be explained.

- **Tower:** The reference model is evaluated without a tower, while a tower is required for a model in HAWC2. Therefore, a tower made from structural steel is added for the HAWC2 model. For this reason, certain results with the reference model cannot be compared to each other.
- **Laminate thickness:** The report of Schelbergen [5] does not specify anywhere which optimum thickness is used in the end. Only a broad range for optimal laminate thickness for each structural member in the blade and strut is given. As the maximum thickness is chosen for the HAWC2 model, the models will not structurally be the same. As a result, some aspects will differ from each other, like the mass and natural frequencies.
- **Material properties:** The report of Schelbergen [5] did not provide specific material properties of CFRP needed for BECAS. Therefore, slightly different properties were found instead. Furthermore, there are no material properties specified for the core material. Thus, the material properties found in the Airfoil2BECAS manual were used instead. This can also lead to differences in the structural properties and masses of the rotor.
- **Stiffness:** To the reference model, pre-stiffening is applied to determine the eigenvalue of the first buckling mode. His first buckling analysis revealed that the buckling eigenvalues have poor convergence. To perform a credible buckling analysis, a larger mesh was needed, while also pre-stiffening of the structure in MSC Nastran is needed to have a reliable analysis. However, this is not done for the structural model in HAWC2.
- **Aerodynamic input:** The chosen airfoil profile of the reference model has no available data for use in HAWC2. As mentioned before, HAWC2 requires a ”pc-file”, which contains the polars of the airfoil for 360 degrees. However, an airfoil with similar thickness, the NACA0031, is used instead. As the airfoil of the reference model is optimized by Prof. Carlos Simão Ferreira, it would be assumed that there would be a power penalty visible due to the NACA0031 profile.

8.1.2. Differences in software framework

The two models both make use of different tools to simulate the wind turbine. In this subsection, the distinctions between these tools are discussed. These differences include various ways in which aerodynamics and blade meshing have been implemented, as well as the absence of dynamic stall modeling in the reference model. As a result, differences in the behavior of the wind turbine can be observed.

- **Aerodynamics:** The reference model is simulated in the FEM software named MSC Nastran. The FEM analysis in MSC Nastran applies the aerodynamic load to the blade using a constant, chord-wise pressure coefficient distribution [5]. The results come from a 2D unsteady panel simulation in potential flow by Prof. Carlos Simão Ferreira. He states that blade-wake contact happens throughout the blade rotation's windward, downwind, and leeward sections. The angle of attack at these rotating sections fluctuates due to this interaction. HAWC2 uses the two-dimensional actuator cylinder model, commonly known as the 2D actuator cylinder model, for VAWTs [81]. However, it uses a modified linear solution of the actuator cylinder approach. This method is faster and computationally more efficient than vortex and full CFD solutions while being more physically correct than the double-stream tube method. So, the aerodynamic forces are simulated more realistically in HAWC2. HAWC2 includes a dynamic calculation model. It considers the dynamic stall and it can use Prandtl's method for tip loss correction. Furthermore, induction is also applied in the aerodynamic model.
- **Dynamic stall model:** The model turns quasi-steady if no dynamic stall model is used [110]. No dynamic effects are replicated; the aerodynamic forces are simply determined by looking up the profile coefficients. Øye's model, though delivers the stall dynamics on the lift coefficients but not on the drag and moment coefficients and does not produce dynamics in the attached flow. The results are less accurate because Øye's model does not produce attached flow dynamics.
- **Simulation issues:** When there is insufficient simulation convergence, the results can deviate from what is expected. The simulation settings, such as the step size and convergence criteria, are critical. If the simulation is run for a more extended period of time, the accuracy and stability of the results could potentially improve.
- **Mesh:** Both in the reference model and the HAWC2 model, the strut is modeled as a beam and linearly meshed. However, he makes a trade-off in the mesh density to get sufficient accuracy while having a tolerable optimization time. In Airfoil2BECAS, several element layers are decided on experts' advice in simulations with BECAS and HAWC2. When more than 100 nodes (140) on the airfoil profile are implemented, BECAS can mention that it needs to process many elements but still does it.
- **Thickness distribution:** Airfoil2BECAS automatically generates a continuous (node-based) thickness distribution to eliminate discontinuities at the boundary between two regions [92]. As a result, mesh generation becomes easier. The continuous thickness distribution of the airfoil can be seen in Figure 8.2. The reference model of Schelbergen [5] uses the blade geometry parameterization, covered in the work of Ferede et al. [121]. This method makes use of NURBs (Non-Uniform Rational Basis Splines). NURBs utilize control points to create curves and surfaces. The beam axis, twist, and (weighted) airfoil shape are parameterized at each control point. The beam axis controls the geometrical characteristics of the blade (i.e., sweep, curvature). The weighted airfoil forms control the blade's chord and cross-sectional shape distribution. Using the geometry in a finite element analysis is simple since the code can discretize (mesh) the geometry in shell elements. The work of Schelbergen [5] mentions that the thickness of all structural members can be set apart (see: Figure 8.1), which maybe implies that there is no tool for making the thickness distribution between the structural members continuous. Both the blade and strut are modeled structurally differently.

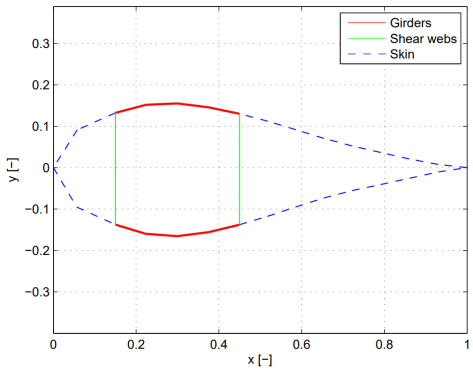

Figure 8.1: The discretized blade cross-section from the reference model, in which the structural members are visible [5].

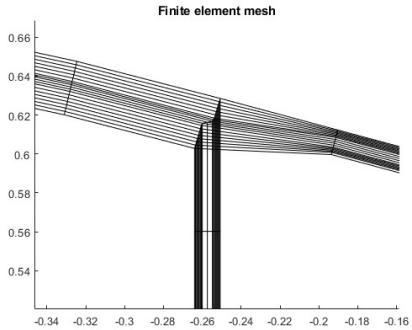

Figure 8.2: Zoomed-in view of the finite element mesh used in this project.

8.2. Limitations of used tools

In this section, the tools used and their associated limitations are discussed. The tools, used in this project, are evaluated critically. Furthermore, particular restrictions, such as computational limitations and challenges, are reviewed. It is crucial to consider these constraints when evaluating the results and extrapolating them to broader applications or future research. A brief overview of possible software causes for deviations in results is presented below.

- **Dynamic stall model:** Changing the dynamic stall model in HAWC2 can significantly alter the wind turbine's performance output, particularly its capacity to generate power. Even though the dynamic stall model is chosen in only one line, the change causes considerable differences in the expected power output. The dynamic stall model should be selected to correctly simulate the wind turbine model under dynamic stall situations. The right model should be chosen to provide the most accurate output.
- **Solver settings:** The simulation output can be significantly influenced by the solver settings in HAWC2. The results can be significantly changed by adjusting settings like the time-step size, convergence requirements, or solver type. A smaller time-step size can produce a representation of the transient flow behavior that is more accurate and detailed. Still, the simulation time will be longer, and the data storage will be more extensive. For larger tip speed ratios, the time-step is often made smaller. The solver settings have a direct impact on the fidelity and precision of the results, and these settings should be specified to ensure reliable solutions.
- **Convergence:** For the simulations in HAWC2 to be accurate and trustworthy, convergence is essential. The solution should become stable and satisfy specified convergence conditions. Convergence can be affected by variables like model complexity and mesh resolution. The solver settings should be specified properly. With looser convergence criteria, convergence can occur more quickly but with less accuracy.
- **Wind model:** The wind model used in the simulations assumes a constant horizontal wind speed of 12 m/s. No turbulence is defined. As a result, the turbulence intensity is zero, the turbulence format is not defined, and the wind field rotations are ignored. Moreover, no tip loss methods or tower shadow methods are implemented. The lack of these additional definitions for the wind model may constrain the accuracy of the results. Different settings, such as adding turbulence and tower shadow effects, could produce outcomes closer to real-life wind situations. Therefore, the realism and accuracy of the simulations could be improved.
- **Damping:** HAWC2 requires damping, which is tuned for every model's first three eigenmodes to have a lograment decreasement below 3%. It should be noted that the damping is added by trial and error.
- **Coordinate systems:** Comparing several positions along a body might be difficult with the local coordinate system of the body. At the origin of the coordinate system, where the coordinate system is specified, the parameters will come out as zero. Along the body, further away from the origin, the results look more like expected. Consequently, relying only on the local coordinate system could result in bad comparisons. Therefore, some parameters should be taken from the global coordinate system to prevent this.

- **Output sensors:** The availability of data for analysis may be constrained in some circumstances by output sensors. Some sensors only supply data at specific nodes or locations. As a result, there is limited access to data and this can make it difficult to fully comprehend the behavior and functionality of the system. Furthermore, some sensors may not be able to accurately capture specific parameters. To ensure the accuracy of the data, it is crucial to carefully assess the available output sensors.

9

Conclusions and recommendations

This chapter includes the conclusions to this Master's thesis while it answers the research questions. The conclusion provides a summary of the key findings and discoveries found while investigating the design drivers of a vertical axis wind turbine (VAWT). The significance of the discovered design drivers is elaborated, highlighting what effects they have on the aeroelastic stability, performance, and behavior of the VAWT. By addressing these factors, the groundwork for further development and improvements is laid. Ultimately, recommendations and possible future research topics are provided based on the conclusions.

9.1. Conclusions

This thesis project aims to find the design drivers of the H-rotor type vertical axis wind turbine. While other researchers have already covered similar topics in the past, this thesis covers a parametric study of the VAWT design and parameters, while also looking at the upscaling of the VAWT design. The results are compared to the literature if applicable. In short, the central objective of this thesis can be summarized to:

The research objective is to investigate the design drivers and their impact on the aeroelastic behavior, structural integrity, and performance of H-rotor vertical axis wind turbines (VAWTs).

Numerous research questions were developed to accomplish this goal, along with a systematic research methodology. The project started to model and simulate a reference turbine in HAWC2 with the help of BECAS. Based on these results, different design drivers were determined and investigated. Moreover, other design drivers, the upscaling of the rotor, and the Huisman model were evaluated.

Aeroelastic stability

The undamped natural frequencies of the structure and its components are taken into consideration during the evaluation process. This is in order to look into the aeroelastic stability, which can contribute to the critical failure modes of the VAWT. The natural frequencies are checked to see if they cause any resonance at the design rotational speed or operational range. As a result, possible resonance problems are detected.

Design drivers for the VAWT

This study has identified several design drivers of the H-rotor vertical axis wind turbines (VAWTs). These design drivers affect how VAWTs perform and behave aerodynamically. This study shows that the laminate thickness in the blade, the placement of the struts, and an additional strut have an impact both on the structural integrity and the performance of the wind turbine. In addition, the aspect ratio is also found to affect the performance and behavior of the wind turbine.

Impact of laminate thickness

Based on the results, a blade with smaller laminate thicknesses can be favored. A smaller laminate thickness translates into a lower mass, resulting in lower costs and a lighter-weight design. As a result, the goal of lowering the mass over the swept area would be best satisfied in this case. Moreover, no significant reduction in power output is found with a lower laminate thickness. It still shows good overall performance. The natural frequencies are well out of range of the operational rotational speed. However, this should be carefully checked when another model is designed. One downside of the lower laminate thickness is that the blade would most likely have less structural stability in the design, which eventually contributes to larger blade deflections. A blade's stiffness is generally increased by thicker laminates, which can lead to smaller deflections. Therefore, the best trade-off between the upsides and the downside should be made.

Impact of strut placement
The power output can be maximized by placing the struts at different positions on the blade (while keeping it symmetric). How higher the strut is placed towards the midpoint, how higher the power output is. However, the power varies minimally. The ideal placement of the struts can be found in the range of x_{strut}/H = 0.23 to 0.27. At this placement, the power output is maximized. Furthermore, compared to the other strut placement, it has been demonstrated that the maximum deflections surrounding this placement are relatively small. The best balance between power and structural integrity is therefore provided.

Impact of additional diagonal strut
By adding another diagonal strut to the original H-rotor design, structural benefits, as well as potential drawbacks, can be offered. First of all, the modified design has improved natural frequencies that increase the stability and structural integrity of the turbine during operation. Additionally, the majority of the deflection along the blade is decreased, which improves the dependability of the turbine. Nevertheless, the additional diagonal strut has a cost impact. Three extra struts in total add more mass, interfering with the optimization goal of decreasing the mass over the area to save costs and maximize power production. The modified model produces more or less the same power output as the original model. Subsequently, a comprehensive cost-benefit analysis is necessary to see if the improved structural features weigh out the economic factors.

Dynamic stall
Furthermore, in this research, the dynamic stall has been recognized to have a significant impact on the performance of a VAWT. The results from two dynamic stall models (Beddoes-Leishman and Øye) show notable differences in their performance output, which are mostly related to the different ways of calculating the lift and drag coefficient. For this reason, it is crucial to take the dynamic stall effects into account when modeling a VAWT in any tool. Even though the Beddoes-Leishman dynamic stall model produces lower power outputs across all simulations, this model is said to be more accurate to capture the dynamic stall effects. To have more accurate results, the right dynamic stall model should be chosen and used in the modeling methodology.

Upscaling
The research into scaling up the VAWT to greater multi-MegaWatt outputs shows that raising the aspect ratio, accomplished by increasing the blade length, has a favorable effect on the mean power output. However, the blade deflection is increased, which could lead to more structural issues for the wind turbine. In addition, longer blades could lead to higher costs. These factors should be taken into consideration during the upscale phase. Ultimately, when scaling up to larger power outputs, maintaining aeroelastic stability and avoiding resonance issues remain critical. The natural frequencies of the blade as well as the natural frequencies of the entire construction are found to decrease as the aspect ratio rises.

Huisman design
The Huisman VAWT design is simplified based on the reference model in HAWC2. It is challenging to directly state the model's structural properties as a result of these simplifications. However, the outcomes match well with the Finite Element Analysis of the company. The simplified HAWC2 model's substantially bigger deflection at the tip is the only notable finding. The aerodynamic output, though, is encouraging. The power output (about 10 MW) is a little bit higher than the original design. Additionally, critical failure scenarios can be avoided because the natural frequencies are not too close to the rotor's rotational speed.

Advancing VAWTs for the future
In summary, this study has shed light on the design drivers of the VAWT design, the effects of structural changes, and the upscaling effects. This study offers insight that can guide future VAWT designs so that the performance can be improved while the aeroelastic stability can be guaranteed. As a result, the development of new sustainable wind energy solutions - such as the VAWT - can be progressed.

Additionally, there is significant potential for VAWTs in practical applications and commercial implementations. VAWTs have the potential to be used in the offshore market, as the design can be scaled up to high multi-MegaWatt outputs to challenge HAWTs. On top of that, this study can be used as a basis for additional research and advancement in the area of VAWTs.

9.2. Recommendations

The current study can be seen as the beginning of a larger investigation into the design drivers and optimization of the VAWT design. As the results vary from the reference model and each other for example with different dynamic stall models, the results should be taken as guidelines. The project also contains

certain limitations. Nevertheless, there are various potential study subjects for new research, building on this project.

- **Investigation of additional design drivers:** There are many design factors not taken into account or not found in this project. The inquiry to find and investigate other essential design drivers can be expanded. Other parameters could be the connection between the struts and blades (pitch control), the specific blade design, and the strut design, or any other design options.
- **Development of a controller for VAWTs in HAWC2:** During this project, there was no available controller for VAWTs. Therefore, it would be helpful for the simulations to become more accurate when a suitable controller is made for VAWTs in HAWC2.
- **Floating construction:** As mentioned in the introduction, VAWTs will become more attractive when placed floating. A floating construction should be designed for VAWTs. Furthermore, the VAWT design should be investigated when wave loads are taken into account.
- **Strength analysis:** The stress and strain recovery function of BECAS can be used to determine whether the material can withstand these strains. BECAS determines the corresponding stresses and strains in the blade by applying the anticipated maximum loading to it. If the acceptable stress or strain is known, it can be used to determine whether the material's maximum allowable stress or allowable strain has been reached.
- **Fatigue analysis:** Fatigue analysis evaluates the structural integrity and toughness of components under cyclic loading. The effects of various design drivers on the fatigue life of a VAWT design can be investigated. The fatigue resistance of a turbine can be improved by identifying crucial locations that are prone to fatigue failure. By figuring out the best inspection intervals and creating fatigue-based maintenance schedules, the study can also help to improve maintenance tactics. The structural performance of a VAWT can be investigated for long-term use.
- **Experimental validation:** To validate the simulation results, experimental tests can be conducted. The VAWT design can be scaled down for a physical replica in the wind tunnel.
- **Load cases:** The current design drivers are found and simulated for one specific load case, which is the optimal operating conditions. The VAWT design should also be checked for other load cases, such as gust and parked conditions. A more thorough aeroelastic analysis can be run to determine whether the wind turbine maintains its stability by adding more load cases.
- **Optimization:** Once a reasonable first design is made, a high-fidelity optimization can be done to specific components of the rotor.
- **Cost and manufacturing analysis:** Once the end design of the VAWT has been created and optimized, it is necessary to assess its manufacturability. This investigation covers not only the technical viability but also a cost analysis.

On top of that, recommendations can be made to Huisman. The future of VAWTs seems to be promising, suggesting a competitive and reasonable path for their growth. However, it is crucial to recognize that the road ahead is not easy. Although there is clear potential, it will be challenging to go from theoretical research to real-life implementation. Not many companies or institutions have taken the risk of building large-size VAWTs. Significant research and development efforts are necessary to close this gap. Even if the real-life implementation will not happen right away, contributions to research projects on VAWTs are quite valuable. Each step will help advance renewable energy, paving the way for a greener and more sustainable future.

References

[1] Anders Melchior Hansen et al. *How 2 HAWC2, the user's manual*. Risø DTU - National Laboratory for Sustainable Energy, 2007.

[2] J. Thirstrup Petersen. "The aeroelastic code HawC - model and comparisons". English. In: *State of the art of aeroelastic codes for wind turbine calculations*. Ed. by B. Maribo Pedersen. 28th Meeting of Experts ; Conference date: 11-04-1996 Through 12-04-1996. Technical University of Denmark. Department of Fluid Mechanics, 1996, pp. 129–135.

[3] J.P.A.A. Blasques et al. *Applications of the BEam Cross section Analysis Software (BECAS)*. 2013, pp. 46–49.

[4] José Pedro Blasques et al. *User's Manual for BECAS: A cross section analysis tool for anisotropic and inhomogeneous beam sections of arbitrary geometry*. 2015. URL: www.becas.dtu.dk.

[5] M. Schelbergen. "Structural Optimization of Multi-Megawatt, Offshore Vertical Axis Wind Turbine Rotors". MA thesis. Delft University of Technology, 2013.

[6] B. Roscher. "Structural Optimization Of A Vertical Axis Wind Turbine With Aeroelastic Analysis". MA thesis. Delft University of Technology, 2014.

[7] Boy S. Koppenol. "Dynamic Analysis of a Floating Vertical Axis Wind Turbine using the Actuator Cylinder Flow Theory". MA thesis. Delft University of Technology, 2016.

[8] Greeshma Boohalli Shivamallegowda. "Simulation and optimisation of unsteady aerodynamic per-formance of a 2D VAWT rotor". MA thesis. Delft University of Technology, 2018.

[9] Alternative Energy Tutorials. *Vertical Axis Wind Turbine*. 2022. URL: https://www.alternative-energy-tutorials.com/wind-energy/vertical-axis-wind-turbine.html. (Accessed: December 2022).

[10] Ben Pilkington. *An Introduction to Vertical Wind Turbines*. 2020. URL: https://www.azocleantech.com/article.aspx?ArticleID=457. (Accessed: December 2022).

[11] Tyson Brown. *Wind Energy*. Ed. by National Geographic Society. 2022. (Accessed: January 2023).

[12] Farhan Ahmed Khammas et al. "Overview of Vertical Axis Wind Turbine (VAWT) is one of the Wind Energy Application". In: *Applied Mechanics and Materials* 793 (Sept. 2015), pp. 388–392. DOI: 10.4028/www.scientific.net/amm.793.388.

[13] Anna M. Maehr et al. "Emotional response to images of wind turbines: A psychophysiological study of their visual impact on the landscape". In: *Landscape and Urban Planning* 142 (2015), pp. 71–79. DOI: 10.1016/j.landurbplan.2015.05.011.

[14] Niels-Erik Clausen. *Environmental Impact Assessment of Offshore Wind Farms*. University Lecture (Technical University of Denmark). 2022.

[15] H. J. Lindeboom et al. "Short-term ecological effects of an offshore wind farm in the Dutch coastal zone; Acompilation". In: *Environmental Research Letters* 6 (3 2011). DOI: 10.1088/1748-9326/6/3/035101.

[16] Lizet Ramírez et al. *Offshore Wind in Europe: Key trends and statistics 2019*. Tech. rep. 2020.

[17] National Grid Group. *Onshore vs offshore wind energy: what's the difference?* n.d. URL: https://www.nationalgrid.com/stories/energy-explained/onshore-vs-offshore-wind-energy. (Accessed: December 2022).

[18] Haoyue Wen. "Subspace Predictive Control for Vertical Axis Wind Turbines". MA thesis. Delft University of Technology, 2022.

[19] Willy Tjiu et al. "Darrieus vertical axis wind turbine for power generation I: Assessment of Darrieus VAWT configurations". In: *Renewable Energy* 75 (Mar. 2015), pp. 50–67. DOI: 10.1016/j.renene.2014.09.038.

[20] Saika Iwamatsu et al. “Study on Elastic Response of Double-Rotor VAWTs”. In: *Journal of Marine Science and Engineering* 10 (2022). DOI: 10.3390/jmse10101400.

[21] Rebecca Loomis et al. *Floating Offshore Wind Brings Challenges and Opportunities*. Ed. by NRDC. https://www.nrdc.org/experts/rebecca-loomis/floating-offshore-wind-brings-challenges-and-opportunities. 2021. (Accessed: January 2023).

[22] Mohammad Sadman Sakib et al. “Parked and Operating Loads Analysis in the Aerodynamic Design of Multi-megawatt-scale Floating Vertical Axis Wind Turbines”. In: (2021). DOI: 10.5194/wes-2021-60. URL: https://doi.org/10.5194/wes-2021-60.

[23] Adnan Memija. *Vertical Axis Turbines ‘Dramatically’ Increase Power Density at Offshore Wind Farms*. 2022. URL: https://www.offshorewind.biz/2022/09/20/vertical-axis-turbines-dramatically-increase-power-density-at-offshore-wind-farms-white-paper/. (Accessed: January 2023).

[24] Delphine De Tavernier. “VAWT aerodynamics”. In: *TU Delft* (2020).

[25] Carlos Simao Ferreira. *Floating Offshore Vertical Axis Wind Turbines: Introduction for brainstorm and current research at TU Delft*. University Guest Lecture. 2021. (Accessed: November 2022).

[26] Ahmed Ali Geneid et al. “Multi-objective optimization of vertical-axis wind turbine’s blade structure using genetic algorithm”. In: *Journal of Engineering and Applied Science* 69 (1 Dec. 2022). DOI: 10.1186/s44147-022-00150-z.

[27] Sandra Eriksson et al. “Evaluation of different turbine concepts for wind power”. In: *Renewable and Sustainable Energy Reviews* 12 (5 June 2008), pp. 1419–1434. DOI: 10.1016/j.rser.2006.05.017.

[28] T. Burton et al. *Wind Energy Handbook*. John Wiley and Sons, Ltd., 2001.

[29] Raunak Bagde. *Aerodynamic response of a two-dimensional vertical axis wind turbine to turbulence*. Delft University of Technology, 2017.

[30] Vertogen Ltd. *Wind Turbines - The Types & History*. 2020. URL: https://www.vertogen.eu/wind-turbine-history/. (Accessed: December 2022).

[31] Marco D’Ambrosio et al. “Vertical Axis Wind Turbines: History, Technology and Applications”. MA thesis. University West (Högskolan Väst), 2010.

[32] J.F. Manwell et al. *Wind Energy Explained*. John Wiley and Sons, Ltd., 2009.

[33] M.T. Kanaki et al. “Cretan windmills”. In: *Applied Energy* 5.3 (1979), pp. 215–222. DOI: https://doi.org/10.1016/0306-2619(79)90038-2. URL: https://www.sciencedirect.com/science/article/pii/0306261979900382.

[34] Solaripedia. *Project: Persian Windmills and Wind Towers from Ancient Times*. 2017. URL: http://www.solaripedia.com/13/80/persian_windmills_and_wind_towers_from_ancient_times.html. (Accessed: January 2023).

[35] Tim Haaker. *All about Dutch Windmills*. 2020. URL: https://starboardboats.nl/amsterdam-windmill-tour-blog/. (Accessed: January 2023).

[36] Redeemer Axisa et al. “Structural assessment of a lattice tower for a small, multi-bladed wind turbine”. In: *International Journal of Energy and Environmental Engineering* 8 (4 Dec. 2017), pp. 343–358. DOI: 10.1007/s40095-017-0239-3.

[37] Ignacio Mártil de la Plaza. *History of Windpower: From its Origins to World War II*. 2021. URL: https://www.bbvaopenmind.com/en/technology/innovation/history-of-windpower-from-origins-to-world-war-ii/. (Accessed: January 2023).

[38] Casey Crownhart. *The wild new technology coming to offshore wind power*. https://www.technologyreview.com/2022/12/08/1064499/new-technology-offshore-wind-floating/. 2022. (Accessed: May 2023).

[39] Ion Paraschivoiu. *Wind Turbine Design: With Emphasis on Darrieus Concept*. Presses inter Polytechnique, 2002.

[40] A. P. Schaffarczyk. *Introduction to Wind Turbine Aerodynamics*. Springer, 2014.

[41] Hongfu Zhang et al. “Improvement of aerodynamic performance of savonius wind rotor using straight-arc curtain”. In: *Applied Sciences (Switzerland)* 10 (20 Oct. 2020), pp. 1–19. DOI: 10.3390/app10207216.

[42] Leyre Redín Larrea. “Vibration Analysis of a VAWT”. MA thesis. Technical University of Sofia, 2013.

[43] Ali Benmeddour et al. “Overview of wind energy research and development at NRC-IAR (Canada)”. In: *Revue des Energies Renouvelables SMEE’10 Bou Ismail Tipaza* (2010), pp. 69–80. URL: https://www.researchgate.net/publication/228639182.

[44] Herbert J. Sutherland et al. *SANDIA REPORT: A Retrospective of VAWT Technology*. Sandia National Laboratories, 2012. URL: http://www.ntis.gov/help/ordermethods.asp?loc=7-4-.

[45] Andreas Johansson. *Concession in Norway gains legal force*. 2023. URL: https://seatwirl.com/news/concession-in-norway-gains-legal-force/. (Accessed: February 2023).

[46] Karl Arvidsson et al. “Early Concept Evaluation of Floating Vertical Axis Wind Turbines Method development and testing utilizing FE-modelling, structural optimization and H-rotor designs”. MA thesis. Chalmers University of Technology, 2022. URL: www.chalmers.se.

[47] Ahmed Y. Qasim et al. *Increase power coefficient for impeller type vertical axis wind turbine*. 2012, pp. 9641–9644. URL: https://www.researchgate.net/publication/230745591.

[48] Brian Hand et al. “Aerodynamic design and performance parameters of a lift-type vertical axis wind turbine: A comprehensive review”. In: *Renewable and Sustainable Energy Reviews* 139 (2021). DOI: 10.1016/j.rser.2020.110699.

[49] Mojtaba Ahmadi-Baloutaki et al. “Straight-bladed vertical axis wind turbine rotor design guide based on aerodynamic performance and loading analysis”. In: *Proceedings of the Institution of Mechanical Engineers, Part A: Journal of Power and Energy* 228.7 (2014), pp. 742–759. DOI: 10.1177/0957650914538631.

[50] M. Saqib Hameed et al. “Design and analysis of a straight bladed vertical axis wind turbine blade using analytical and numerical techniques”. In: *Ocean Engineering* 57 (2013), pp. 248–255. DOI: 10.1016/j.oceaneng.2012.09.007.

[51] Povl Brøndsted et al. *Advances in Wind Turbine Blade Design and Materials*. Woodhead Publishing, 2013.

[52] Simon Reijniers. “Design and Aeroelastic Analysis of Flexible Wind Turbine Blades”. MA thesis. Delft University of Technology, 2015.

[53] Yuqiao Zheng et al. “Optimization Method for Girder of Wind Turbine Blade”. In: *Mathematical Problems in Engineering* 2014 (2014). DOI: 10.1155/2014/898736.

[54] Kevin Cox et al. “Structural design and analysis of a 10MW wind turbine blade”. In: vol. 24. Elsevier Ltd, 2012, pp. 194–201. DOI: 10.1016/j.egypro.2012.06.101.

[55] Dervis Ozkan et al. “Carbon Fiber Reinforced Polymer (CFRP) Composite Materials, Their Characteristic Properties, Industrial Application Areas and Their Machinability”. In: vol. 124. Springer, 2020, pp. 235–253. DOI: 10.1007/978-3-030-39062-4_20.

[56] Pietro Bortolotti. “Carbon Glass Hybrid Materials for Wind Turbine Rotor Blades”. MA thesis. Delft University of Technology, 2012.

[57] James F. Manwell et al. *Wind Energy Explained: Theory, Design and Application*. John Wiley and Sons, Ltd., 2010.

[58] Habtamu Beri et al. “Double Multiple Streamtube Model and Numerical Analysis of Vertical Axis Wind Turbine”. In: *Energy and Power Engineering* 03 (03 2011), pp. 262–270. DOI: 10.4236/epe.2011.33033.

[59] F. Trivellato et al. “Appraisal of Strouhal number in wind turbine engineering”. In: *Renewable and Sustainable Energy Reviews* 49 (Oct. 2015), pp. 795–804. DOI: 10.1016/j.rser.2015.04.127.

[60] Yichen Jiang et al. “Investigation of blade tip shape for improving VAWT performance”. In: *Journal of Marine Science and Engineering* 8 (3 Mar. 2020). DOI: 10.3390/jmse8030225.

[61] Eduard Dyachuk et al. “Simulating dynamic stall effects for vertical axis wind turbines applying a double multiple streamtube model”. In: *Energies* 8 (2 2015), pp. 1353–1372. DOI: 10.3390/en8021353.

[62] Sébastien Le Fouest et al. “The dynamic stall dilemma for vertical-axis wind turbines”. In: *Renewable Energy* 198 (Oct. 2022), pp. 505–520. DOI: 10.1016/j.renene.2022.07.071.

[63] Carlos Simão Ferreira et al. “Airfoil optimization for stall regulated vertical axis wind turbines”. In: American Institute of Aeronautics and Astronautics Inc., 2015. DOI: 10.2514/6.2015-0722.

[64] Bruce P. LeBlanc et al. “Overview and design of pitchVAWT: Vertical axis wind turbine with active variable pitch for experimental and numerical comparison”. In: American Institute of Aeronautics and Astronautics Inc, AIAA, 2018. DOI: 10.2514/6.2018-1243.

[65] Gebreel Abdalrahman et al. “Pitch angle control for a small-scale Darrieus vertical axis wind turbine with straight blades (H-Type VAWT)”. In: *Renewable Energy* 114 (2017), pp. 1353–1362. DOI: 10.1016/j.renene.2017.07.068.

[66] M. Montenegro Montero. “Optimization of Cyclic Pitch Control for a Vertical Axis Wind Turbine”. MA thesis. Delft University of Technology, 2017.

[67] T. Kosaku et al. *Optimum pitch control for variable-pitch vertical-axis wind turbines by a single stage model on the momentum theory*. 2002.

[68] Kenneth Thomsen et al. *M13: Load Analysis*. University Lecture (Technical University of Denmark). 2022.

[69] Dick Veldkamp. *Standards and load calculations*. University Lecture (Delft University of Technology). 2020.

[70] Dutch Offshore Wind Atlas. *Weibull parameters a and k per wind farm zone and Cabauw*. https://www.dutchoffshorewindatlas.nl/atlas/image-library/image-library/weibull-parameters. n.d. (Accessed: June 2023).

[71] Brian Hand et al. “Structural analysis of an offshore vertical axis wind turbine composite blade experiencing an extreme wind load”. In: *Marine Structures* 75 (Jan. 2021). DOI: 10.1016/j.marstruc.2020.102858.

[72] Marco Raciti Castelli et al. “Numerical evaluation of aerodynamic and inertial contributions to Darrieus wind turbine blade deformation”. In: *Renewable Energy* 51 (Mar. 2013), pp. 101–112. DOI: 10.1016/j.renene.2012.07.025.

[73] C. Galinos et al. *Vertical-axis wind turbine design load cases investigation and load comparison with horizontal axis wind turbine*. 2016. URL: https://www.sintef.no/globalassets/project/eera-deepwind2016/presentations/c_galinos_a1session.pdf.

[74] C. Galinos et al. *Presentation of Vertical-axis wind turbine design load cases investigation and load comparison with horizontal axis wind turbine*. https://www.sintef.no/globalassets/project/eera-deepwind2016/presentations/c_galinos_a1session.pdf. 2016.

[75] D.W. Lobitz. “Dynamic Analysis of Darrieus Vertical Axis Wind Turbine Rotors”. In: (1981). URL: https://ntrs.nasa.gov/citations/19820015829.

[76] Dale E. Berg. *SANDIA Report: Structural Design of the Sandia 34-Meter Vertical-Axis Wind Turbine*. Sandia National Laboratories, 1985. URL: https://vdocument.in/841287-structural-design-of-sandia-34m-vawt.html?page=1.

[77] R.J. Templin. “Aerodynamic performance theory for the NRC vertical-axis wind turbine”. In: (1974). URL: https://www.osti.gov/biblio/7235638.

[78] Delphine de Tavernier et al. “Vertical-axis Wind Turbine Aerodynamics”. In: *Handbook of Wind Energy Aerodynamics*. Ed. by Peter Fuglsang Bernhard Stoevestandt Gerard Schepers et al. Springer International Publishing, 2022, pp. 1317–1361. DOI: 10.1007/978-3-030-31307-4_64. URL: https://link.springer.com/referenceworkentry/10.1007/978-3-030-31307-4_64.

[79] I. Paraschivoiu. *Double-multiple streamtube model for Darrieus in turbines*. 1981. URL: https://ntrs.nasa.gov/citations/19820015811.

[80] Carlos Simão Ferreira. “The near wake of the VAWT: 2D and 3D views of the VAWT aerodynamics The near wake of the VAWT”. PhD thesis. Delft University of Technology, 2009.

[81] Mette Bischoff Kristiansen. *HAWC2: Aerodynamic models*. https://www.hawc2.dk/hawc2-info/aerodynamic-model. n.d. (Accessed: January 2023).

[82] Michael Borg et al. “Offshore floating vertical axis wind turbines, dynamics modelling state of the art. part I: Aerodynamics”. In: *Renewable and Sustainable Energy Reviews* 39 (2014), pp. 1214–1225. DOI: 10.1016/j.rser.2014.07.096.

[83] M.A. Khan. “Dynamic Stall Modeling for Wind Turbines”. MA thesis. Delft University of Technology, 2018. URL: http://repository.tudelft.nl/..

[84] Mark Faber. *A comparison of dynamic stall models and their effect on instabilities*. 2018. URL: www.vindenergi.dtu.dk.

[85] Morten Hartvig Hansen et al. *A Beddoes-Leishman type dynamic stall model in state-space and indicial formulations*. 2004, p. 2023.

[86] J. Gordon Leishman. “Challenges in modeling the unsteady aerodynamics of wind turbines”. In: *ASME 2002 Wind Energy Symposium, WIND2002* (2002), pp. 141–167. DOI: 10.1002/we.62.

[87] Ignas Satkauskas et al. *Wind Turbine Rotor Design Optimization Using Importance Sampling*. National Renewable Energy Laboratory, 2020. URL: www.nrel.gov/publications.

[88] Douglass J. Wilde Panos Y. Papalambros. *Principles of Optimal Design: Modeling and Computation*. Cambridge University Press, 2000.

[89] Turaj Ashuri. “Beyond Classical Upscaling: Integrated Aeroservoelastic Design and Optimization of Large Offshore Wind Turbines”. PhD thesis. Delft University of Technology, 2012.

[90] P. Jamieson. *Loading and cost trends using certification calculation*. 2007.

[91] Gaspar Gohin. “Upscaling, analysis, and design of a floating vertical axis wind turbine”. MA thesis. Norwegian University of Science and Technology, 2018.

[92] Robert David Bitsche. *Airfoil2BECAS: A preprocessor for the cross-section analysis software BECAS*. 2014.

[93] DTU Wind Energy - Department of Wind Energy. *Structural Model - E-lesson 2: Defining the Structure*. University Lecture (Technical University of Denmark). n.d.

[94] DTU Wind Energy. *BLADED to HAWC2 model conversion*. https://toolbox.pages.windenergy.dtu.dk/WindEnergyToolbox/bladed/bladed2hawc.html. 2018. (Accessed: June 2023).

[95] Nelda Andersone. *HAWC2: FAQ*. https://www.hawc2.dk/support/faq#structural-model. n.d. (Accessed: June 2023).

[96] DTU Wind Energy - Department of Wind Energy. *Structural Model - E-lesson 3: Orienting and Constraining Bodies*. University Lecture (Technical University of Denmark). n.d.

[97] Furqan Ahmad et al. “The effects of stacking sequence on the penetration-resistant behaviors of T800 carbon fiber composite plates under low-velocity impact loading”. In: *Carbon Letters* 16 (2 Apr. 2015), pp. 107–115. DOI: 10.5714/CL.2015.16.2.107.

[98] Nicolas Parneix et al. *Efficiency Improvement of Vertical-Axis Wind Turbines with Counter-Rotating Lay-out*. 2016.

[99] AdvanTec. *Advantages of Structural Steel Construction*. https://www.advantecglobal.com/industrial/6-advantages-of-structural-steel-construction/. 2022. (Accessed: June 2023).

[100] Jatin Gupta. *What are the advantages and disadvantages of steel and concrete for windmills?* https://www.quora.com/What-are-the-advantages-and-disadvantages-of-steel-and-concrete-for-windmills. 2023. (Accessed: August 2023).

[101] Huisman Equipment. *VAWT FEM Results V2*. Document number: A21-11750-B1-001. 2022.

[102] Christian Bak et al. *Description of the DTU 10 MW Reference Wind Turbine*. Technical University of Denmark, Department of Wind Energy, 2013.

[103] Henrik Bredmose et al. *COst REduction and increase performance of floating WIND technology (COREWIND) D1.1 Definition of the 15 MW Reference Wind Turbine. D1.1 Definition of the 15 MW Reference Wind Turbine*. 2020.

[104] Mikkel Friis-Møller. *Simulation setup*. https://www.hawc2.dk/about-hawc2/simulation-setup. n.d. (Accessed: June 2023).

[105] Wikipedia contributors. *Newmark-beta method*. https://en.wikipedia.org/wiki/Newmark-beta_method. 2022. (Accessed: June 2023).

[106] Joanna Arida. "The Newton-Raphson method". In: (2021). DOI: 10.13140/RG.2.2.32727.19366. URL: https://www.researchgate.net/publication/350911714.

[107] Kristian Dixon et al. *A 3D unsteady panel method for vertical axis wind turbines AWESCO-Airborne Wind Energy System Modelling, Control and Optimisation View project Aeroelastic Analysis of a 300kW H-type VAWT View project*. 2008. URL: https://www.researchgate.net/publication/259089589.

[108] Michael S. Forsthoffer. "Compressors". In: Elsevier, 2017, pp. 73–185. DOI: 10.1016/B978-0-12-809277-4.00003-6. URL: https://linkinghub.elsevier.com/retrieve/pii/B9780128092774000036.

[109] Kathy Cao et al. "Comparing wind turbine aeroelastic response predictions for turbines with increasingly flexible blades". In: *Journal of Physics: Conference Series* 2265 (3 June 2022). DOI: 10.1088/1742-6596/2265/3/032025.

[110] DTU Wind Energy - Department of Wind Energy. *Aerodynamic Model - E-lesson 4: Aerodynamic input in HAWC2*. University Lecture (Technical University of Denmark). n.d.

[111] Weipao Miao et al. "Recommendation for strut designs of vertical axis wind turbines: Effects of strut profiles and connecting configurations on the aerodynamic performance". In: *Energy Conversion and Management* 276 (Jan. 2023). DOI: 10.1016/j.enconman.2022.116436.

[112] Philip Marsh et al. "Three-dimensional numerical simulations of straight-bladed vertical axis tidal turbines investigating power output, torque ripple and mounting forces". In: *Renewable Energy* 83 (Nov. 2015), pp. 67–77. DOI: 10.1016/J.RENENE.2015.04.014.

[113] Thierry Villeneuve et al. "Increasing the efficiency of vertical-axis turbines through improved blade support structures". In: *Renewable Energy* 169 (May 2021), pp. 1386–1401. DOI: 10.1016/J.RENENE.2021.01.092.

[114] Andrzej J Fiedler et al. *Blade Offset and Pitch Effects on a High Solidity Vertical Axis Wind Turbine*. 2009.

[115] Seán Carroll. *How to Calculate Beam Deflection*. https://www.degreetutors.com/beam-deflection/. 2022. (Accessed: February 2023).

[116] Hui Wang et al. "Chapter 2 - Mechanics of solids and structures". In: *Methods of Fundamental Solutions in Solid Mechanics*. Ed. by Hui Wang et al. Elsevier, 2019, pp. 53–90. DOI: https://doi.org/10.1016/B978-0-12-818283-3.00002-6. URL: https://www.sciencedirect.com/science/article/pii/B9780128182833000026.

[117] Agostino De Marco et al. "A numerical study on a vertical-axis wind turbine with inclined arms". In: *International Journal of Aerospace Engineering* 2014 (2014). DOI: 10.1155/2014/180498.

[118] Aya Aihara et al. "A numerical study of strut and tower influence on the performance of vertical axis wind turbines using computational fluid dynamics simulation". In: *Wind Energy* 25 (5 May 2022), pp. 897–913. DOI: 10.1002/we.2704.

[119] S. Brusca et al. "Design of a vertical-axis wind turbine: how the aspect ratio affects the turbine's performance". In: *International Journal of Energy and Environmental Engineering* 5 (4 Dec. 2014), pp. 333–340. DOI: 10.1007/s40095-014-0129-x.

[120] Airfoil Tools. *NACA 0021 (naca0021-il)*. http://airfoiltools.com/airfoil/details?airfoil=naca0021-il. 2023. (Accessed: January 2023).

[121] E.A. Ferede et al. "NURBS-based Parametric Modelling of Wind Turbine Blades". In: *Proceedings of 9th PhD Seminar on Wind Energy in Europe*. Uppsala University Campus Gotland, Sweden,

2013. URL: https://www.eawe.eu/site/assets/files/downloads/9th-phd-seminar-book-of-abstracts-2013.pdf.

[122] David Marten et al. *User's Guide: Polar Extrapolation Overview*. https://docs.qblade.org/src/user/airfoil/polar_extrapolation.html. 2021. (Accessed: April/May 2023).

A

Structural input file for HAWC2

The structural input file is related to the half-chord point in the cross-section. Figure A.1 shows the cross-section structural centers, half-chord location, and structural pitch definition on a blade cross-section. The half-chord point coincides with the nodal positions defined in the htc-file of HAWC2.

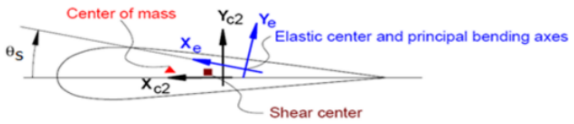

Figure A.1: Visualization of the cross-section structural centers, half-chord location, and structural pitch definition [94].

In Table A.1, the structural parameters which HAWC2 needs are described. These are the parameters for the original beam model. The structural input file has then 19 files. It should be noted that the elastic and shear centers are not always the same in blade-cross sections [93]. Moreover, the main bending axes of the blades are not always parallel to the chord line.

Table A.1: Structural parameters needed for HAWC2 when modeled as origional beam element structural data [52].

Column	Parameter	Unit	Definiton
1	r	m	Curved length distance from main_body node 1
2	m	kg/m	Mass per unit length
3	x_m	m	x_{c2}-coordinate from $C_{1/2}$ to mass center
4	y_m	m	y_{c2}-coordinate from $C_{1/2}$ to mass center
5	r_{ix}	m	Radius of gyration related to elastic center Corresponds to rotation about principal bending x_e axis
6	r_{iy}	m	Radius of gyration related to elastic center Corresponds to rotation about principal bending x_e axis
7	x_s	m	x_{c2}-coordinate from $C_{1/2}$ to shear center
8	y_s	m	y_{c2}-coordinate from $C_{1/2}$ to shear center
9	E	N/m^2	Modulus of elasticity
10	G	N/m^2	Shear modulus of elasticity
11	I_x	m^4	Area moment of inertia with respect to principal bending x_e axis
12	I_y	m^4	Area moment of inertia with respect to principal bending y_e axis
13	K	m^4/rad	Torsional stiffness constant with respect to z_e axis at the shear center
14	k_x	-	Shear factor for force in principal bending x_e
15	k_y	-	Shear factor for force in principal bending y_e
16	A	m^2	Cross-sectional area
17	θ_z	deg	Structural pitch about z_{c2} axis Angle between x_{c2}-axis defined with the c2_def command and the main principal bending axis x_e
18	x_e	m	x_{c2}-coordinate from $C_{1/2}$ to center of elasticity
19	y_e	m	y_{c2}-coordinate from $C_{1/2}$ to center of elasticity

B

Structural models

BECAS provides for every structural model visualization of the mesh (Section B.1) and cross-sectional parameters (Section B.2).

B.1. Mesh

The mesh with the centers and axes of the V1 and V2 structural models are given below.

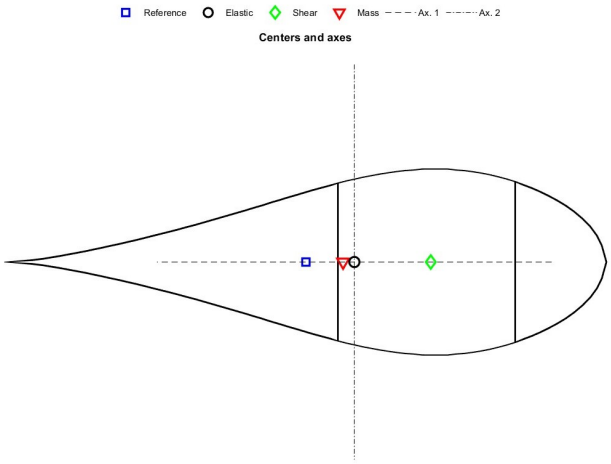

Figure B.1: Mesh with centers and axes of the V1 structural model.

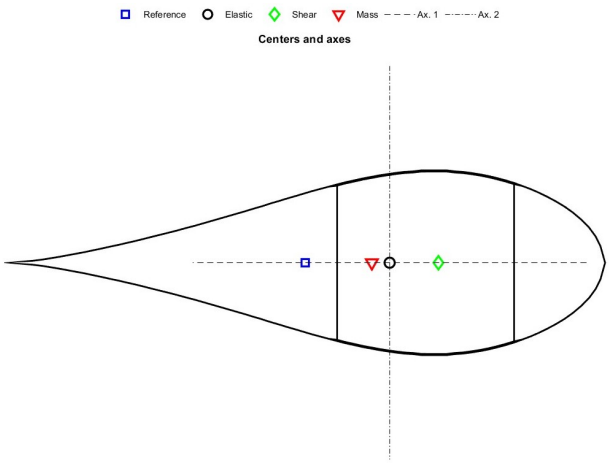

Figure B.2: Mesh with centers and axes of the V2 structural model.

B.2. Cross-section parameters

The cross-sectional parameters are obtained for both the blade and the strut. The blade differs for every structural model, but the blade has the same cross-section over its whole length. The strut is kept the same for every structural model, though the cross-section varies from tip to base.

B.2.1. Blade

In this section, the cross-section parameters that are needed for HAWC2 are written down in Table B.1.

Table B.1: Cross-sectional parameters of the blade for every structural model that are required for HAWC2.

Parameter	Symbol	Unit	Max	V1	V2
Mass per unit length	m	kg/m	246.8	103.01	159.69
Center of mass	x_{cg}	m	0.546	0.292	0.523
Center of mass	y_{cg}	m	≈ 0	≈ 0	≈ 0
Radius of gyration	r_{ix}	m	0.541	0.446	0.540
Radius of gyration	r_{iy}	m	1.122	1.328	1.144
Structural pitch	γ	deg	≈ 0	≈ 0	≈ 0
Elastic center	x_e	m	0.681	0.380	0.662
Elastic center	y_e	m	≈ 0	≈ 0	≈ 0

B.2.2. Strut

The input variables for the cross-section of the strut are listed in Table B.2.

Table B.2: Cross-sectional parameters of the strut that are required for HAWC2.

Parameter	Symbol	Unit	Tip	Base
Mass per unit length	m	kg/m	99.44	185.12
Center of mass	x_{cg}	m	≈ 0	≈ 0
Center of mass	y_{cg}	m	≈ 0	≈ 0
Radius of gyration	r_{ix}	m	0.281	0.481
Radius of gyration	r_{iy}	m	0.305	0.606
Structural pitch	γ	deg	≈ 0	90
Elastic center	x_e	m	≈ 0	≈ 0
Elastic center	y_e	m	≈ 0	≈ 0

C

Extrapolation of polars

The polar data for an airfoil frequently only applies to a limited range of angles of attack. This is referred to as partial polars. Because of this, QBlade has a module that extrapolates the polars to a whole 360 degrees range. The extrapolation of two airfoils (NACA0031 and NACA0021) has been done by QBlade. QBlade makes use of XFoil to find the polars in a smaller range of angles of attack, until $C_{l,max}$ at stall angle. The Viterna method is used to extrapolate airfoil partial polar data. The following parameters can be adjusted in QBlade during the extrapolation process [122]:

- **Range of original polar** (angle of attack) to use for the interpolation;
- The specific drag coefficient **CD90** at α= 90°, which influences the lift coefficient as well;
- **The positive and negative stall** for an airfoil, $St+$ and $St-$.

In Figure C.1, the extrapolation of the NACA0031 airfoil polars is shown. The maximum lift coefficient lays around $C_{l,max} = 1.5$ [-].

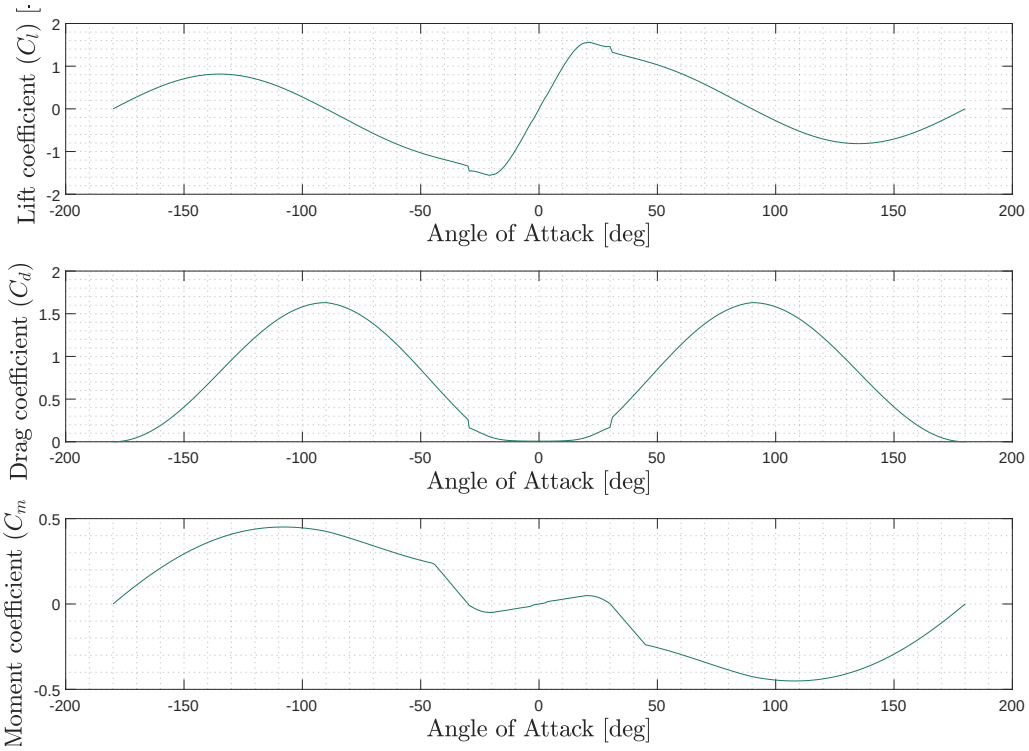

Figure C.1: Extrapolation of the NACA0031 airfoil polars in QBlade.

Figure C.2 shows the extrapolation of the NACA0021 airfoil polars, in which the maximum lift coefficient lies slightly higher.

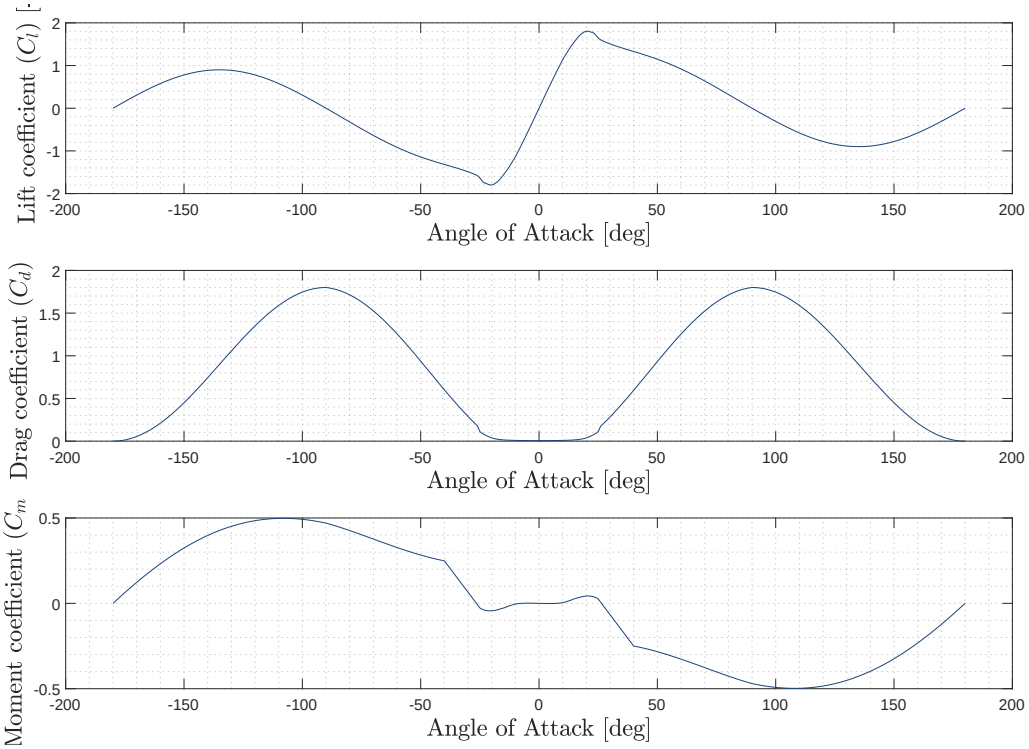

Figure C.2: Extrapolation of the NACA0021 airfoil polars in QBlade.

D

Supported constraint types in HAWC2

In order to create more complex systems, HAWC2 offers a variety of various constraints [96]. Below, the bearing types are mentioned.

- Bearing 1: Frictionless bearing;
- Bearing 2: Bearing for which a fixed angle is specified by an external DLL;
- Bearing 3: Bearing with a constant specified angle velocity;
- Bearing 4: Cardan shaft, locked in rotation around one vector, but free to rotate around the two other axes.

Moreover, different constraints when linking bodies can be employed as well. The user can decide which constraint, and only one constraint, will be set between bodies.

- Fix 0: Clamped to the ground;
- Fix 1: Clamped connection;
- Fix 2: Fix node to ground, optionally specify the axis of free translation;
- Fix 3: Fix node to the ground, optionally specify the axis of free rotation;
- Fix 4: Locked in translation, but not in rotation, with pre-stress feature.

E

Post-processing calculations

MATLAB is used as an analytical tool for the calculations utilized for post-processing the simulation data. The focus lies on collecting and managing important data obtained from HAWC2 simulations. Only data collected after the transient period is considered for analysis to guarantee data accuracy and consistency.

E.1. Rotation

The azimuthal angle is found with the bearing angle, which can be outputted by HAWC2. One rotation is taken after the transient period to the end of the simulation.

E.2. Deflection

From HAWC2, the position in the x- and y-direction in the global coordinate system can be taken as output. If the rotor makes a perfect rotation, the blades provide a sinusoidal output with the rotor radius (R) and the rotational speed (ω). The x and y data can therefore be transformed from Cartesian coordinates to polar coordinates (theta and rho).

```
[theta,rho] = cart2pol(x,y)
```

The total deflection of the blade can be found by subtracting the rotor radius from the polar coordinates.

F

Extra result plots

In this chapter, extra plots of the results are shortly presented.

F.1. Laminate thickness

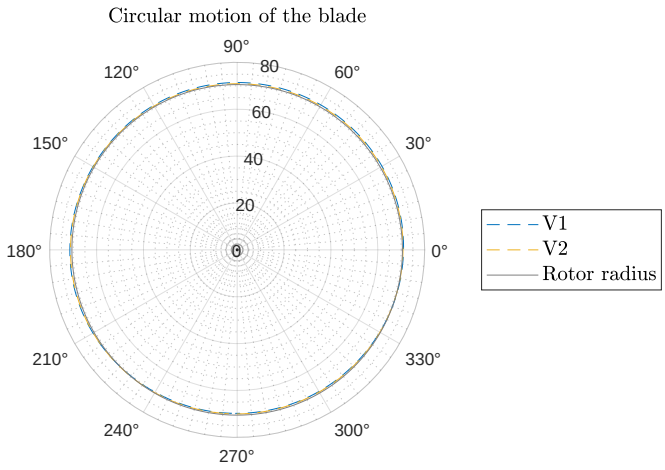

Figure F.1: Circular motion of the middle part of the blade for the V1 and V2 model.

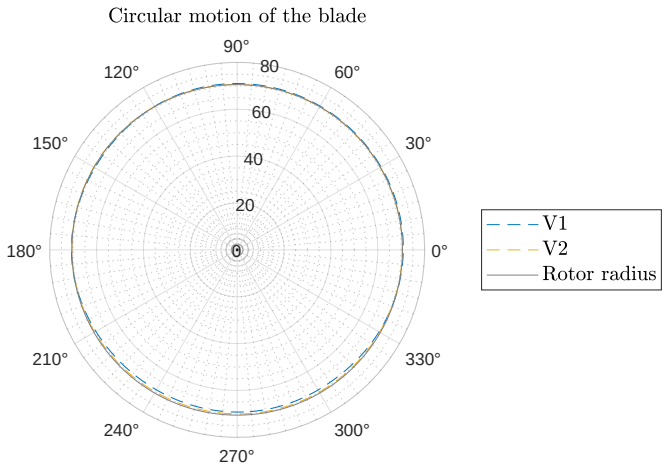

Figure F.2: Circular motion of the bottom part of the blade for the V1 and V2 model.

F.2. Upscaling

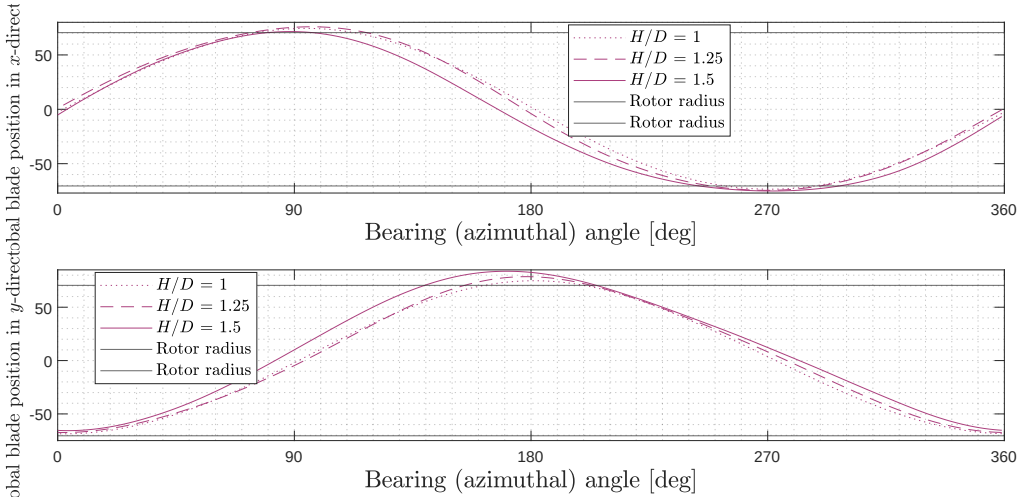

Figure F.3: The rotation of the tip of the blade in the x- and y-direction of the global coordinate system for different aspect ratios (H/D).

F.3. Huisman

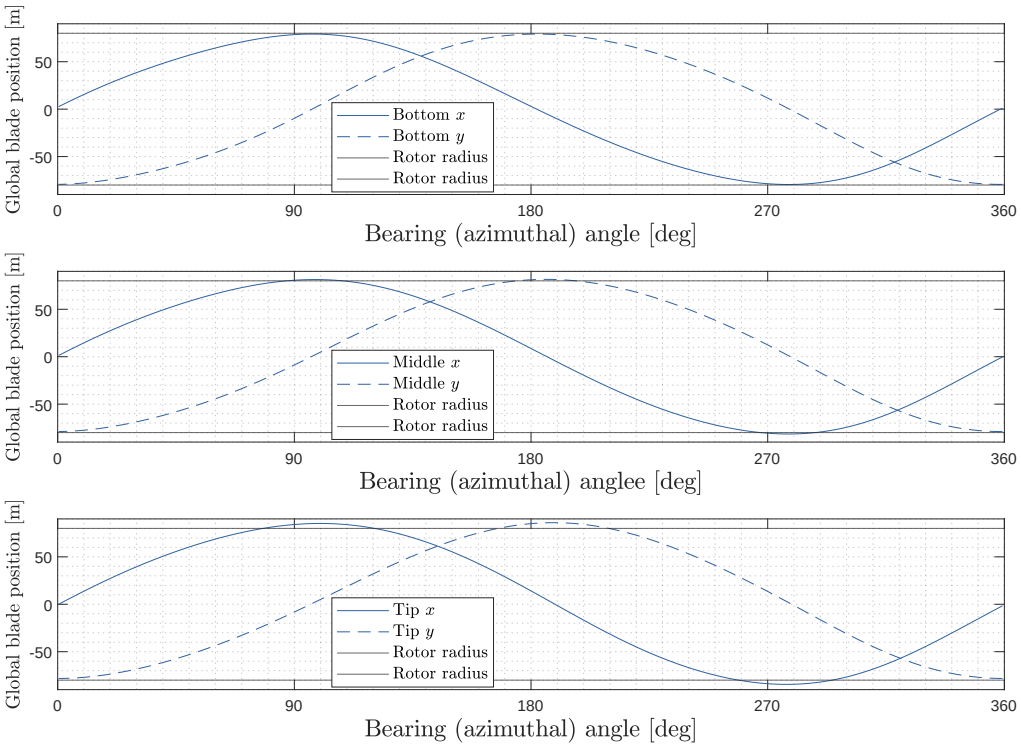

Figure F.4: The rotation of the blades of the simplified Huisman design over one rotation at three different positions: the bottom, middle, and tip.